Evolution and Impact of Microstructure in Functional Materials

by

Erik Hanson

A dissertation submitted in partial fulfillment
of the requirements for the degree of
Doctor of Philosophy
(Materials Science and Engineering)
in the University of Michigan
2019

Doctoral Committee:

Professor Katsuyo Thornton, Chair
Professor Anthony Grbic
Professor Emmanuelle Marquis
Professor Ashwin Shahani

Erik Hanson

erikhans@umich.edu

ORCID iD: 0000-0001-9917-4067

To my wife,
the mother of my children,
and my best friend.

Acknowledgements

There are a great many people who have helped make my journey possible. First and foremost, I would like to thank Professor Katsuyo Thornton for giving me the opportunity to join her research group and for providing her wisdom, guidance, and understanding throughout my time here. It is difficult to imagine successfully navigating the last several years without her help. I would also like to give my appreciation to my other committee members, Professor Ashwin Shahani, Professor Emmanuelle Marquis, and Professor Anthony Grbic for offering their time and support.

I would like to acknowledge the considerable help I've received from other members of the Thornton group, both past and present. Larry Aagesen was a critical mentor when I started in the group and his knowledge helped lay the foundation of my understanding of numerical simulation and eutectic solidification. Hui-Chia Yu provided me with essential understanding of the Smoothed Boundary Method and jumpstarted my grasp of visualization techniques. David Montiel pointed me toward useful resources and contributed many useful discussions and feedback. Min-Ju Choe supplied the initial inspiration for the hindered grain boundary diffusion work and I appreciate his support outside the research. Alex Chadwick's codes for manipulating polycrystalline structures were an essential stepping stone. Max Powers contributed greatly to the hindered grain boundary diffusion work. Thank you also to Beck Andrews, Jason Luce, Stephen DeWitt, Dong-Uk Kim, Geetha Krishna, and Susanta Ghosh for helpful conversations along the way.

A large portion of my work has been a joint effort with my experimental collaborators. The opportunity to collaborate with Ashish Kulkarni, Julia Kohanek, and Paul Braun was critical in building my understanding of optical materials and eutectic solidification. The discoveries we made and the knowledge we built, we did together. Will Boley and Jennifer Lewis were essential in the eutectic printing study. Mengdi Han, Yan Zheng, and John Rogers did a phenomenal job at organizing the three-dimensional cage work.

I would also like to thank my family and friends. My parents, Beth and Jim, have encouraged my passion for science for a very long time and they've enabled my education at every step. The rest of my family and the friends I've made here have provided essential encouragement and support. My sons, Simon and soon-to-be Levi, provided me with valuable perspective in hard times. Simon has also granted me a sense of great accomplishment by increasing the difficulty of attaining my degree through perpetual sleep deprivation. Perhaps most of all, I must express my gratitude to my wife, Becka. The sacrifices she's made to allow me to pursue this aspiration are immeasurable. The trust she has placed in me throughout this journey, but particularly at its origin, was dearly cherished.

I must also acknowledge the funding agencies and computational resources that supported my research. My eutectic research was supported by the Air Force Office of Scientific Research MURI (Multidisciplinary University Research Initiative) FA9550-12-0471. The hindered grain boundary diffusion model work was supported by the National Science Foundation under Grant No. 1506055 and the NorthEast Center for Chemical Energy Storage (NECCES), an Energy Frontier Research Center funded by the U.S. Department of Energy (DOE), Office of Science, Basic Energy Sciences (BES) under Award No. DESC0012583. The computational resources utilized in my research were provided by the Department of Defense

High Performance Modernization Program, the Extreme Science and Engineering Discovery Environment (XSEDE), and Advanced Research Computing at the University of Michigan.

Table of Contents

List of Figures

List of Tables

Abstract

A series of investigations are conducted to determine, first, how microstructure evolves in the synthesis of optical materials via template-directed eutectic solidification and, second, how microstructure affects the chemical transport properties of function materials with diffusional hindrance at grain boundaries.

As the first and primary part of this thesis, self-organization techniques, such as eutectic solidification, are being explored to enable fabrication of large-area optical metamaterials and to overcome the limitations of traditional metamaterial synthesis methods. Directing the solidification of a eutectic material through a non-reactive periodic template yields more complex morphologies with different length scales than those of either the native eutectic material or the template alone. Phase-field simulations utilizing the smoothed boundary method (SBM) to include template-eutectic interactions are conducted, and the predictions are used to guide the design of template geometries and the selection of eutectic material systems.

A combination of phase-field and heat transfer simulations elucidate the morphological evolution of four cases of geometric confinement. The first case is a printed AgCl-KCl eutectic filament. The simulated temperature profile reveals an inward solidification direction at the filament edges, whereas the filament center solidifies along the printing direction. In another case, eutectic solidification is guided by the surface of a three-dimensional cage structure. The cage's nonuniform thermal conductivity results in a curved solidification front. Additionally,

simulations indicate in an investigation of a solidification velocity-dependent rod-to-lamellar transition in the eutectic microstructure of AgCl-$CsAgCl_2$, that the structure which forms initially on the cool surface will persist through the bulk. Finally, through phase-field simulations with asymmetric eutectic-template interfacial energies confined within a cylindrical channel, core-shell nanowire morphologies are realized.

Solidifying binary eutectic materials confined to a template consisting of an array of pillar obstacles produces periodic structures with a high degree of order. These pillar templates can also be used to exert control over lamellar orientation. The relationship between undercooling and lamellar orientation is explored via phase-field simulations and the cause of lamellar reorientation within a template is discovered. Highly ordered mesostructures develop when solidifying along the pillar axis. A parametric study is conducted to investigate the effects of minority-phase volume fraction, template volume fraction, and solidification velocity on these mesostructures.

The second part of this thesis considers interfaces and grain boundaries that can enhance or hinder transport, which alter the properties of polycrystalline solids from their intrinsic bulk properties. Diffusion in polycrystalline materials can be hindered at grain boundaries in several material systems, including those of solid oxide fuel cells and batteries. A hindered grain boundary diffusion model employing SBM is developed, analyzed, and utilized to study a nanocrystalline solid oxide fuel cell material (yttria-stabilized zirconia) and a battery cathode material (nickel manganese cobalt oxide). Further, effective diffusivities are extracted from the concentration profiles produced by the model for a range of grain morphologies. The anisotropy of grain morphologies plays a critical role in the overall transport behavior, which cannot be quantified with preexisting mean-field approximations. Steady-state concentration profiles are used to guide the development of a universal expression for predicting effective diffusivities of

complex polycrystalline solids without computationally intensive simulations. The universal expression predicts effective diffusivity more accurately than the Maxwell Garnett equation does by up to 57%, depending on anisotropy. This approach enables efficient simulation of transport in larger-scale systems while accurately capturing the effects of grain morphologies.

Chapter 1: Introduction

1.1 Motivation – Template-Directed Eutectic Solidification

This section is largely a reproduction of part of the article titled "Template-Directed Solidification of Eutectic Optical Materials" previously published in Advanced Optical Materials in 2018.[1]

Photonic crystals (materials with periodic variations in optical properties in one, two, or three dimensions on the order of the wavelength of light) are widely utilized to manipulate light.[2] Example devices based on photonic crystals include distributed Bragg reflectors, diffraction gratings, wire-grid polarizers, some waveguides, and many lasers.[2-4] Materials with powerful optical functionalities, including negative-index of refraction and optical chirality, can be realized by appropriate placement of materials with suitable properties in two or three-dimensional space.[5-7] Light in the visible spectrum can be manipulated, although the tolerance for defects is exceedingly low at visible frequencies, and the number of materials with the appropriate properties is limited.[8,9] Most photonic crystals are fabricated by high-resolution top-down two-dimensional patterning methods such as electron-beam lithography, interference lithography, and focused ion beam milling.[10] However, it is challenging to fabricate large-area bulk materials with these techniques, especially with intricate internal structures.[9] Additionally, many materials with promising optical properties are not compatible with these top-down patterning methods. [5,11]

As work on colloidal crystals has shown, controlled self-assembly is an effective route to organizing materials into three-dimensional architectures that interact strongly with light.[10-14] Colloidal self-assembly, however, only offers a limited set of symmetries (generally those of close packed arrangements), and a spherical basis.[13] For many applications, considerably more complex structures are of interest. Particularly promising approaches for forming materials with complex internal microstructures include eutectic solidification and block copolymer self-assembly,[15-17] and materials with interesting optical properties have been reported using both approaches. These methods are advantageous due to the wide range of microstructures they form. Here, we focus on the structures formed by eutectic solidification since materials with a broader range of optical properties are available compared to that provided by block copolymers, and because the characteristic lengths of structures accessible through eutectic solidification better match the wavelengths of visible light and infrared radiation. Further, forming materials with sufficiently large characteristic dimensions for interaction with visible light by block copolymer assembly is synthetically challenging as it requires high molecular weight polymers.[18] Similarly, self-assembly of other building blocks, *e.g.*, nanoparticles,[19,20] molecules,[21,22] and DNA,[23,24] tend to produce structures with characteristic dimensions too small to provide strong light-matter interactions (via diffractive phenomena).[3,4,25]

Thus, the concept of template-directed eutectic solidification is proposed and explored. There is a vast library of eutectic systems that have promising material combinations and the solidification of eutectic materials has been well studied. Despite this, the utilization of eutectic materials for optical functionalities has not received sufficient attention to realize their full potential.

Phase-field simulation of the microstructural evolution in template-directed eutectic solidification can give further insight as both a complement to experiments and as a predictive

tool. One benefit realized through simulation is the ability to investigate the isolated effects of each material property or process parameter. For example, one can adjust the eutectic-point phase fraction of a material system in a simulation without changing other parameters ordinarily associated with a material change, such as diffusivity or interfacial energy. This approach allows one to gain understanding of what material properties or process parameters have the largest influence on the resultant microstructure and its ability to facilitate a desired optical response. Simulations also allow the examination of details that are difficult or impossible to observe during experiments, such as the orientation of the solidification front or the specifics of the path of microstructure evolution. Some of these details can be quantified in the simulation, such as the undercooling of the solidification front or the chemical composition distribution in the liquid ahead of the front.

Additionally, simulating the template-directed eutectic solidification can often offer strategies for circumventing challenges that arise in experiments, such as the potential difficulty in controlling the temperature profile of a sample during solidification, issues with eutectic-substrate compatibility, or synthesizing particular template geometry. Overcoming these experimental challenges is sometimes necessary, but using the simulations as a predictive tool to determine promising combinations of template geometries, material properties, and processing parameters narrows the focus of the experimental efforts and thus increases developmental efficiency. In this manner, the cooperation of both experiments and simulations can lead to novel and successful template-directed eutectic optical materials more rapidly than experiments alone.

1.2 Motivation – Hindered Grain Boundary Diffusion

Solid oxide fuel cells are valued for their high efficiency of up to 70%.[26] These fuel cells are composed of three layers: a porous cathode, a dense electrolyte, and a porous anode. Hydrogen fuel is oxidized at the surface of the porous anode and the produced electrons flow

through an external circuit to the cathode, where they reduce the oxygen, producing O^{2-} ions.[27] These oxygen ions move from the cathode, through the electrolyte, and into the anode to enable hydrogen oxidation. Thus, a high ionic conductivity in the electrolyte layer is critical for the effective production of electricity in a solid oxide fuel cell.[28] Oxygen ion diffusivity increases at high temperature, so solid oxide fuel cells are often operated at elevated temperatures (800-1000°C)[26,27,29] Due, in part, to its low electronic conductivity, zirconia is a common selection as the basis of the electrolyte layer. Zirconia is often doped with up to 8% yttria to form yttria-stabilized zirconia (YSZ), thereby replacing Zr^{4+} ions with Y^{3+} ions and introducing oxygen vacancies.[30] The migration of these vacancies facilitates the diffusion of oxygen ions, therefore improving the ionic conductivity of YSZ. Sintering is commonly used to fabricate a dense YSZ layer,[31] resulting in a polycrystalline structure. Because grain boundaries and similar defects can have a large impact on chemical transport behavior,[32-40] and because high diffusivity is imperative for optimizing solid oxide fuel cell performance, careful consideration of the effect of YSZ grain boundaries is crucial. While many material systems display enhanced diffusion of chemical species at grain boundaries,[32-37] YSZ exhibits the opposite behavior – hindered grain boundary diffusion – due to oxygen vacancy depletion at grain boundaries and space charge layer effects.[38-40] Hindered grain boundary diffusion is not as well studied as enhanced grain boundary diffusion and a quantitative means to investigate the effects of the phenomenon could contribute to expediting advances in grain boundary engineering.

Battery cathodes are another example of an application where ion transport through a polycrystalline structure is essential. Battery cathode particles often consist of agglomerations of smaller particles that form dense, polycrystalline structures.[41-43] For lithium ion batteries, one type of cathode material is a layered transition metal oxide, such as Nickel Cobalt Aluminum oxide (NCA)[41,44] or Nickel Manganese Cobalt oxide (NMC).[42,43] When the battery is discharged

or charged, ions intercalate into or flow out of the layered cathode material, respectively. Charging to a higher voltage increases the amount of lithium intercalating into the cathode material and increases the capacity of the battery; however, the tradeoff of this improvement is a more rapid rate of capacity fading over multiple charge-discharge cycles.[45,46] One potential source of this capacity fade is the formation of microcracks at the grain boundaries of the cathode particle due to the volumetric expansion associated with lithium ion intercalation.[41,44] These cracks reduce the contact area between grains, hindering the diffusion of lithium ions across the grain boundary regions.[41] Further, liquid electrolyte can penetrate into the depths of the cathode particle through the microcracks and enable the formation of a nickel oxide-like layer – which has a significantly lower ionic conductivity – at the grain boundaries.[41,44] Because the ion transport behavior in battery cathodes is so critical, a quantitative model would be beneficial in understanding how the effects of hindrance on lithium-ion transport at grain boundaries affect capacity fading and charge-discharge behavior.

While there are models that can describe enhanced grain boundary diffusion,[47-49] no such models that explicitly account for microstructures exist for hindered grain boundary diffusion. A model that can accurately predict the evolution of concentration profiles for such a system is needed to understand the effects and implications of hindered diffusion in grain boundaries. Other physics can be coupled to the concentration field, such as reaction kinetics in a battery material or the concentration-dependent mechanical response in a cathode particle. In addition, the concentration information can be used to calculate effective properties of a microstructure. For example, the effective diffusivity of a polycrystalline microstructure can be determined from the flux in the system without making assumptions about microstructural morphology; assumptions that are a necessity for mean-field approximations such as the Hart[50] or Maxwell Garnett[51] approaches. Diffuse interface models, which circumvent the need for explicit interface

tracking or remeshing for even complex geometries, have proven successful for calculating concentration evolution in inhomogeneous systems.[47,52]

1.3 Dissertation Outline

This dissertation comprises phase-field and diffuse interface simulation studies, often to understand, support, guide, or inform the research conducted by experimental collaborators. Chapters 1-3 contain general introductory information and simulation methods. Chapters 4-8 contain the principal results of the simulation studies. Experimental findings (conducted solely by collaborators) are included in many cases to provide context, display the simulation-experiment agreement, or because they were, in part, driven by the simulation results themselves.

Chapter 2 contains background information regarding the use of the templating approach, eutectic solidification, and template-directed eutectic solidification in the pursuit of functional optical materials. The previous studies that help to inform the new template-directed eutectic solidification approach are reviewed. In addition, preexisting phase-field models that simulate eutectic solidification are described. Finally, a brief background of grain boundary effects on materials properties and hindered grain boundary diffusion is provided.

Chapter 3 describes the simulation methods. First, the template-directed eutectic solidification model, which is a combination of a phase-field model and the Smoothed Boundary Method (SBM), is explained. A heat transfer calculation method using diffuse interfaces to study the temperature profile in printed eutectic filaments is described. The hindered grain boundary diffusion method using SBM is also provided.

Chapter 4 consists of a series of cases where eutectic materials were solidified under geometric confinement. First, a new method involving printing eutectic filaments is demonstrated. Next, eutectic solidification confined to the surface of ribbon-like legs of a three-dimensional cage structure is investigated. Additionally, a rod-to-lamellar transition is explored

in AgCl-$CsAgCl_2$. Finally, a core-shell nanowire synthesis concept is described that uses confinement within cylindrical channels.

Chapter 5 presents the results of a study of the phenomenon of lamellar reorientation within a template consisting of a periodic array of pillars. The cause of the reorientation is elucidated and the phenomenon is proposed as a means of controlling eutectic orientation and morphology.

Chapter 6 further investigates eutectic solidification in pillar array templates, but now with the solidification direction along the pillar axis. Highly ordered patterns form and multiple morphologies can be selected using the same template geometry and eutectic material system.

Chapter 7 demonstrates the hindered grain boundary diffusion method. The model's error and its dependence on numerical and physical parameters is explored. Case studies for a solid oxide fuel cell and a battery cathode material are examined. Using isotropic and anisotropic polycrystalline microstructures, a comparison is made between the effective diffusivities calculated by the hindered grain boundary diffusion method and preexisting mean-field approximations.

Chapter 8 derives and displays the results of a newly developed expression that predicts the effective diffusivity of polycrystalline solids with grain boundary transport properties that differ from the bulk. The results of the new expression are compared to the results of the hindered grain boundary diffusion method and other preexisting mean-field approximations.

Chapter 9 contains conclusions and recommendations for future work.

Chapter 2: Background

2.1 Template-Directed Eutectic Solidification

This section is in part a reproduction of part of the article titled "Template-Directed Solidification of Eutectic Optical Materials" previously published in Advanced Optical Materials in 2018.[1]

2.1.1 Directionally Solidified Eutectics as Optical Materials

Eutectic material systems have two or more chemical components for which a liquid and two or more solid phases coexist in equilibrium at the eutectic temperature, T_E, and composition, C_E.[15,53] The point (C_E , T_E) on a phase diagram is called the eutectic point. A typical binary eutectic phase diagram for a two-component system (with chemical species A and B), is shown in Figure 2.1a. During solidification of such a eutectic melt, the liquid phase-separates into two distinct solid phases α and β. The simultaneously solidifying phases generally organize into simple motifs consisting of alternating layers (lamellar morphology) or fibrous structures (rod morphology) (Figure 2.1b); however, complex structures, such as spiral or broken lamellar, globular, elongated rods, or even structures resembling split-ring-resonators, are also possible (Figure 2.1c).[15]

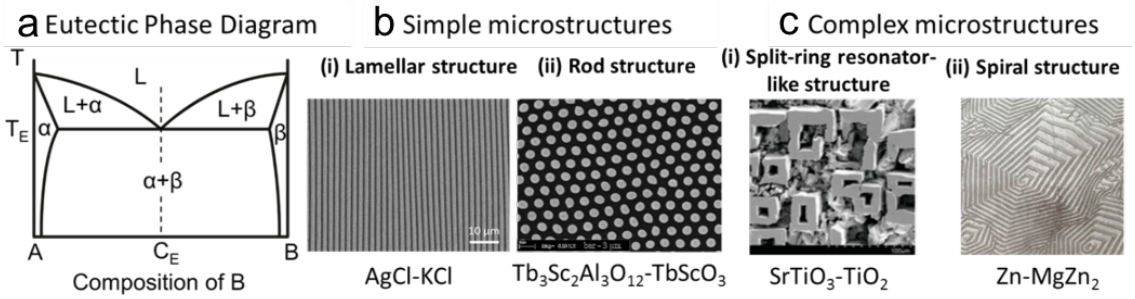

Figure 2.1 Directionally solidified eutectics: (a) A schematic of a typical binary eutectic phase diagram. Examples of simple microstructures: **(b)**-(i) Lamellar structure (AgCl-KCl eutectic) and b-(ii) Rod structure ($Tb_3Sc_2Al_3O_{12}$-$TbScO_3$ eutectic), reproduced with permission.[54] Copyright 2006, American Chemical Society. Examples of complex microstructures: **(c)**-(i) Split-ring resonator-like structure ($SrTiO_3$-TiO_2 eutectic), reproduced with permission.[55] Copyright 2010, Wiley-VCH. c-(ii) Spiral structure (Zn-$MgZn_2$ eutectic, imaged at 1200X magnification).[56] Used with permission of The Minerals, Metals & Materials Society.

The microstructure of a eutectic material is dependent on factors including composition, atomic or ionic diffusivity, interfacial energies, thermal conductivity, and latent heat of fusion of the individual components.[15,56-58] Another important parameter is the rate of solidification, defined as the velocity of the solidification front, v. Depending on the solidification technique, v can be controlled by external parameters, *e.g.*, the temperature gradient in the furnace, sample draw rates through the furnace, and printing speeds.[56,59-62] The laser floating zone method,[63] the micro-pulling-down approach,[54,64] the Czochralski method,[65] the Bridgman furnace,[60,66] and direct ink writing,[62] are examples of methods utilized for the directional solidification of eutectics. The rate of solidification controls the feature size (layer widths, particle or fiber diameter) and the characteristic spacing, λ, of the periodic structures. The ability to tune the length scale of a periodic eutectic structure allows one to adjust which wavelengths of light an optical material interacts with. Jackson and Hunt developed a theory for the relationship between solidification rate and eutectic characteristic spacing.[57] In eutectic solidification, the temperature of the solidification front is lower than the eutectic temperature due to three factors: the

curvature of the solidification front, the buildup of rejected solute in the liquid near the solidification front, and the energy barrier for chemical species to cross the solid-liquid interface.[57] The last of these contributions, called kinetic undercooling, is often negligibly small and disregarded. The difference between the solidification front temperature and T_E is the undercooling, denoted by ΔT, and is described for a binary lamellar structure by

$$\Delta T = \left(\frac{1}{m_\alpha} + \frac{1}{m_\beta}\right)^{-1} \left(v\lambda Q_{JH} + \frac{a_{JH}}{\lambda}\right) \tag{2.1}$$

where m_i is the liquidus slope of phase i linearized about the eutectic point. Q_{JH} and a_{JH} are constants defined by the properties of the material system:

$$Q_{JH} = \frac{\mathrm{P}(1+\zeta)^2 \Delta C}{\zeta D} \tag{2.2}$$

$$a_{JH} = 2T_E(1+\zeta)\left(\frac{\sigma_\alpha \sin\theta_\alpha}{m_\alpha L_\alpha} + \frac{\sigma_\beta \sin\theta_\beta}{\zeta m_\beta L_\beta}\right) \tag{2.3}$$

where ζ is the ratio of β to α phase fraction, P is a constant related to ζ, ΔC is the difference in solubilities of the solid phases at T_E, D is the diffusion coefficient in the liquid, σ_i is the solid-liquid interfacial energy of phase i, θ_i is the contact angle of phase i, and L_i is the latent heat of fusion for phase i.[57]

For a given solidification velocity, the structure and spacing that give the lowest undercooling are most often selected by a eutectic undergoing solidification.[57] Therefore, if we find the minimum in undercooling in Equation 2.1 by setting its derivative to zero, the equation reduces to:

$$\lambda^2 v = \frac{a_{JH}}{Q_{JH}} \tag{2.4}$$

Under steady-state conditions of eutectic growth, $\lambda^2 v$ is constant for the given material system, thus fast rates of heat removal (high v) lead to small characteristic spacing and *vice versa*.[57] This characteristic spacing control can be effective over a wide range, from tens of nanometers to hundreds of microns, without changing material systems.[67] The constituent materials of the eutectic can be chosen from many material types, including metals, organics, salts, ceramics, semiconductors, and polymers.[68-70]

There is a vast variety of eutectic materials that are yet to be explored for their optical properties,[71] as well as a wide range of processing conditions that can be applied. The number of variables here indicates a phase space that cannot be efficiently studied through experiments alone, which is why the application of simulation and theory is critical to explore even simple systems. Additional complications arise when studying complex (or anomalous) eutectics, such as Al-Ge or Al-Si, as the structure of these systems are highly dependent on the growth mechanisms of the individual phases.[72,73] These metal-dielectric systems are particularly interesting for metamaterial applications, which require one phase of the system to have a metallic character. To date, the nature of the solidification in these metal-dielectric eutectic systems has made it difficult to achieve precise control over the orientation and long-range order of the solidifying structure, as well as its computational investigation.[74-76]

It is clear that the microstructure present in solidified eutectics can result in materials with significant potential for photonic applications. However, to fully realize the potential of eutectic solidification, it is crucial to make use of quantitative models that can predict the microstructures formed by eutectic solidification.

2.1.2 Phase-Field Modeling of Eutectic Microstructure Evolution

Predicting the microstructure of self-organizing systems is challenging even when the underlying physics is well understood. With the growth of computational resources and

improvements in computational capabilities, numerical simulation has become a practical approach for solving complex problems such as this. Simulations of microstructural evolution have been conducted utilizing many different methods,[77-95] spanning a wide range of time and length scales.

An important element of modeling multiphase and composite systems is how to describe interfaces. There are two approaches for treating interfaces mathematically. One approach is known as the sharp interface model that considers interfaces between phases as surfaces with zero thickness. Simulations based on this approach follow the positions of the interfaces at every time step. Boundary conditions are imposed on these sharp interfaces, which may have complex morphologies. The level set method,[83] the boundary integral method,[96] and the enthalpy method[87] have been developed based on sharp interface models to simulate eutectic solidification. Another approach, the so-called diffuse interface model, represents interfaces with a field defined in three dimensions, which includes a transition region with a finite thickness near phase boundaries.[97] The field varies smoothly from one phase to another, and therefore appears diffuse, leading to its name. The interfacial locations are determined from this field, rather than explicitly tracked. The phase-field model is one type of diffuse interface model developed for simulating phase transformations and microstructural evolution because of its ability to take into account both the thermodynamics and kinetics of materials.

Phase-field models represent phases with a field called as an order parameter. An order parameter may correspond to the concentration of a chemical species, which is distinct in different phases, or represent the degree of order/disorder at the atomic level (*e.g.,* crystalline solid vs. liquid). The order parameter takes a constant value in the bulk regions of a phase, transitioning smoothly between these values at the interfaces between phases with a finite thickness. The temporal change of the order parameter implicitly captures the motion of

interfaces without explicit tracking. The thickness of the interface in a phase-field model is a numerical input parameter and is typically chosen to be much larger than the physical interfacial thickness to increase computational efficiency without affecting the dynamics when the interfacial thickness is taken to be sufficiently small compared to characteristic length scales in the system.[98,99]

The temporal evolution of the order parameter is driven toward configurations that decrease the total free energy of the system. The total free energy, F is defined as the integral of the local free energy density, f, in space, V:

$$F = \int_V f dV \tag{2.1}$$

The most basic form of the free energy density consists of two terms: bulk free energy density describing the thermodynamics of the material and energy density that penalizes gradient in the order parameter. These two terms together describe the energetics of the system, including the interfacial energy. An example of f can be given by:

$$f = w\phi^2(1-\phi)^2 + \frac{\epsilon^2}{2}(\nabla\phi)^2 \tag{2.2}$$

where the bulk free energy is modeled with a double-well function, and w and ϵ are the double-well height and gradient energy coefficient, respectively. The term $w\phi^2(1-\phi)^2$ is the bulk free energy that induces phase separation due to the energy minima at bulk phase values of $\phi = 0$ and $\phi = 1$. A more realistic model includes dependences on other variables, such as temperature in solidification modeling. The other term, $\frac{\epsilon^2}{2}(\nabla\phi)^2$, provides an energy penalty for large gradients in the order parameter, resulting in interfaces with a finite thickness. Additional free energy density terms can be added to capture the underlying physics of a system, such as elastic strain energy. Based on the constructed total free energy, the rate of change of the order parameter at each point, $\partial\phi/\partial t$, is given by two types of equations. For a conserved order

parameter (*e.g.*, a concentration field), the Cahn-Hilliard equation,[100] which results from mass conservation with a flux driven by chemical potential gradient, applies:

$$\frac{\partial \phi}{\partial t} = \nabla \cdot \left[M \nabla \left(\frac{\delta F}{\delta \phi} \right) \right] \tag{2.3}$$

where M is a mobility associated with the conserved order parameter and $\delta F / \delta \phi$ is the variational derivative of F,[101] which is an infinitesimal change of F corresponding to an infinitesimal change of ϕ. For a nonconserved order parameter (*e.g.*, a field representing the degree of atomic-level order/disorder), the Allen-Cahn equation is applied:[102]

$$\frac{\partial \phi}{\partial t} = -L \nabla \left(\frac{\delta F}{\delta \phi} \right) \tag{2.4}$$

where L is a mobility associated with the nonconserved order parameter.

Phase-field models have an advantage of simpler numerical implementation compared to most sharp interface models. Here, boundary conditions do not need to be imposed on the interfaces, which often have complex morphologies. This enables the use of the finite difference method,[103] which is a straightforward numerical approach for solving partial differential equations. The validity of phase-field models can be assessed by examining the sharp interface asymptotics for the phase-field model,[98,99,104,105] and by comparing the phase-field simulation results to the sharp interface models.[106,107]

Phase-field models of eutectic solidification found in existing literature have been developed[108-112] based on the quantitative phase-field models of solidification.[98,99,113-115] Early phase-field models for eutectic solidification were demonstrated for binary eutectics but were not computationally efficient because fine spatial resolutions were required for resolving composition gradients and their evolution within the interface.[116-119] Multi-phase-field models enabled examination of three or more phases.[108,109] These models were further developed to

improve accuracy and computational efficiency by mitigating a diffuse interface artifact (i.e., solute trapping) and have been validated against the Jackson-Hunt theory.[57,110-112]

Many aspects of microstructural formations in eutectic solidification have been studied by using phase-field models. Phase-field simulations of eutectic colony formation[120] and lamellar stability during solidification[121-124] have provided insights into eutectic morphological evolution. Phase-field simulation results confirmed the existence of a eutectic colony structure, which has shorter-range (e.g., lamellae) and longer-range (e.g., eutectic colony cell) periodicity,[120] which were predicted by the long-range instability in a linear stability analysis.[125] The overstability condition of small lamellar spacing was studied by phase-field modeling and experiments revealing transverse movement of phase triple junctions not considered in the derivation of the Jackson-Hunt theory.[121] Phase-field simulations of the continuous nucleation of solid phases during eutectic solidification were performed and revealed that the nucleation can suppress instabilities of interfaces between a single solid phase and the eutectic liquid.[122] Also, the formation of a zig-zag type lamellar structure was found and analyzed.[123] Subsequently, the stability of structural defects in lamellar and other unique periodic microstructures not considered in the Jackson-Hunt theory were revealed.[124] The effects of planar geometric confinement on the resulting eutectic microstructures were examined, and several microstructural features rarely seen in experiments were discovered.[126,127] As in all multi-phase materials, interfacial energies play a key role in eutectic microstructure evolution, and thus the effects of anisotropy in interfacial energy were studied.[128,129] The results showed a wide variety of morphological patterns, such as spiral eutectic colony structure, due to interfacial energy anisotropy.[128,129] The effects of the temperature profile were investigated, and a lamellar-to-rod microstructural transition was found in the directional solidification of the eutectic with the temperature gradient direction transverse to the solidification direction.[130] Ternary eutectic

systems, in which three solid phases form simultaneously, were studied for lamellar growth in two dimensions[131] and spiral growth of two-phase rods embedded in a matrix phase in three dimensions.[132-134] Eutectic phase-field models have been employed to simulate many different types of eutectic material systems, including metals and ionic compounds. Figure 2.2 shows various types of eutectic microstructures (including lamellar, colony, rod, and spiral structures) that have been successfully simulated with phase-field models.

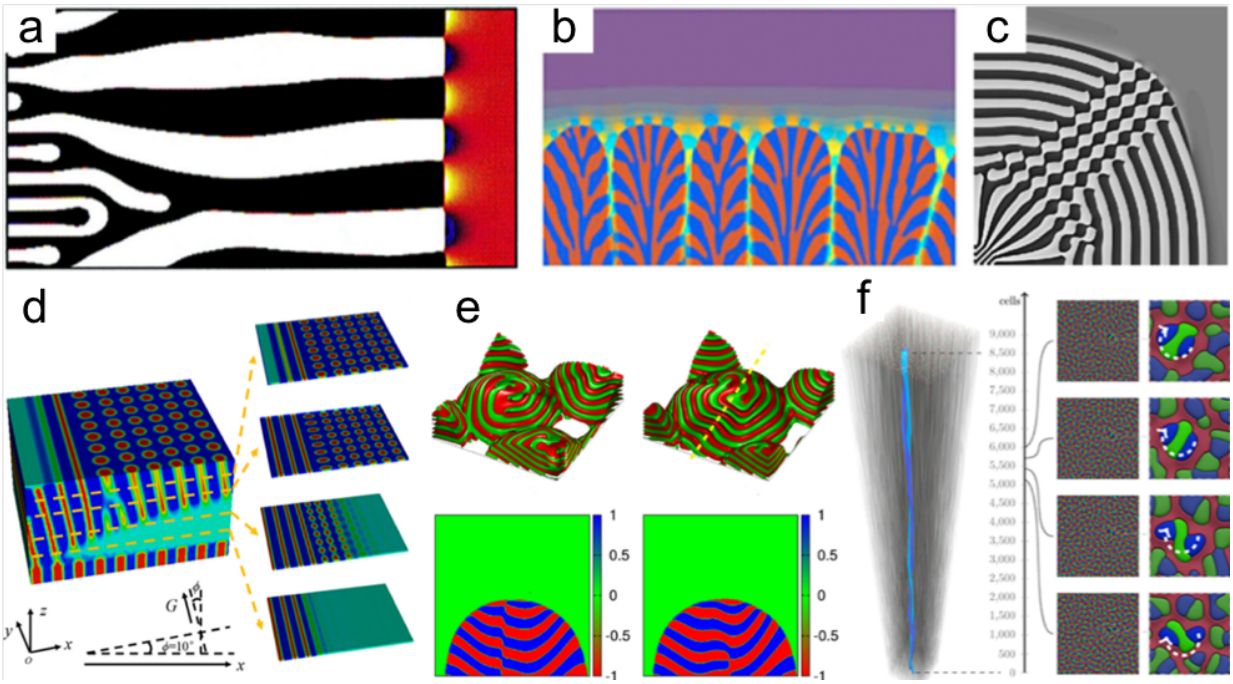

Figure 2.2 Various eutectic pattern formations captured by phase-field modeling: (a) Lamellar structure formation during directional solidification. Reproduced with permission.[108] Copyright 2000, Elsevier. **(b)** Eutectic colony formation during directional solidification. Reproduced with permission.[120] Copyright 2002, American Physical Society. **(c)** Lamellar breakdown during isothermal solidification under thermal noise and continuous nucleation. Reproduced with permission.[122] Copyright 2007, Springer Nature. **(d)** Lamellar-to-rod structure transition during directional solidification due to change in the temperature gradient direction. Reproduced with permission.[130] Copyright 2017, AIP Publishing LLC. **(e)** Spiral eutectic colony pattern formation due to anisotropy in interfacial energies. Reproduced with permission.[129] Copyright 2017, Elsevier. **(f)** Spiral growth of rods during directional solidification of a ternary eutectic. Reproduced with permission.[134] Copyright 2016, Elsevier.

2.1.3 Early Works on Template-Directed Eutectic Solidification

Template-directed assembly is showing promise for controlling the self-organization of eutectic materials to generate microstructures that could have potential optical functionalities. This template-directed solidification could also lead to the emergence of new structures that are not present in either the template or the native eutectic structure. As the variables associated with a template's geometry further broaden an already large phase space, simulation methods would be key to making efficient progress in understanding the microstructural evolution and the development of templates.

State-of-the-art tools like lithography and surface functionalization can be used to design a template matrix with a patterned topography and surface chemistry. With this, the effects of confinement and the interaction between the template pattern and the solidifying eutectic (for surface-selective nucleation) can be combined to tailor the assembly of the phase-separating components. The combination of top-down lithography and bottom-up assembly of materials give opportunities to fabricate large-area, scalable optical materials and widen the scope of constituent structures and materials.

A few cases of template-directed solidification of eutectics have been studied in literature, as reviewed below, wherein factors affecting the solidification process and the final structure are either the template-dictated shape of the solidification front or confinement within the patterned template. The periodicity of the eutectic, λ, is primarily determined by the solidification front velocity, v. Depending on the manner of heat removal from the eutectic melt and the design or composition of the container/template, the solidification front can assume different shapes and orientations. Hence, the template design and template composition are both crucial in determining the shape of the solidification front for a given method.

As one of the initial examples of template-directed solidification of eutectics, it was demonstrated that by forcing the solidification front to curve, either by adjusting the heat-flow pattern or by blocking the eutectic growth with a physical obstacle, the lamellar structures of some eutectics (Pb-Cd, Sn-Cd, and Cd-Zn) transition into rod structures.[135] Over the range of the applied growth rates, the Pb-Cd eutectic always formed an ordered lamellar structure in the absence of obstacles. To produce a curved solidification front, the eutectic was directionally solidified in a graphite boat containing a graphite inset. In this setup, the metal eutectic solidified with a planar solidification front until the front reached the sharp edge of the graphite inset. At the edge, the solidification front curved as it grew around and past the inset obstacle without significant change to the growth rate. However, the lamellae broke down into rod structures as the growth direction curved and pointed out of the plane of the initial growing lamellae. The rods did not extend far from the edge of the graphite inset, rather there was a rapid transition back to lamellae, suggesting that the rods must be growing under unstable conditions. Thus, it was concluded that the sudden change in either the direction of the solidification or the curvature of the solidification front caused by the template led to this unique morphological changes.[135]

In addition to controlling the shape of the solidification front, templates can greatly modify the microstructure of a solidifying eutectic, in particular when the template has characteristic dimensions commensurate to the characteristic spacing of the eutectic structure.[61] Templates have been used to demonstrate the effects of confinement on eutectic solidification with those ranging from one-dimensional structures, such as capillary tubes and porous anodized aluminum oxide, to three-dimensional structures, such as silica opals, which are further discussed below.

Optically transparent eutectic organic alloys are advantageous for studying eutectic solidification, as their transparency enables direct, *in situ* observation of directional

solidification, which provides the details of the evolution of the solidification front and the formation of eutectic structures.[127,136,137] In one study, shown in Figure 2.3, the specimen (capillary tubes with a thin-slab geometry) thickness was modified by changing the spacer thickness, and the rate of solidification was controlled.[127] Samples of succinonitrile (SCN) - (d)-camphor (DC) eutectic were sealed in 5 mm wide glass sample holders ranging in thickness from 15 to 350 μm. The samples were directionally solidified at a range of velocities and the cross-section perpendicular to the solidification direction was imaged using an optical microscope. The eutectic formed a rod structure independent of the specimen thickness, when high growth velocities were used. This showed that the rod morphology was favorable when the characteristic spacing was small. However, at low growth velocities, the characteristic spacing of the eutectic structure was larger and on the order of the specimen thickness; thus under these conditions, the system can be considered to be "confined." For specimen thicknesses (i.e., confining-geometry dimensions) between 30 μm and 140 μm, lamellar patterns of DC and SCN phases are observed. While the volume fraction of SCN-DC would usually result in a rod structure, the ordinarily unfavorable lamellar microstructure formed within a confinement since the lamellar instability modes were blocked as the specimen thickness was smaller than the critical wavelengths of the morphological instability threshold.[123,124] For specimen thicknesses above 140 μm, the bulk microstructure of DC rods in SCN matrix was observed for the same slow growth velocities. These steady-state morphologies that formed at different velocities with the confinement effects of the solidification template showed a bistability in the eutectic pattern. Phase-field modelling was used to confirm these transitions.[123,126,136] Rod-to-lamellar transitions resulting from confinement effects of the template could prove useful in designing specific periodic microstructures in the solidifying eutectic material.

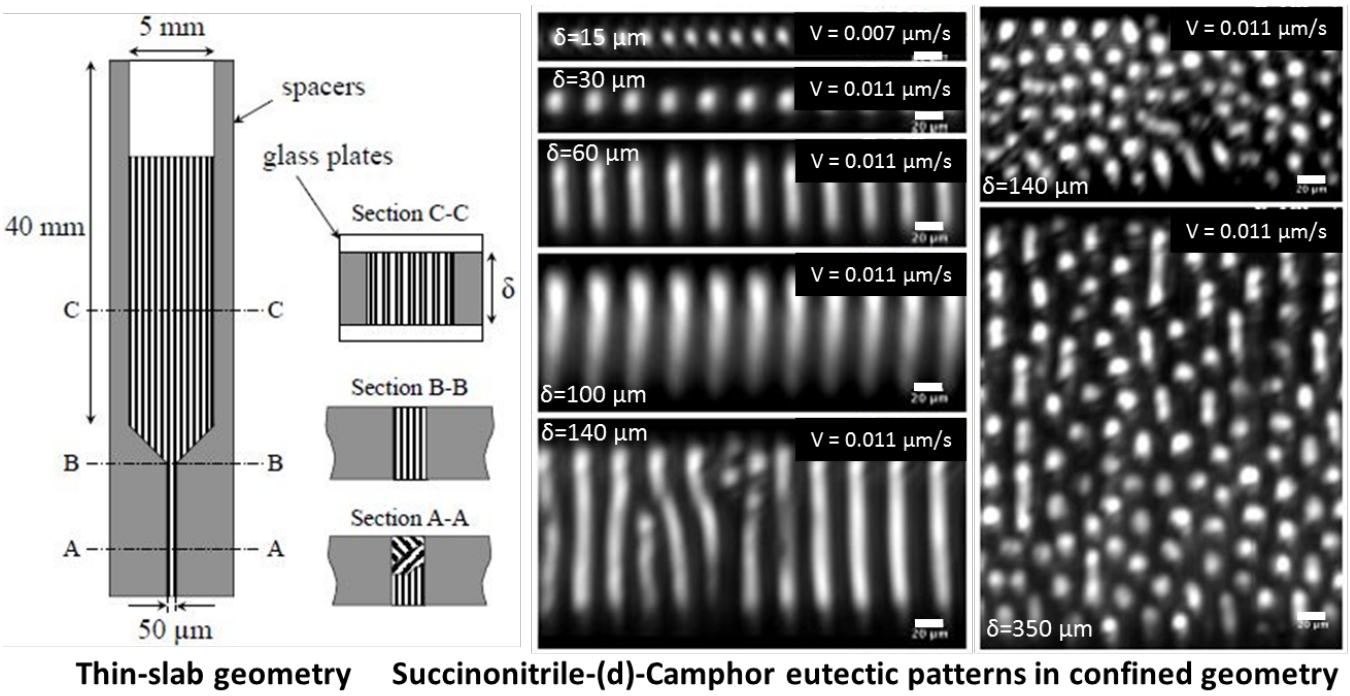

Figure 2.3 Confinement of eutectics during solidification within a thin slab geometry: Succinonitrile - (d)-Camphor eutectic confined in a thin slab geometry with finite thickness (δ). As the thickness varies, the microstructure transitions from lamellar to rod morphology. Scale bars 20 μm. Reproduced under the terms of the CC-BY-NC-SA 3.0 license.[127]

The effect of confinement on the solidification of eutectics has also been studied using microporous anodic aluminum oxide (AAO) as a template. Single-crystal nanowires of Bi-Sn solder eutectic alloy were synthesized by confining its solidification within this porous structure.[138] The AAO templates were infiltrated by the metal eutectics using a setup that enabled evacuating the air from the pores, followed by hydraulic pressure injection of the melt into the pores. The confined Bi-Sn eutectic melt phase-separated within these nanosized pores to form an alternating layer structure (Figure 2.4).[138,139] Given the direction of heat flow (from the top of the template to the bottom surface, where heat is extracted) and the expected solidification direction that results, alternating layers of the eutectic would ordinarily be expected to align along the axis of the cylindrical pores. However, the template-directed eutectic exhibited an unexpected orientation of phase-separation of the Bi and Sn phases. Such phase separation could arise due to

the confinement effects of the small pores on the eutectic. It can be observed in Figure 2.4 that there is not a preferred phase that nucleates at the bottom surface of the template; either Bi or Sn can start solidifying at the bottom surface. This leads to a build-up of the atomic species of the other phase, which subsequently solidifies above the first-forming phase. The overall alternating structure does not have a fixed spacing; rather the Bi and Sn layers are of random lengths, suggesting that a stochastic process, such as nucleation, is playing a role. The phase boundary orientation suggests that this phase-separation process is not a traditional directional solidification of a eutectic, where solid-phase separation occurs in a lateral direction, parallel to the solidification front.[15]

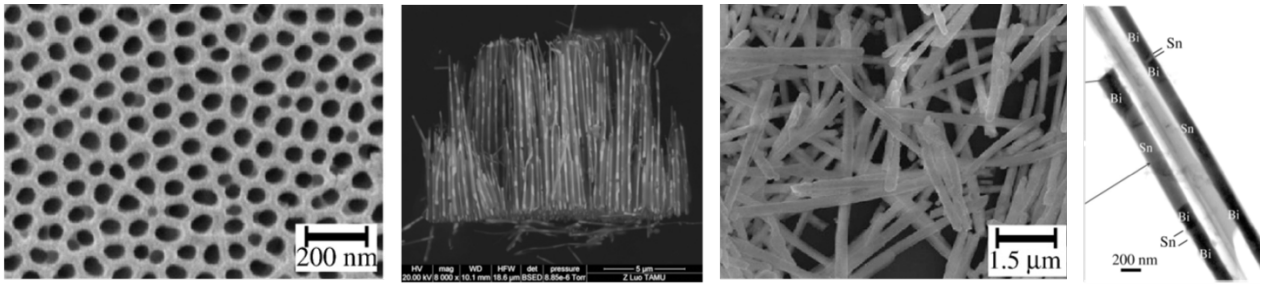

Figure 2.4 Confinement of eutectic during solidification in AAO template: Bi-Sn eutectic as solidified within the channels of AAO template. This provides a novel approach to synthesize large-area nanowires. Reproduced with permission.[138,139] Copyright 2009, Elsevier.

The AAO template-directed eutectic solidification presents a novel method to obtain multi-phase nanowires of various chemistries, however lack of control over the thickness of the individual layers could be a concern for optical applications. Future investigations may include eutectic materials of inherent structures such as rods, or spiral, directed by the pores of the AAO template, possibly resulting in helical morphologies.[140]

The confinement of the solidifying eutectic within pores offers a novel method to obtain small feature sizes in the eutectic structure that may not be easy to obtain by simple directional solidification. These pores can also be created via three-dimensional templates, as reported in the

case where AgCl-KCl salt eutectic was infiltrated into a silica opal template.[61] The nanosized gaps between the individual silica colloidal particles gave rise to new morphological features with sizes significantly smaller than that of either the template or the inherent bulk eutectic, as shown in Figure 2.5.[61] The emergence of the three-dimensional mesostructures was mainly determined by the gap size (necks) between the densely packed silica colloidal particles. When the gaps were sufficiently large, the lamellar phase separation was facilitated in such a manner that the eutectic maintained a lamellar structure locally. However, there was no long-range order in the complex morphology of AgCl and KCl lamellae. In the case where this gap size was small, i.e., the colloidal particle diameter was small, a random agglomerate of AgCl and KCl phases was observed with no short- or long-range order.[61]

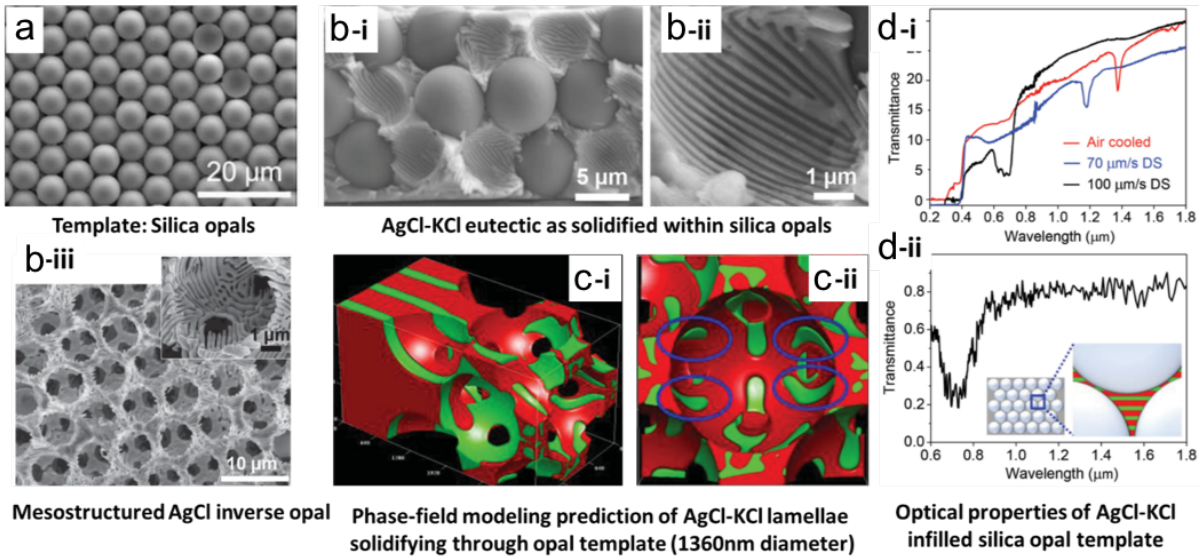

Figure 2.5 Silica opal template-directed solidification of eutectics: AgCl-KCl eutectic directionally solidified within silica opal template shows a complex morphology of the lamellar eutectic. Reproduced with permission.[61] Copyright 2015, Wiley-VCH.

This three-dimensional mesostructured network of AgCl-KCl eutectic imposed by the template exhibited intriguing optical properties that could be changed by varying the rate of directional solidification. Depending on the lamellar spacing of the mesostructured eutectic,

sharp dips in the transmission spectrum were observed around 1.42 μm, 1.18 μm or 690 nm, corresponding to the features in the complex morphology of the template-directed eutectic (Figure 2.5d).[61] This was confirmed with finite-difference time-domain optical simulations for a simplified structure of alternating dielectric layers (assuming the refractive index of 1.49 and 2.09 for KCl and AgCl, respectively) infiltrated within a matrix of silica spheres. The absence of any optical response from the opal template suggested that the mesostructure retains optical features from the lamellar eutectic, even when infiltrated within a periodic array of silica colloidal particles.[61]

2.1.4 Eutectic-Template Considerations

There are a large number of material combinations that undergo eutectic solidification.[56,57,59,60,141,142] However, it is challenging to test all of these material chemistries to obtain the desired template-directed eutectic optical materials. Thus, it is critical to select the best material system for a given application and for ease of processing. Processing challenges include limitations of the ambient environment control, undesired chemical reactions, and the thermal and chemical stability of the template materials. The template features should be durable and strong enough to tolerate stresses from volume changes during the melting and solidification of the eutectic materials. In some cases, processes may require rapid heating or quenching and thus the template materials must be able to survive large thermal gradients.

The ideal template fabrication technique should provide features at the desired length scales. For model studies, lithographic techniques are probably best, given their precision and applicability to a diverse range of geometric designs.[9,143] The ability to incorporate a diverse set of materials is important, as the constituent materials play a major role in controlling heat flow, and therefore the temperature profile imposed on the solidifying eutectic, which often strongly affects the resultant microstructure.[144]

Another consideration is the compatibility between the template surface and the solidifying eutectic material. Chemical stability and wettability are particularly important for template-directed eutectic solidification. Surface modifications, such as metal or oxide coatings, could provide favorable, stable surface chemistries and allow controlled flow of the liquid eutectic material over the template surface. The template material must also have a melting temperature higher than that of the eutectic temperature to avoid thermal instability or melting of the template. For some applications, it may also be important for the template to be reusable.

For cases when certain materials with desired properties cannot be directly solidified through a template, a template-directed eutectic could itself act as a template for other materials. This can be achieved by selectively etching one of the phases and infiltrating with new materials.[62,145] This replacement technique could be especially advantageous in synthesizing optical metasurfaces and metallodielectric optical metamaterials.

There are great opportunities in the design space for the template-directed solidification of eutectics to tailor the light-matter interactions for optical metamaterial applications. However, such applications require a high level of control over the eutectic morphologies and their degree of order, both at short and long ranges. Along with appropriate template design, this will require precise control over the rate and direction of heat flow in the experimental design, allowing steady-state solidification conditions suitable to produce a high degree of order. If this is realized, the potential list of applications will include optical, electronic, magnetic, thermal, photovoltaic and mechanical functionalities. To date, reports on template-directed organization of eutectics have been predominantly limited to lamellar eutectic systems. By utilizing other eutectic structures with rod, irregular, or complex motifs, new classes of template-directed eutectic organization can be explored.

2.2 Hindered Grain Boundary Diffusion

2.2.1 Grain Boundary Effects on Materials Properties

Defects, such as grain boundaries in polycrystalline solids, often have a significant effect on material properties.[48] Grains and grain boundaries in materials arise from various processing techniques such as sintering, agglomeration of particles, or nucleation and growth. The unique configuration of atoms at grain boundaries, in which bonding structures differ from atoms in the intrinsic lattice, lead to differences in mechanical and/or transport behavior between grain boundaries and bulk regions. In many cases, materials can be designed to take advantage of these grain boundary effects, such as improving creep strength, ductility, corrosion resistance, and damage resistance in metallic alloys.[146-149]

Mass transport is a vital phenomenon in a vast range of materials, from ion transport in solid oxide fuel cells[26,27,29] and batteries[41-43] to metal diffusion barrier layers.[150,151] Due to lower density and a high degree of defects at grain boundaries, often, mass transport is enhanced compared to the bulk. For example, it has long been known that the increased rate of diffusion at grain boundaries has accelerated sintering processes.[152-154] In functional materials, grain boundaries have been shown to increase transport rates of charge-carrying species in photovoltaics[33-35] and battery materials,[36,37] as well as enhancing dopant diffusion rates in polycrystalline silicon.[32]

The examples listed thus far have all been cases where grain boundaries enhanced the rate of diffusion; however, some materials systems exhibit the opposite behavior, in which grain boundaries act to hinder transport. In the solid oxide fuel cell material yttria-stabilized zirconia (YSZ), space charge layers and oxygen vacancy depletion at grain boundaries decrease the diffusivity of oxygen ions at the grain boundaries compared to the bulk.[38,155] The decrease in diffusivity at grain boundaries becomes particularly important for performance in nanocrystalline

YSZ, in which the effects of the grain boundaries become more prominent as the grain boundary density increases.[39] Battery cathode particles often consist of agglomerations of smaller particles that form dense, polycrystalline structures.[41-43] During electrochemical charging and discharging, stress from volumetric changes may cause decohesion and cracks to form at the grain boundaries of the cathode particle which obstruct ionic transport and negatively affect battery performance.[41] Hydrogen diffusion in aluminum is hindered across certain grain boundary configurations, though enhanced diffusion parallel to grain boundaries is observed.[156] Similarly, helium diffusivity is decreased in tungsten grain boundaries.[157] In organic semiconductors, grain boundaries can, at times, act as traps for charge carriers.[158] Once the trap site is occupied by a charged species, it will repel other like-charged carriers and thus transport is obstructed at the grain boundary. Likewise, there are biomedical instances of hindrance, such as medicine delivery to tumors where diffusion may be impeded at membranes in vasculature.[159] In addition to the hindering effects of grain boundaries on mass transport, grain boundaries can inhibit thermal transport as well.[160]

2.2.2 Grain Boundary Diffusion Modeling

Models have been developed for investigating systems that exhibit enhanced grain boundary diffusion. Fisher proposed a numerical model to predict the penetration of a diffusing species with enhanced transport at surfaces and grain boundaries.[48] The model was later adapted using the Smoothed Boundary Method to develop a mesoscale model applicable to any arbitrary polycrystalline geometry and the diffusional impedance spectra of lithium ion battery materials were investigated.[47] Enhanced grain boundary diffusion has also been explored in nanocrystalline copper by employing molecular dynamics simulations.[161]

The extent of modeling of hindered grain boundary diffusion has been limited. Molecular dynamics simulations were utilized to study the hindrance effects of grain boundaries in the YSZ

solid oxide fuel cell material.[39] Kinetic Monte Carlo simulations have revealed grain boundary orientations that inhibit helium diffusion in tungsten.[162] These investigations were limited to bicrystals. One work, which examined diffusion in a total of four grains, combined kinetic Monte Carlo and molecular dynamics simulations to demonstrate a method for studying asymmetric grain boundary structures of plasma-facing and their impurity retention behavior. A model which could explicitly account for the entire polycrystalline microstructure (or at least a representative volume) of a material with hindered diffusion at grain boundaries does not yet exist in literature.

Nevertheless, there are mean-field approaches that seek to predict the effective diffusivity – though not the dynamically evolving concentration – of polycrystalline structures by making assumptions about the grain boundary geometry. One such approach is Hart's equation, which assumes all grain boundaries are parallel to each other and oriented along the direction of macroscopic diffusion.[50] Essentially, this description is simply the rule of mixtures, in which the effective diffusivity is expressed as the average of the grain boundary and bulk diffusivities, weighted by their respective volume fractions. Another mean-field approximation is the Maxwell Garnett equation, where grain boundaries are assumed to have spherical shapes.[51] These expressions and their comparisons to models presented in this dissertation are discussed in more detail in Chapters 7 and 8.

Chapter 3: Methods

3.1 Template-Directed Eutectic Solidification

3.1.1 Eutectic Solidification Phase-Field Model

For our phase-field model, we use a combination of the eutectic solidification model developed by Folch and Plapp[112] and the Smoothed Boundary Method (SBM) developed by Yu.[163] We begin by describing the base phase-field model.

The phase of each point in the system is described by three nonconserved order parameters, (p_α, p_β, p_L). The order parameters for the two solid phases, denoted by α and β, and the liquid phase, denoted by L. are constrained such that their sum is one (i.e., $p_\alpha + p_\beta + p_L = 1$). In phase i, $p_i = 1$ and $p_j = p_k = 0$, where $i \neq j \neq k$. The binary interfaces and triple points have order parameter values between zero and one. The order parameters evolve and reduce a free energy, which is a volume integral of the free energy density f described by:

$$f = Kf_{grad} + Hf_p + Xf_c \tag{3.2}$$

where K is a constant with dimensions of energy per unit length and H and X are constants with dimensions of energy per unit volume. The free energy density is made up of three contributions: the gradient free energy density, f_{grad}, the phase-field free energy density, f_p, and the chemical free energy density, f_c. The gradient free energy density is dependent on the spatial derivative of the order parameters:

$$f_{grad} = \frac{1}{2}\sum_i (\nabla p_i)^2 \tag{3.2}$$

The phase-field free energy density has a triple well construction with minima at the bulk values of the order parameters. More specifically, it is a sum of double wells:

$$f_p = \sum_i {p_i}^2 (1 - p_i)^2 \tag{3.3}$$

The chemical free energy density is necessary to tilt the triple well construction such that one phase is preferred over the others at certain compositions and temperatures. It is described by:

$$f_c = \sum_i g_i (B_i - \mu A_i) \tag{3.4}$$

where g_i is a function that raises the energy well of phase *I* and μ is the chemical potential. A_i and B_i are the scaled equilibrium concentration and equilibrium chemical free energy, respectively, for the corresponding phase, which are explained in further detail later. The evolution of the order parameters to reduce the free energy is described by an Allen-Cahn equation:

$$\tau \frac{\partial p_i}{\partial t} = \nabla^2 p_i + \frac{2}{3}\left[-2p_i(1-p_i)(1-2p_i) + \sum_{j \neq i} p_j\left(1-p_j\right)\left(1-2p_j\right)\right] + \tilde{\lambda}\sum_j \left.\frac{\partial g_j}{\partial p_i}\right|_{p_\alpha + p_\beta + p_L = 1} \left(\mu A_j - B_j\right) \tag{3.5}$$

where τ is the relaxation time, t is the simulation time, and $\tilde{\lambda}$ is a coupling constant ($\tilde{\lambda} = X/H$). All interfacial energies are assumed to be equal, though a small modification to include anisotropic interfacial energies can be found in Ref. 112 along with the derivation for Equation 3.5.

The chemical composition of the simulated system is calculated in terms of the chemical potential. The flux of the solute, *J*, is described by Fick's first law:

$$J = -Dp_L \nabla \mu \tag{3.6}$$

Here, the diffusion coefficient, D, is multiplied by the liquid order parameter, p_L, because the diffusivity in the solid is negligible compared to the diffusivity in the liquid. This gives us a one-sided model in which there is no diffusion in the solid. However, because the phase-field model frequently takes an interface thickness that is greater than that of the physical system, an anti-trapping current term must be added to avoid solute being trapped in the interface. This anti-trapping current adds a flux normal to the solid-liquid interface into the liquid that exactly counteracts the artificial solute trapping effect of the wide interface. Therefore, the flux becomes

$$J = -Dp_L \nabla \mu - 2aW\hat{n}_L \sum_{i=\alpha,\beta} (A_i - A_L)(-\hat{n}_L \cdot \hat{n}_i) \frac{\partial p_i}{\partial t} \tag{3.7}$$

where *W* is the interface thickness and $\hat{n}_i$ is the unit vector normal to the phase i interface. The constant $a = 1/(2\sqrt{2})$ is chosen to exactly counterbalance solute trapping while eliminating the spurious effects dependent on interface thickness (i.e., artificial surface diffusion, interface stretching, and chemical potential jump at the interface).[164] With this flux, the chemical potential evolves in time according to the diffusion equation:[112]

$$\frac{\partial \mu}{\partial t} = \nabla \cdot (Dp_L \nabla \mu) - \sum_i A_i \frac{\partial p_i}{\partial t} + 2a \sum_{i=\alpha,\beta} (A_i - A_L)(-\hat{n}_L \cdot \hat{n}_i) \nabla \cdot \left(\hat{n}_i \frac{\partial p_i}{\partial t} \right) \tag{3.8}$$

The driving force toward solidification in the simulation depends on the temperature. In the isothermal solidification case, the temperature profile is a constant value below T_E throughout the system. In the directional solidification case, the initial location of the eutectic temperature isotherm (y_{int}) in the y-direction (growth direction) is an input as an initial

condition. In most cases, y_{int} is just a single value representing a planar eutectic temperature isotherm (leading to a planar solidification front); however, experimental observation or heat transfer simulation results can justify a y_{int} that is variable across the x- and z-directions. A linear thermal gradient G in the y-direction is used to calculate the temperature away from the eutectic temperature isotherm. Finally, the pulling velocity v_p of the system through the thermal gradient is used to update the temperature profile over time. The equilibrium chemical free energy density for phase i is dependent on the temperature as described by

$$B_i = A_i \frac{(T - T_E)}{m_i \Delta C} = A_i \frac{G\big(y - v_p t - y_{int}(x,z)\big)}{m_i \Delta C} \tag{3.9}$$

Assuming the liquidus and solidus lines are parallel, A_i is equal to the scaled concentration of phase i, $c_i = (C_i - C_E)/\Delta C$, where C_i is the equilibrium concentration of phase i and C_E is the eutectic concentration. A_L and B_L are zero because only the relative differences between phases i and L are important.

The remaining undefined terms are the coupling constant $\tilde{\lambda}$ and the relaxation time τ. They are described by

$$\tilde{\lambda} = \frac{W a_1}{2\bar{d}} \left(\frac{1}{|A_\alpha|} + \frac{1}{|A_\beta|} \right) \tag{3.10}$$

$$\tau = \frac{\tau_\alpha + \tau_\beta}{2} + \frac{\tau_\alpha - \tau_\beta}{2} \frac{(p_\beta - p_\alpha)}{(p_\alpha + p_\beta)} \tag{3.11}$$

where $a_1 = \sqrt{2}/3$ and $\bar{d}$ is the capillary length $\bar{d} = (\sigma_i T_E)/(L_i |m_i| \Delta C)$. The relaxation times τ_α and τ_β are defined by

$$\tau_i = \frac{\tilde{\lambda} {A_i}^2 W^2 a_2}{D} \tag{3.12}$$

where $a_2 = 1.175$.[112] The constants a_1 and a_2 are chosen such that errors associated with an artificially large interface vanish, as discussed in Ref. 164.

The model is discretized in space using a centered finite difference scheme with a grid spacing of Δx=0.8 or less. The temporal discretization follows a forward Euler time stepping scheme where the time step Δt is 80% of the lesser of $(1/2)^d \Delta x^2/D$ and $(1/2)^d \Delta x^2 \tau_i$, where d is the number of dimensions in the simulation. Variables and spatial derivatives are nondimensionalized. Lengths and times are nondimensionalized using the factors W and $\bar{\tau} = (\tau_\alpha + \tau_\beta)/2$, respectively. Because W is the interfacial thickness of the phase-field model, a sufficiently small W is necessary to ensure accuracy. For example, to keep a sufficiently high ratio of bulk to interface, an interfacial thickness is chosen such that the ratio of the eutectic spacing to W is 64. The computational domain is chosen to be large enough in the growth direction to ensure that the variations of the chemical potential in the x- and z-directions at the higher-temperature region of the domain are sufficiently small. A one-dimensional solution for the chemical potential equation extends in the y-direction beyond the edge of the conventional computational domain (i.e., the two- or three-dimensional domain), as shown schematically in Figure 3.1 for a two-dimensional simulation. Because there is no phase transformation in that one-dimensional region, only a simplified diffusion equation is solved:

$$\frac{\partial \mu}{\partial t} = D \nabla^2 \mu \tag{3.13}$$

This one-dimensional domain is chosen to be at least as long as the diffusion length, defined by D/v. The boundary condition at the end of this one-dimensional domain is a Dirichlet boundary condition set to the value of the eutectic composition while the other edge is set to the average value of the composition just inside the conventional domain (discarding values corresponding to positions where $\psi < 0.5$). The boundary conditions in the x- and z-directions are periodic unless

geometric confinement is being investigated, in which case the boundary conditions may instead be no-flux. The y-direction boundary conditions are no-flux, but in practice it does not matter because the solid does not evolve at the cold edge and there is only liquid at the hot edge of the domain. The computational domain shifts in the y-direction by one grid point every time the solidification front moves forward by one grid point. In doing so, the low-temperature end of the domain is discarded and new grid points are added to the high-temperature end of the domain with the chemical composition imposed by the one-dimensional solution beyond the domain described above.

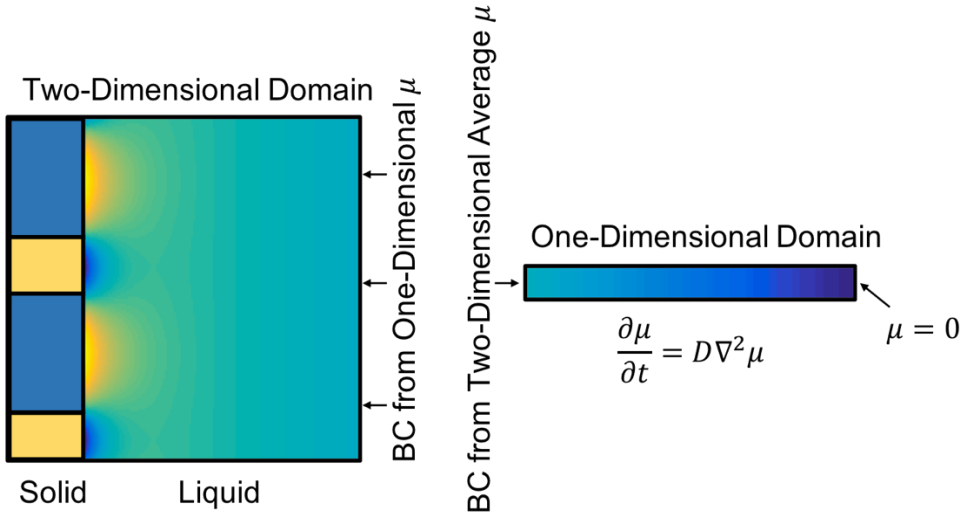

Figure 3.1 Two-dimensional eutectic solidification domain schematic: The chemical potential is solved in two-dimensions in the conventional domain, shown on the left. The domain is extended with a one-dimensional domain, shown on the right. The boundary condition (BC) imposed on the right side of the two-dimensional domain comes from the chemical potential on the left side of the one-dimensional domain. The BC imposed on the left side of the one-dimensional domain comes from the average of the chemical potential on the right side in the two-dimensional domain. The BC imposed on the right side of the one-dimensional domain is zero, the eutectic composition.

3.1.2 Template-Eutectic Interactions with the Smoothed Boundary Method

Because the template is static and impermeable, the diffusion equation must be modified such that no-flux boundaries are enforced at the template-eutectic interface. We accomplish this

by using the smoothed boundary method and introducing another field variable, the domain parameter ψ.[163] Like the order parameters, the domain parameter varies between zero and one. In the template, the domain parameter is zero and in the eutectic, the domain parameter is one. Again, the regions with values between zero and one represent the interface between the template and eutectic. Multiplying both sides of Equation 3.8 by ψ gives

$$\psi\frac{\partial\mu}{\partial t} = \psi\nabla\cdot(Dp_L\nabla\mu) - \psi\sum_i A_i\frac{\partial p_i}{\partial t} + 2a\psi\sum_{i=\alpha,\beta}(A_i - A_L)(-\hat{n}_L\cdot\hat{n}_i)\nabla\cdot\left(\hat{n}_i\frac{\partial p_i}{\partial t}\right) \tag{3.14}$$

We can then manipulate Equation 3.14 using the identity

$$\psi\nabla\cdot(Dp_L\nabla\mu) = \nabla\cdot(\psi Dp_L\nabla\mu) - \nabla\psi\cdot(Dp_L\nabla\mu) \tag{3.15}$$

to obtain a new equation:

$$\psi\frac{\partial\mu}{\partial t} = \nabla\cdot(\psi Dp_L\nabla\mu) - \nabla\psi\cdot(Dp_L\nabla\mu) - \psi\sum_i A_i\frac{\partial p_i}{\partial t} + 2a\psi\sum_{i=\alpha,\beta}(A_i - A_L)(-\hat{n}_L\cdot\hat{n}_i)\nabla\cdot\left(\hat{n}_i\frac{\partial p_i}{\partial t}\right) \tag{3.16}$$

To enforce a no-flux boundary at the template interface, $\hat{n}_\psi\cdot J$ must be zero, where $\hat{n}_\psi$ is the unit vector normal of the template. Substituting Eq. 3.7 into $\hat{n}_\psi\cdot J = 0$ gives the equation

$$-\frac{\nabla\psi}{|\nabla\psi|}\cdot\left(-Dp_L\nabla\mu - 2aW\hat{n}_L\sum_{i=\alpha,\beta}(A_i - A_L)(-\hat{n}_L\cdot\hat{n}_i)\frac{\partial p_i}{\partial t}\right) = 0 \tag{3.17}$$

Rearranging gives

$$\nabla\psi\cdot(Dp_L\nabla\mu) = \nabla\psi\cdot\left(-2aW\hat{n}_L\sum_{i=\alpha,\beta}(A_i - A_L)(-\hat{n}_L\cdot\hat{n}_i)\frac{\partial p_i}{\partial t}\right) \tag{3.18}$$

Substituting this back into Equation 3.15 and dividing both sides by ψ, we arrive at the final diffusion equation:

$$\frac{\partial \mu}{\partial t} = \frac{1}{\psi}\nabla \cdot (\psi D p_L \nabla \mu) - \frac{\nabla\psi \cdot \left(-2aW\hat{n}_L \sum_{i=\alpha,\beta}(A_i - A_L)(-\hat{n}_L \cdot \hat{n}_i)\frac{\partial p_i}{\partial t}\right)}{\psi} - \sum_i A_i \frac{\partial p_i}{\partial t} + 2a \sum_{i=\alpha,\beta}(A_i - A_L)(-\hat{n}_L \cdot \hat{n}_i)\nabla \cdot \left(\hat{n}_i \frac{\partial p_i}{\partial t}\right) \tag{3.19}$$

Note that modifying the diffusion equation with the domain parameter only has an effect where $\nabla\psi$ is nonzero; this is only the case at the template interface, where the no-flux boundary is applied. The template interface is chosen to have the shape of a hyperbolic tangent function:

$$\psi(x) = \frac{1}{2}\left(1 + \tanh\left(\frac{x - x_0}{2}\right)\right) \tag{3.20}$$

where x is the spatial coordinate in the x-direction and x_0 is the location of center of the interface.

Additionally, the SBM can be employed to impose template boundary conditions on the phase-field evolution equation. Equilibrium contact angle boundary conditions can be applied by modifying Equation 3.5 in the same manner as the diffusion equation was modified with a no-flux boundary condition, but instead of setting $\hat{n}_\psi \cdot J$ to zero, we instead use the equation

$$-\frac{\nabla\psi}{|\nabla\psi|} \cdot \frac{\nabla p_i}{|\nabla p_i|} = \cos\theta_i \tag{3.21}$$

where θ_i is the contact angle at the phase i-liquid-template junction. The negative on the left hand side comes from the fact that the gradient of ψ points away from the template (i.e., $\psi = 0$ in the template). We multiply by ψ on both sides of Equation 3.5 to obtain

$$\psi\tau\frac{\partial p_i}{\partial t} = \psi\nabla^2 p_i + \psi\frac{2}{3}\left[-2p_i(1-p_i)(1-2p_i) + \sum_{j\neq i} p_j\left(1-p_j\right)\left(1-2p_j\right)\right] + \psi\,\tilde{\lambda}\sum_j \left.\frac{\partial g_j}{\partial p_i}\right|_{p_\alpha+p_\beta+p_L=1}\left(\mu A_j - B_j\right) \tag{3.22}$$

and subsequently use the identity

$$\psi\nabla^2 p_i = \nabla\cdot(\psi\nabla p_i) - \nabla\psi\cdot\nabla p_i \tag{3.23}$$

as a substitute in Equation 3.22 to obtain

$$\psi\tau\frac{\partial p_i}{\partial t} = \nabla\cdot(\psi\nabla p_i) - \nabla\psi\cdot\nabla p_i + \psi\frac{2}{3}\left[-2p_i(1-p_i)(1-2p_i) + \sum_{j\neq i} p_j\left(1-p_j\right)\left(1-2p_j\right)\right] + \psi\,\tilde{\lambda}\sum_j \left.\frac{\partial g_j}{\partial p_i}\right|_{p_\alpha+p_\beta+p_L=1}\left(\mu A_j - B_j\right) \tag{3.24}$$

Rearranging Equation 3.22 as

$$\nabla\psi\cdot\nabla p_i = -\,|\nabla\psi||\nabla p_i|\cos\theta_i \tag{3.25}$$

and substituting it into Equation 3.24 and dividing both sides by ψ gives the final phase-field evolution equation modified to include a template-solid-liquid contact angle boundary condition:

$$\tau\frac{\partial p_i}{\partial t} = \frac{1}{\psi}\nabla\cdot(\psi\nabla p_i) + \frac{|\nabla\psi||\nabla p_i|}{\psi}\cos\theta_i$$
$$+\frac{2}{3}\left[-2p_i(1-p_i)(1-2p_i) + \sum_{j\neq i} p_j\left(1-p_j\right)\left(1-2p_j\right)\right] \tag{3.26}$$
$$+\tilde{\lambda}\sum_j \frac{\partial g_j}{\partial p_i}\Bigg|_{p_\alpha+p_\beta+p_L=1}\left(\mu A_j - B_j\right)$$

3.1.3 Parameterization

For the majority of the template-directed eutectic solidification simulation work, the model was parameterized for the AgCl-KCl eutectic system. AgCl-KCl was chosen for its relatively low eutectic temperature (compared to that of the template materials silicon, silica, and nickel), its ability to have KCl selectively etched with water, and its inherent, regular lamellar structure. The materials constants for AgCl-KCl are shown in Table 3.1. This phase-field model does not account for each phase having a different molar volume; therefore, the eutectic composition is set such that the volume fraction is preserved.

Table 3.1 AgCl-KCl materials parameters used in the phase-field simulations.

Quantity	Symbol	Value	Reference
Liquidus slope of AgCl	m_{AgCl}	-542 K/mol	165
Liquidus slope of KCl	m_{KCl}	837 Kmol	165
Eutectic temperature	T_E	319°C	165
Eutectic composition	C_E	30 mol%	165
Composition of AgCl at T_E	C_{AgCl}	0 mol%	165
Volume fraction of KCl at T_E	V_E	38 vol.%	165
Composition of KCl at T_E	C_{KCl}	100 mol%	165
AgCl-Liquid interfacial energy	σ_{AgCl-L}	154 mJ/m^2	Assume same as σ_{KCl-L}
KCl-Liquid interfacial energy	σ_{KCl-L}	154 mJ/m^2	166
AgCl-KCl interfacial energy	$\sigma_{AgCl-KCl}$	154 mJ/m^2	Assume same as σ_{KCl-L}
Latent heat of fusion per unit volume for AgCl	L_{AgCl}	5.12×10^8 J/m^3	167
Latent heat of fusion per unit volume for KCl	L_{KCl}	6.93×10^8 J/m^3	167
Diffusion coefficient	D	3.79×10^{-9} m^2/s	62

3.1.4 Initial Condition

Unless stated otherwise, the initial condition of the simulation contains a seed with a lamellar structure. The initial lamellar spacing corresponds to expected lamellar spacing predicted by the Jackson-Hunt[57] theory based on the materials parameters and solidification velocity. For some simulations, it is important to break the symmetry of the initial condition to enable a more natural evolution or to avoid metastable states. In such cases in two-dimensions,

the width of each lamellar pair is varied randomly by up to ±10% of the nominal lamellar spacing while preserving the volume of the domain. In three-dimensions, the same lamellar pair width variation procedure is followed by the local width of each lamellar layer being sinusoidally perturbed along the other lateral direction up to ±10% of the nominal width to break symmetry I the remaining direction.

3.2 Heat Transfer Calculation for Eutectic Printing

This section is largely a reproduction of part of the article titled "High Operating Temperature Direct Ink Writing of Mesoscale Eutectic Architectures," previously published in Advanced Materials in 2017.[62] The model described below was used to find the steady-state temperature profiles and solidification velocities in printed filaments of eutectic material (see Chapter 4 Section 4.1).

In the case of eutectic printing, a filament of initially molten eutectic is deposited onto a cold substrate by a nozzle moving at a constant velocity. The steady-state temperature profile of the center of the filament (comprising both the solidified and molten regions of the printed eutectic) is simulated by solving an equation that accounts for the thermal diffusion and the velocity due to the moving frame of reference, which follows the motion of the nozzle at a printing speed $\tilde{v}$

$$\frac{\partial \tilde{T}}{\partial \tilde{t}} = \tilde{\alpha}\tilde{\nabla}^2\tilde{T} + \tilde{v}\frac{\partial \tilde{T}}{\partial \tilde{y}} \tag{3.27}$$

where $\tilde{T}$ is the temperature, $\tilde{t}$ is the time, and $\tilde{\alpha}$ is the thermal diffusivity. Tildes denote non-dimensionalized variables, which are scaled by the length scale W_h = 2.5×10^{-5} m and the time scale τ_h = 2.5×10^{-3} s. W_h and τ_h are on the order of α/v and α/v^2, respectively. Temperatures are nondimensionalized by a factor of 1 K. The x-axis is parallel to the width of the filament, the

y-axis is parallel to the printing direction, and the z-axis is parallel to the thickness of the filament. The printed filament is treated as a rectangular prism, where the bottom surface (positioned at $\tilde{z} = 0$) is in contact with the substrate and is subjected to Newton's law of cooling:

$$J_{\tilde{z}=0} = \tilde{h}_{sub}\left(\tilde{T}_{\tilde{z}=0} - \tilde{T}_{sub}\right) = -\tilde{k}\left.\frac{\partial \tilde{T}}{\partial \tilde{z}}\right|_{\tilde{z}=0} \tag{3.28}$$

where J is the heat flux, $\tilde{h}_{sub}$ is the heat transfer coefficient of the substrate, $\tilde{T}_{sub}$ is the substrate temperature, and $\tilde{k}$ is the thermal conductivity of the eutectic. Equation 3.28 is used to enforce a Neumann boundary condition at the substrate-filament interface. Neumann boundary conditions corresponding with the air-filament interfaces are enforced at the edges and top of the filament in a similar manner as Equation 3.28. Equations 3.29 and 3.30 describe the boundary condition at the top and edges of the filament, respectively.

$$J_{\tilde{z}=L_z} = \tilde{h}_{air}\left(\tilde{T}_{\tilde{z}=L_z} - \tilde{T}_{air}\right) = -\tilde{k}\left.\frac{\partial \tilde{T}}{\partial \tilde{z}}\right|_{\tilde{z}=L_z} \tag{3.29}$$

$$J_{\tilde{x}=0,L_x} = \tilde{h}_{air}\left(\tilde{T}_{\tilde{x}=0,L_x} - \tilde{T}_{air}\right) = -\tilde{k}\left.\frac{\partial \tilde{T}}{\partial \tilde{x}}\right|_{\tilde{x}=0,L_x} \tag{3.30}$$

where h_{air} is the heat transfer coefficient to air and T_{air} is the temperature of the air. Equation 3.29 is evaluated at the top of the filament at position L_z, the height of the filament. Equation 3.30 is evaluated at the edges of the filament at position zero and at position L_x, the width of the filament. In the y-direction, no-flux boundaries are applied at the front and back of the filament domain. A cylindrical Dirichlet boundary represents the nozzle and is set to the temperature of the nozzle, T_{nozzle}. This cylinder is centered at the maximum y-coordinate of the filament domain and has an outside diameter of d_{noz}. The diameter of the filament is taken to be 3% greater than the nozzle diameter to account for the slight spreading of the molten ink observed

during the printing process. The gap height between the nozzle exit and the substrate is set to 10 μm. See Figure 3.2 for a schematic representation of the domain.

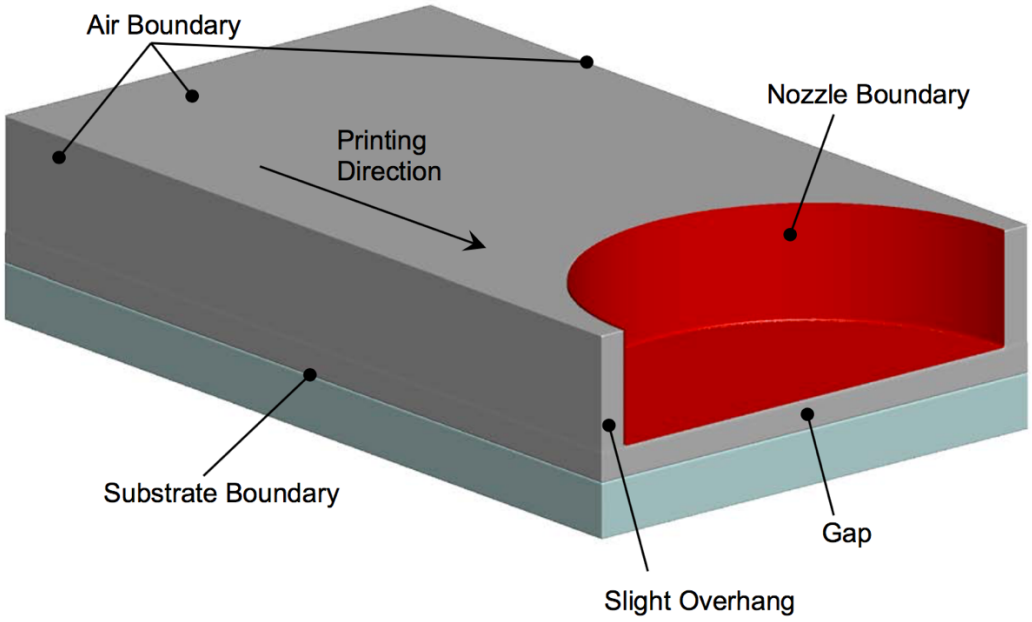

Figure 3.2 Filament domain schematic: Schematic representation of the domain for 3D eutectic filament heat transfer simulations.

Thermal properties differ between the molten and solidified AgCl-KCl eutectic material. A smoothly varying function to interpolate between liquid and solid values of the thermal diffusivity $\tilde{\alpha}$ and the thermal conductivity $\tilde{k}$ as a function of temperature is needed for numerical convergence. The interpolation function g is given by

$$g = \frac{3(\tilde{T} - \tilde{T}_s)^2}{(\tilde{T}_L - \tilde{T}_s)^2} - \frac{2(\tilde{T} - \tilde{T}_s)^3}{(\tilde{T}_L - \tilde{T}_s)^3} \tag{3.31}$$

where $\tilde{T}_s$ and $\tilde{T}_L$ are the lower and upper bounds of the temperature range used for the interpolation. Figure 3.3a shows a plot of the interpolation function. For temperatures between $\tilde{T}_s$ and $\tilde{T}_L$, $\tilde{\alpha}$ and $\tilde{k}$ are given by

$$\tilde{\alpha} = \tilde{\alpha}_s(1-g) + \tilde{\alpha}_L g \tag{3.32}$$

$$\tilde{k} = \tilde{k}_s(1-g) + \tilde{k}_L g \tag{3.33}$$

where $\tilde{\alpha}_s$ is the solid thermal diffusivity, $\tilde{\alpha}_L$is the liquid thermal diffusivity, $\tilde{k}_s$ is the solid thermal conductivity, and $\tilde{k}_L$ is the liquid thermal conductivity. For temperatures below $\tilde{T}_s$, $\tilde{\alpha} = \tilde{\alpha}_s$ and $\tilde{k} = \tilde{k}_s$. For temperatures above $\tilde{T}_L$, $\tilde{\alpha} = \tilde{\alpha}_L$ and $\tilde{k} = \tilde{k}_L$. $\tilde{T}_s$ and $\tilde{T}_L$ are chosen to be 1.25 below and above the eutectic temperature, respectively. This range is minimal while still ensuring numerical convergence. Figure 3.3b and c show the interpolated values of the thermal diffusivity and thermal conductivity, respectively.

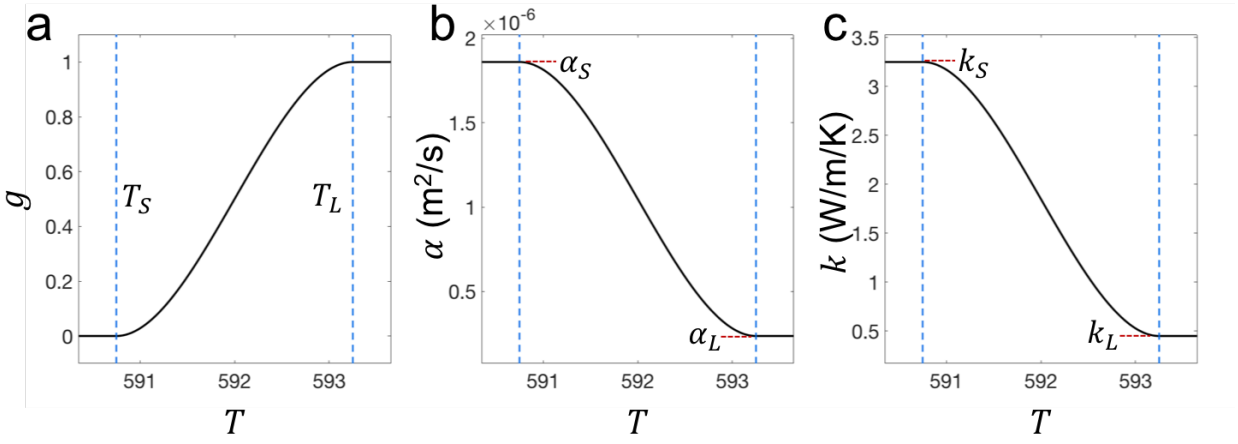

Figure 3.3 Interpolation function and interpolated materials properties: a. The interpolation function, g, is plotted over the temperature range of T_S to T_L. Outside that range, the value is displayed here as a constant extrapolation. **b.** The dimensional interpolated thermal diffusivity, α. **c.** The dimensional interpolated thermal conductivity, k.

A term is added for the latent heat rejected at the solidification front over the same temperature range as the interpolation function g. For temperatures between $\tilde{T}_s$ and $\tilde{T}_L$, Equation 3.27 becomes:

$$\frac{\partial \tilde{T}}{\partial \tilde{t}} = \tilde{\alpha}\tilde{\nabla}^2\tilde{T} + \tilde{v}\left[1 + \left(\frac{c_L}{c_s} - 1\right)g + \left(\frac{c_L}{c_s} - 1\right)\tilde{T}\frac{\partial g}{\partial \tilde{T}} + \frac{L_E}{c_s}\frac{\partial g}{\partial \tilde{T}}\right]\frac{\partial \tilde{T}}{\partial \tilde{y}} \tag{3.34}$$

where c_s and c_L are the heat capacities of the solid and liquid eutectic, respectively, and L_E is the latent heat for the eutectic mixture.

The physical constants used to parameterize the temperature profile model for AgCl-KCl are summarized in Table 3.2. The model is discretized using a centered finite-difference scheme and a forward Euler time stepping scheme. For $\partial\tilde{T}/\partial\tilde{y}$ in the velocity term, an upwinding Essentially Non-Oscillatory (ENO) scheme is utilized.[168] The dimensionless grid spacing $\Delta\tilde{x}$ and time step $\Delta\tilde{t}$ are 0.05 and 2.5×10^{-5}, respectively. The code is parallelized via domain decomposition using the message passing interface (MPI) library.

Two-dimensional simulations of a vertical slice of the central region of the filament are performed under steady-state conditions to determine the solidification front orientation in the *y*-*z* plane. Simulating in two dimensions adequately captures the behavior at the center of the filament while allowing for a large number of printing speeds to be considered without incurring a large computational cost. The solidification front orientation is calculated as the angle between the printing direction and the surface normal of the contour curve at the eutectic temperature, averaged over the thickness of the filament.

Three-dimensional simulations were carried out under steady-state conditions to determine the thermal gradients in the *y*-direction and the orientation of the solidification front in the *x*-*y* plane at the bottom surface of the filament. The solidification front orientation was calculated by finding the angle between a linear fit to the contour curve at the eutectic temperature (the solidification front) and the printing direction. The linear fit was applied to the outermost 1% of the filament width to find the solidification front orientation at the edge of the filament and the innermost 1% to one side of the center of the filament width to find the solidification front orientation at the center of the filament. The thermal gradients and solidification front orientations were then used to set up the phase-field simulation.

Table 3.2 Quantities used in parameterizing the eutectic filament heat transfer simulations.

Quantity	Symbol	Value	Reference
Thermal diffusivity of solid eutectic	α_S	1.86×10^{-6} m^2/s	169,170
Thermal diffusivity of liquid eutectic	α_L	2.36×10^{-7} m^2/s	171
Thermal conductivity of solid eutectic	k_S	3.25 W/m/K	170
Thermal conductivity of liquid eutectic	k_L	0.45 W/m/K	171
Heat capacity of solid eutectic	c_S	417 J/kg/K	169,170
Heat capacity of liquid eutectic	c_L	519 J/kg/K	171
Temperature of air	T_{air}	25°C	62
Temperature of substrate	T_{sub}	25°C	62
Temperature of nozzle	T_{nozzle}	400°C	62
Heat transfer coefficient to air	h_{air}	10 W/m^2/K	172
Heat transfer coefficient to substrate	h_{sub}	2×10^3 W/m^2/K	62
Latent heat of fusion per unit mass for eutectic	L_{E}	1.4×10^5 J/kg	173

3.3 Hindered Grain Boundary Diffusion

3.3.1 Sharp Interface Model

Grain boundaries that hinder diffusion have their greatest effect at orientations perpendicular to the diffusion direction as that configuration positions the fast and slow regions in series. Therefore, as a first step to develop a numerical model and assess its accuracy, we

consider a one-dimensional system in which grain boundaries are placed perpendicular to the diffusion direction (i.e., the grain boundary normal is parallel to the diffusion direction). The evolution of the concentration, C, in the bulk of the grains is described by the diffusion equation:

$$\frac{\partial C}{\partial t} = D_{bulk}\frac{\partial^2 C}{\partial x^2} \tag{3.35}$$

where t is time, D_{bulk} is the constant bulk diffusivity, and x is the coordinate in the diffusion direction. To account for the hindrance of diffusion at the grain boundary, a Neumann boundary condition is imposed at each grain boundary such that for an identical concentration gradient, the flux across the grain boundary is lower than the flux in the bulk, resulting in a sharper concentration gradient in grain boundaries than in the bulk at steady-state. The other physical constants needed to parameterize the model for a given system are the grain boundary diffusivity, D_{gb}, the grain boundary thickness, δ, and the grain size, d.

First, a sharp interface model for the flux boundary condition at grain boundaries will be described and used as a baseline. The flux at the grain boundary, J_{gb}, is dependent on the concentration drop across the grain boundary and is given by:

$$J_{gb} = -\frac{1}{\kappa}\Delta C_{gb} \tag{3.36}$$

where ΔC_{gb} is the concentration drop across the grain boundary. The degree of hindrance, κ, is the parameter which sets how strongly the grain boundary blocks chemical transport, and it is related to the diffusivity and thickness of the grain boundary. We choose to define the degree of hindrance as

$$\kappa = \delta\left(\frac{1}{D_{gb}} - \frac{1}{D_{bulk}}\right) \tag{3.37}$$

Much like the calculation of the electrical conductance of a series circuit, the inverse of the diffusivity is the relevant quantity. This formulation of κ is such that the degree of hindrance is

independent of δ when $D_{gb} = D_{bulk}$, a condition not held for a simpler choice such as $\kappa = \delta/D_{gb}$.

The boundary conditions at the left and right edges of the domain are Dirichlet boundary conditions of $C = 1$ and $C = 0$, respectively. The concentration evolution is calculated using Equation 3.35. This one-dimensional sharp interface model is sufficient for systems in which the grain boundaries are all perfectly perpendicular to the diffusion direction; however, a model which can allow for angled or curved grain boundaries is necessary for more complex systems.

3.3.2 Smoothed Boundary Method

As previously discussed in Section 3.1.2 for the template-directed eutectic solidification model, the Smoothed Boundary Method is a diffuse interface approach for setting internal boundary conditions using a field variable called a domain parameter.[163] For a polycrystal, we use domain parameters, ϕ_q, to describe the location of each grain in the system such that $\phi_q = 0$ outside grain q and $\phi_q = 1$ inside grain q, as in the phase-field modeling of grain growth.[174] The interface is indicated as a region of smooth transition between 0 and 1 described by a hyperbolic tangent function,

$$\phi_q = \frac{1}{2}\left(1 + \tanh\left(\frac{x - x_q}{\zeta}\right)\right) \tag{3.38}$$

where x_q is the location of the grain boundary and ζ is a numerical parameter which controls the thickness of the diffuse interface, which naturally arises as a solution to the Allen-Cahn equation.[102] The sum of all domain parameters at any given point is equal to one, $\sum_q^Q \phi_q = 1$, where Q is the number of grains in the system.

To include the effect of grain boundaries, the diffusion equation is modified to include a term that sets the Neumann boundary condition in regions where the gradient of the domain parameter is nonzero (i.e., at the grain boundaries):[163]

$$\frac{\partial C_q}{\partial t} = D_{bulk}\frac{1}{\phi_q}\frac{\partial}{\partial x}\phi_q\frac{\partial C_q}{\partial x} + \frac{1}{\phi_q}\left|\frac{\partial \phi_q}{\partial x}\right|\left[-\frac{1}{\kappa}\Delta C_{gb}\right] \tag{3.39}$$

where C_q is the concentration field for grain q. A separate concentration field must be solved for each grain to accurately capture ΔC_{gb}in Equation 3.35. This concentration drop for the diffuse interface approach is calculated by:

$$\Delta C_{gb} = C_q - \frac{\sum_{i\neq q}^{Q}\phi_i C_i}{\sum_{i\neq q}^{Q}\phi_i} \tag{3.40}$$

such that ΔC_{gb} is the difference between the concentration of the grain considered and a weighted average of the concentrations of all the other grains. The use of this weighted average term also prevents any spurious effect from the concentration field outside a grain located far from the grain under consideration.

3.3.3 Microstructure Generation

Artificial polycrystalline microstructures are generated using a procedure outlined in Ref. 47. First Dream.3D[175] is utilized to generate voxel data for a polycrystalline microstructure with the desired grain size distribution and grain aspect ratio (to introduce anisotropy to grain boundary structures as required). The voxel data consists of a three-dimensional array for each grain which has values of 1 inside the grain and 0 outside the grain. Next, a field is created for each grain which is the average of a voxel and its six nearest neighbors. This introduces regions at grain boundaries which have nonzero values for more than one grain array, a condition used to check if grains are in contact with each other. Arrays containing grains which do not contact each other are added to one another in such a way as to culminate with the fewest number of arrays to describe the structure. These multigrain arrays are then subjected to Allen-Cahn[102] smoothing to obtain diffuse interfaces in the shape of hyperbolic tangent functions that enable the use of the Smoothed Boundary Method described in Section 3.3.2.

Chapter 4: Directional Solidification of Eutectics Under Geometric Confinement

The simplest cases of template-directed eutectic solidification are those of simple geometric confinement. In this chapter, we discuss four cases of eutectic systems solidified under geometric confinement. First, we investigate the situation of eutectic solidification being confined to a printed filament. Next, solidification is confined to the surface of a three-dimensional cage structure. A transition from rod-like to lamellar structures with increasing solidification velocity is explored. Finally, an example is shown where eutectic confinement in a cylindrical geometry can produce core-shell nanowires.

4.1 Eutectic Printing

This section is largely a reproduction of part of the article titled "High Operating Temperature Direct Ink Writing of Mesoscale Eutectic Architectures" previously published in Advanced Materials in 2017.[62] All eutectic printing experiments and their related measurements

presented in this chapter were conducted by experimental collaborators William Boley and Jennifer Lewis at Harvard University.

4.1.1 Introduction and Approach

A new process for creating mesoscale eutectic architectures, known as high operating temperature direct ink writing (HOT-DIW), was developed at Harvard University by Jennifer Lewis' research group.[62] Specifically, a molten eutectic ink composed of a silver chloride (AgCl)-potassium chloride (KCl) is printed onto a glass substrate in air under ambient conditions. The ink solidifies when cooled below its eutectic temperature ($T_E \approx 319°C$).[56,57,142] By controlling the printing temperature and speed, mesoscale eutectic AgCl-KCl architectures are created that are composed of lamellar features oriented along the printing direction, whose periodic spacing can be systematically varied between ~100 nm and 2 μm. Heat transfer calculations and phase-field modeling are carried out to understand the influence of key printing parameters on their directional solidification. Given their periodicity, these mesoscale eutectic architectures serve as diffraction gratings that manipulate light in the visible and infrared regimes (optical measurements and simulations performed by William Boley and Ashish Kulkarni, respectively, can be found in Ref. 62). By selectively etching KCl lamellae followed by coating silver onto the remaining AgCl lamellae, their optical reflectivity is enhanced by an order of magnitude.

While we focused on the AgCl-KCl system due to its relatively low eutectic temperature, lamellar microstructure, and ability to print in air,[61] HOT-DIW enables patterning of nearly any material whose melting point is below 700°C, the current maximum hot operating temperature, including polymers, glasses, and metal eutectics.

The experimental HOT-DIW platform developed by the Lewis group consists of a custom-designed graphite nozzle that is locally heated to 400°C through which the molten AgCl-

KCl ink flows. The solidification front trails the hot nozzle, as the nozzle is translated across the substrate at a printing speed, v. Upon solidification of the eutectic ink, the AgCl and KCl phases self-organize into a lamellar architecture with a characteristic spacing, L, which is governed by the rates of solidification and diffusion ahead of the solidification front[57] and whose relative lamellar widths are determined by the eutectic phase volume fraction (i.e., 62% AgCl and 38% KCl).[165]

4.1.2 Simulation Method

Heat transfer calculations were conducted using the method described in Chapter 3 Section 3.2. Equation 3.34 was parameterized with the material properties found in Table 3.2 and solved to steady-state. The x-direction is parallel to the width of the filament, the y-direction is parallel to the printing direction, and the z-direction is parallel to the thickness of the filament. Two-dimensional simulations of a vertical slice within the central region of the filament were performed under steady-state conditions to determine the solidification front orientation in the *y*–*z* plane. This two-dimensional simulation adequately captured the behavior at the center of the filament while allowing for a large number of printing speeds to be explored without incurring a large computational cost. The solidification front orientation was calculated as the angle between the printing direction and the surface normal of the contour curve at the eutectic temperature, averaged over the thickness of the filament.

Three-dimensional heat transfer simulations were carried out under steady-state conditions to determine the thermal gradients in the *y*-direction and the orientation of the solidification front in the *x*–*y* plane at the bottom surface of the filament. The solidification front orientation was calculated by finding the angle between a linear fit to the contour curve at the eutectic temperature (the solidification front) and the printing direction. The linear fit was applied to the outermost 1% of the filament width to find the solidification front orientation at

the edge of the filament and the innermost 1% to one side of the center of the filament width to find the solidification front orientation at the center of the filament. The thermal gradients and solidification front orientations were then used to set up the phase field simulation.

Phase-field simulations were conducted to predict the filament morphology utilizing the method described in Chapter 3 Section 3.1. Equations 3.5 and 3.8 were solved with the parameter set shown in Table 3.1 with the exception of the eutectic composition, which was set to the actual 30% KCl rather than the volume fraction. The morphology was not significantly affected by this discrepancy because of the system's tendency to form lamellar features. The thermal gradient for simulations of the edge of the filament used a thermal gradient that was higher than that calculated by the temperature profile method (1.5×10^7 K/m) to encourage nucleation of new lamellae. A higher thermal gradient was expected because the experiment showed a curved surface in which the filament edge became thin, a feature not captured in the temperature profile model. Variables are nondimensionalized using the length scale W_p and time scale τ_p. W_p is chosen such that the ratio between the expected lamellar spacing and W_p was at least 64; τ_p was the average of the relaxation times of the AgCl and KCl phases as described in Chapter 3 Section 3.1.

For the center of the filament, $W_p = 5.0625 \times 10^{-9}$ m and $\tau_p = 3.78 \times 10^{-8}$ s. For the edge of the filament, $W_p = 1.0125 \times 10^{-8}$ m and $\tau_p = 3.03 \times 10^{-7}$ s. Greater values of W_p and τ_p were used for the edge of the filament, because the lamellar feature size was larger. The dimensionless grid spacing $\Delta\tilde{x}$ was 0.8 and the time step $\Delta\tilde{t}$ was 2.29×10^{-2} for the center and 1.15×10^{-2} for the edge. Simulations of the center of the filament used periodic boundary conditions in the *x*-direction because the isotherm was parallel with the *x*-axis; while simulations of the edge of the filament used no-flux boundaries in the *x*-direction. In both cases, no-flux boundaries were used in the *y*-direction.

An initial set of AgCl–KCl lamellae with a small periodicity of 32.4 nm (on the order of one tenth of the experimentally observed spacing) was used to allow lamellar merging so that a natural lamellar spacing evolved at steady state. The initial lamellar pairs had spacings varying randomly by 5% to break the symmetry of the initial conditions and allowed for a less constrained evolution. The initial solidification front was set to have the same orientation as the eutectic temperature isotherm.

4.1.3 Comparison of Experimental and Simulation Results

To demonstrate HOT-DIW, William Boley of Jennifer Lewis' research group produced meander line patterns composed of eutectic AgCl-KCl filaments that are nominally 2 mm wide, corresponding to the outer diameter of the nozzle used. A representative eutectic filament shown in Figure 4.1 is printed at a speed of 0.18 mm/s. The lamellar features observed on the top and bottom surfaces exhibit long-range order, persisting along the length and through the thickness of the printed filaments (Figure 4.1b). The lamellar spacing (and orientation) measured at the two edges and center region of these filaments are 668 ± 84 nm (70 ± 7°) and 324 ± 32 nm (3 ± 4°), respectively, where the printing direction is defined as 0°. These values are in good agreement with predicted values of 716 nm and 67° (edge) and 309 nm and 0° (center) determined by phase-field simulation and heat transfer calculations. Qualitatively, the agreement between experiment and simulation can clearly be seen in Figure 4.1b. Nucleation of new eutectic lamellae occurs at the edges of the filament and proceed toward the center of the filament.

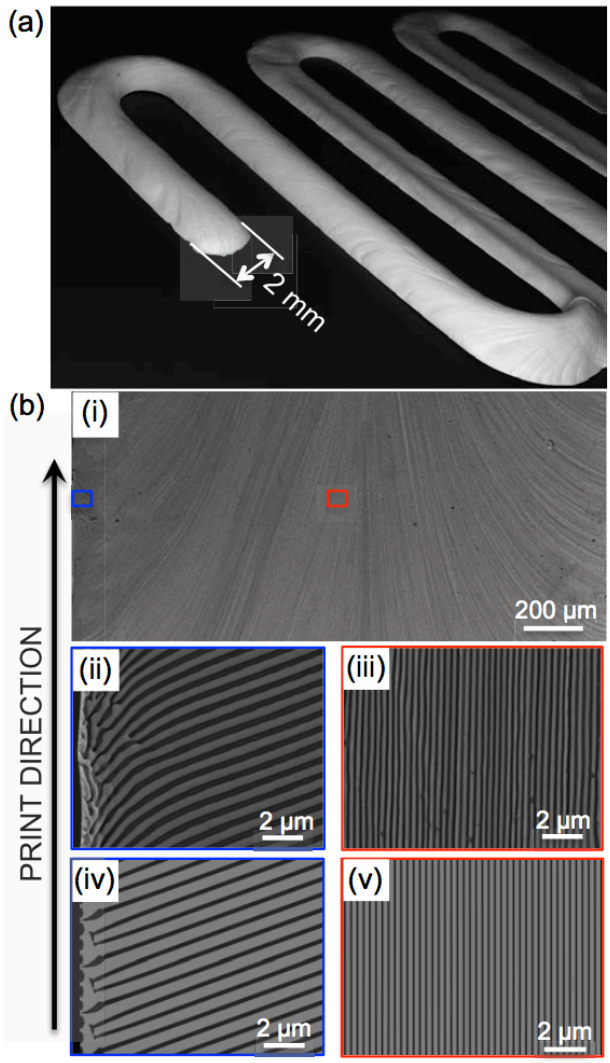

Figure 4.1 Printed eutectic AgCl-KCl filaments: (a) Macro-scale SEM image of typical printed meander pattern. **(b)** Representative images of printed filament (bottom surface), including (i) low magnification and (ii-iii) high magnification views along with (iv-v) corresponding predicted images from phase-field modeling of filament edge (blue) and center (red), respectively. The experimental data and simulations correspond to v = 0.18 mm/s. Reproduced with permission.[62] Copyright 2016, Wiley-VCH.

4.1.4 Solidification Front Dependence on Printing Velocity

The lamellar spacing within the printed eutectic architectures can be systematically controlled by varying the printing speed (Figure 4.2). In the Lewis group's experiments, at low speeds ($v \leq v_{crit}$), the printed eutectic filaments exhibited a periodic lamellar architecture, whose characteristic spacing decreases with increasing v (Figure 4.2a). However, when $v > v_{crit}$,

multiple lamellar domains are observed that progress inward from each edge ultimately impinging in the center of the filament (Figure 4.2a). A transition from a uniform to non-uniform lamellar architecture occurs at v_{crit} (≈ 1 mm/s). To better understand these experimental observations, two-dimensional heat transfer calculations were carried out to determine the influence of printing speed, v, on the shape and evolution of the solidification front within the printed filaments (Figure 4.2b). When $v \leq v_{crit}$, the temperature field remains constant throughout the thickness of the filament resulting in a vertical solidification front that gives rise to a uniform lamellar architecture (Figures 4.2b). When $v \leq v_{crit}$, the speed of the solidification front is approximately identical to v. However, this relationship falls off sharply when $v > v_{crit}$ and the temperature field becomes non-uniform throughout the thickness of the filament shifting the solidification front away from the nozzle to the filament edges (Figure 4.2b). Under these conditions, the solidification front deviates from a vertical orientation (Figure 4.2b), as the advective heat transfer rate associated with a given printing speed becomes large relative to thermal diffusion through the filament thickness. The HOT nozzle moves away from the deposited eutectic ink quickly enough such that its influence on the solidification front lessens as v increases (Figure 4.3a). This weaker dependence of the solidification front speed on v translates to a weaker dependence of L on v (Figure 4.2c).[57] Hence, above $v_{crit} \approx 1$ mm/s, the direction of solidification and, hence, lamellar growth changes from predominately parallel to the print path to primarily inward from each filament edge, while remaining vertical to the substrate. As these lamellar features converge at the filament center, domain boundaries arise leading to a non-uniform architecture (Figure 4.2a). Based on simulations, the printed filaments begin to solidify roughly 200 μm downstream from the HOT nozzle-molten ink interface (Figure 4.2b).

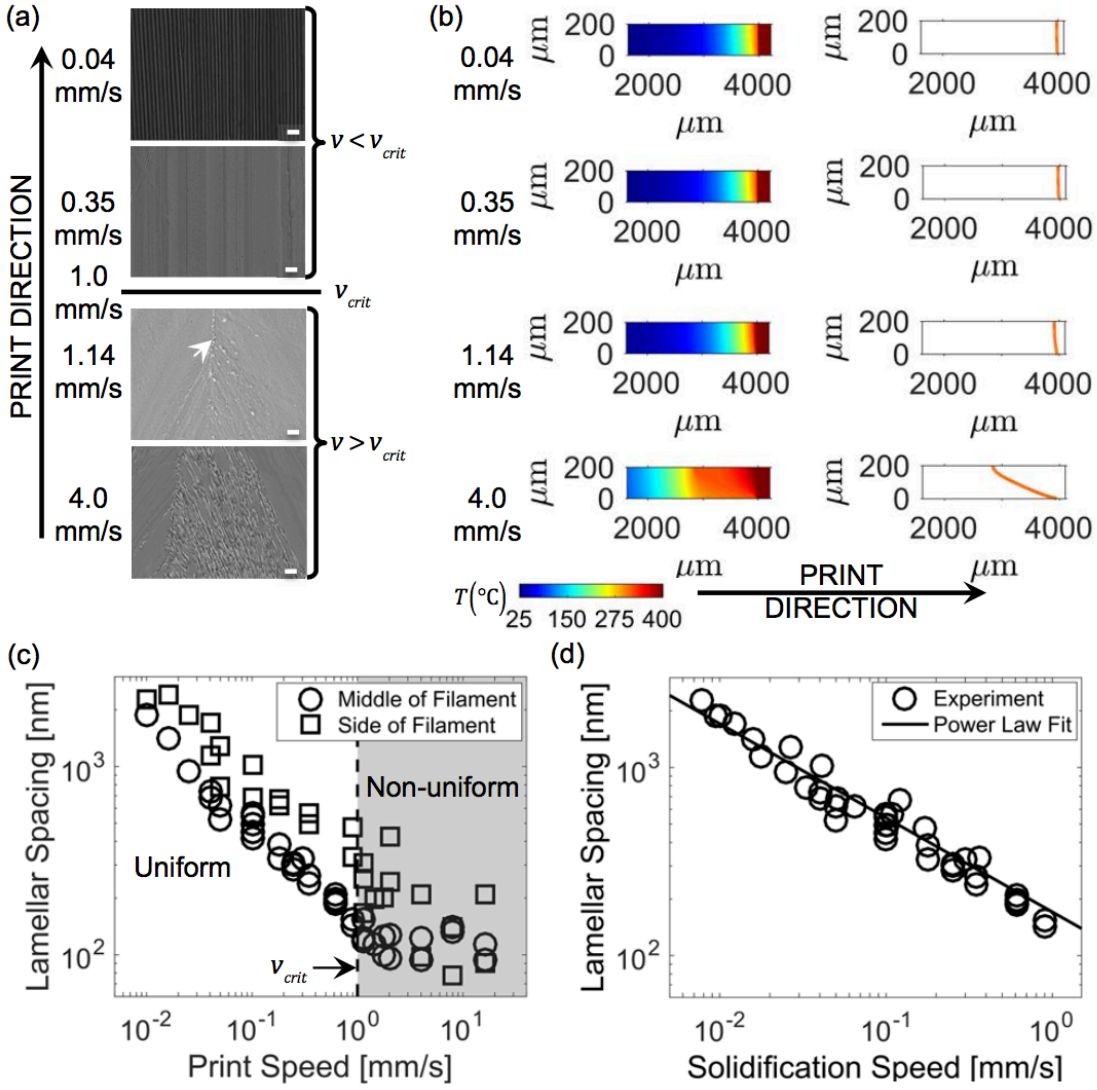

Figure 4.2 Controlling lamellar spacing in printed eutectic AgCl-KCl filaments: (a) SEM images of eutectic filaments (center region, bottom surface) printed at speeds below and above v_{crit}. [Note: Arrow shown in image at v = 1.14 mm/s denotes the formation of a domain boundary within the printed filament.] Scale bars are 2 microns. **(b)** Two-dimensional heat transfer simulations of the central region of printed filaments as a function of printing speed, which reveal the temperature fields (left column) and resulting solidification fronts (right column). The HOT nozzle interface is located at position 4214 microns in the print direction. **(c)** Lamellar spacing measured within printed filaments as a function of print speed. White region denotes filaments printed below v_{crit}, where lamellae of uniform orientation are observed. Gray region denotes filaments printed above v_{crit}, which contain lamellae that are non-uniform in orientation. **(d)** Lamellar spacing as a function of solidification velocity. Reproduced with permission.[62] Copyright 2016, Wiley-VCH.

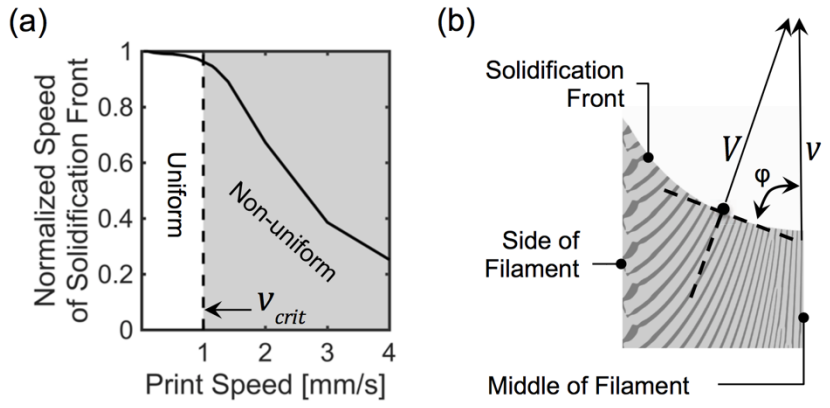

Figure 4.3 Print speed-solidification velocity relationship: (a) Normalized speed of solidification front calculated in the central region of printed filaments as a function of print speed. White region denotes filaments printed below v_{crit}, where lamellae of uniform orientation were observed. Gray region denotes filaments printed above v_{crit}, exhibiting non-uniformly oriented lamellae. **(b)** Schematic illustration of lamellar growth along bottom surface of the printed filaments depicting geometric relationship between solidification velocity (V) and printing speed (v). Reproduced with permission.[62] Copyright 2016, Wiley-VCH.

4.1.5 Eutectic Printing Conclusions

In summary, the new printing method developed by the Lewis group, HOT-DIW, is a promising technique for patterning eutectic materials for optical applications in the visible and IR regimes. By controlling the print speed, the lamellar spacing within the printed filaments can be systematically varied between approximately 100 nm to 2 μm. Heat transfer and phase-field simulations elucidated the dependence of temperature profile and microstructural evolution on printing velocity. In particular, the heat transfer simulations directed the selections of printing speeds, demonstrated an upper limit of printing speed – above which, changes in printing speed have no effect on solidification velocity and thus eutectic spacing – and revealed the nozzle's shape to be the cause of lamellar curving. Upon further optimization, this method should allow the programmable patterning of a wide range of materials, including polymers, metal eutectics, and glass, in both large area and multi-layer formats.

4.2 Three-Dimensional Cage Mesostructure Template

This section is largely a reproduction of part of the article titled "High Operating Temperature Direct Ink Writing of Mesoscale Eutectic Architectures" previously published in the Proceedings of the National Academy of Sciences of the United States of America in 2017.[144] All eutectic solidification experiments and their related measurements presented in this section were conducted by experimental collaborators Ashish Kulkarni and Paul Braun at the University of Illinois at Urbana-Champaign. The three-dimensional mesostructures utilized as templates by the Braun group were originally developed and produced by Mengdi Han, Yan Zengh, and John Rogers at Northwestern University.

4.2.1 Three-Dimensional Framework Mesostructure: Introduction

Growing interest in approaches for three-dimensional micro/nanomanufacturing derives, in part, from the potential to exploit advanced, three-dimensional designs in emergent technologies, from biomedical devices,[176-179] micro- robotics,[180-182] metamaterials[183,184] and platforms for energy storage and conversion,[185,186] to integrated electronics,[187,188] electro-mechanical components,[189] optics and optoelectronics.[190] Existing fabrication methods include nozzle- and light-based methods in three-dimensional printing,[191-194] stress-controlled bending,[195-197] colloidal self-assembly,[198,199] templated growth and others.[200-202]

In this context, routes to three-dimensional mesostructures that exploit non-linear buckling of two-dimensional precursors initiated through stress relaxation in prestrained elastomeric substrates offer some important capabilities. In particular, these methods, developed in John Rogers' research group at Northwestern University, provide access to complex, three-dimensional architectures with dimensions that can range from fractions of a micron to many centimeters,[203-210] in nearly any class of material. The result is a broad set of unique design opportunities in three-dimensional electronic, optic, optoelectronic, biomedical and robotic

systems.[144] One demonstration of these applications, explained below, is guided eutectic solidification. Specifically, we examined solidification of the eutectic AgCl-KCl confined to the surface of a three-dimensional cage consisting of ribbon-like legs.

4.2.2 Simulation Method

The temperature profile of one ribbon of the three-dimensional cage structure during solidification was calculated using COMSOL®. Dirichlet boundary conditions were applied to the top (300 K) and bottom (700 K) of the ribbon and the heat equation was solved, attaining the temperature profiles prior to equilibrium that represent the state during solidification. See Figure 4.4 for a schematic representation of the computational domain and Figure 4.5B for an image of the full cage structure. The shape of the solidification front (approximated by the eutectic temperature isocontour) was calculated to observe the effect of differing thermal conductivities in the component materials of the composite ribbon structure (Si, SiO_2, air).

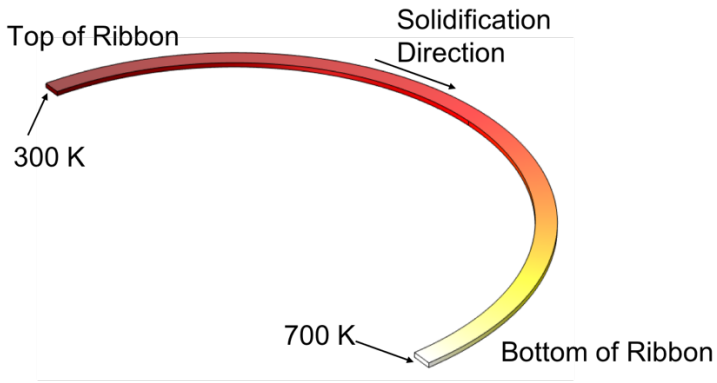

Figure 4.4 Schematic representation of the heat transfer simulation domain: A 300 K and 700 K Dirichlet boundary conditions were applied to the top and bottom of the ribbon, respectively.

Solidification of the AgCl-KCl eutectic down the ribbon structure was simulated using the template-directed eutectic solidification phase-field model described in Chapter 3 Section 3.1. Equations 3.5 and 3.8 were solved using the parameters in Table 3.1. Simulations were conducted over computational domains representing the edge of the ribbon and the center of the

ribbon, separately, with a thermal gradient of 10^6 K/m and solidification velocity of 1.93×10^{-4} m/s. The grid spacing was 5 nm and the time step was 1.3×10^{-9} s. The simulation domain had no-flux boundary conditions on all sides, except for periodic boundary conditions in the ribbon-width-direction for the center of the ribbon. The initial condition consisted of AgCl-KCl lamellae with a 400 nm spacing.

Because lamellae terminate at the edge of the ribbon as they curve outward, a mechanism must exist to stabilize the necessary increase in lamellar spacing as the number of lamellae decreases. While in some cases oscillation of the lamellar path could stabilize the increase in lamellar spacing, the continued termination of lamellae leaves that mechanism unlikely here. Therefore, new regions of the solid eutectic phases must nucleate at the solidification front.

To facilitate nucleation in the model, when the chemical potential exceeds a threshold of 4×10^{-3}, a small nucleus of the KCl phase is placed at the solid-liquid interface. Likewise, when the chemical potential falls below a threshold of -4×10^{-3}, a small nucleus of the AgCl phase is placed at the solid-liquid interface. The threshold was chosen such that new lamellae would form at a similar rate at which they terminate at the edge of the ribbon. A more detailed explanation for this threshold choice can be found in Appendix A. The nucleus is centered at the point of the largest magnitude of chemical potential where the liquid order parameter p_L is 0.25 or higher. The change in the order parameter for a nucleus is described by:

$$\Delta p_{i,nuc} = \frac{1}{4} - \frac{1}{4}\tanh\left(\frac{d-r}{2}\right) p_{j\neq i,L} \tag{4.1}$$

where d is the distance from a point to the center of the nucleus and r is the radius of the nucleus (2.5×10^{-8} m). To maintain the constraint of $p_{AgCl} + p_{KCl} + p_L = 1$, $\Delta p_{i,nuc}$ is subtracted from the order parameter of the other solid phase.

4.2.3 Three-Dimensional Frameworks as Templates for Eutectic Solidification

One example of the use of these frameworks as three-dimensional templates for material growth and processing involves geometrically guided phase separation in AgCl-KCl eutectics, of relevance partly due to the interesting optical properties that follow from controlled periodic variations in refractive index associated with this system, where length scales typically lie in the nanometer to micrometer range.[61,62] Specifically, directionally solidifying AgCl-KCl eutectic materials in three-dimensional geometries could enable optical devices and metamaterials with unique characteristics, difficult or impossible to realize using conventional fabrication schemes. In one experiment, conducted by Ashish Kulkarni in Paul Braun's research group at the University of Illinois at Urbana-Champaign, three-dimensional cages of Si-SiO_2 on quartz substrates yield controlled, AgCl-KCl submicron lamellae in three dimensions (Figure 4.5a-f) as a result of melting and solidification of AgCl-KCl powder (70 mol% AgCl and 30 mol% KCl) on top of the cage. During this process, the material flows downward along the constituent ribbons (i.e., the legs of the cage), such that cooling below the eutectic temperature (T_E = 319 °C) drives solidification and formation of periodic architectures that are strongly influenced by the three-dimensional geometry. SEM images from Braun's group in Figure 4.5c-d illustrate self-organized, periodic lamellar motifs with spacings of ~400 nm (AgCl: bright in SEM image, KCl: dark in SEM image) oriented along the ribbons. Figure 4.5e provides additional details on the eutectic structures along a single ribbon. In the center, the lamellar features exhibit long-range order and align to the tangent of the ribbon (red- squared region 1 and blue-squared region 2 in Figure 4.5e). The lamellae tend to curve outside near the edges of the ribbon (yellow-squared region 3 and green-squared region 4 of Figure 4.5e). Heat-transfer simulation results (the left frame in Figure 4.5f) explain the outward curvature of the lamellae at the edges of the structures. Specifically, the lower thermal conductivity of the SiO_2 layer (1.3 W/m/K) compared to the Si

layer (149 W/m/K) causes the solidification front to lag behind at the edges. Figure 4.6 shows the structure of the composite ribbon.

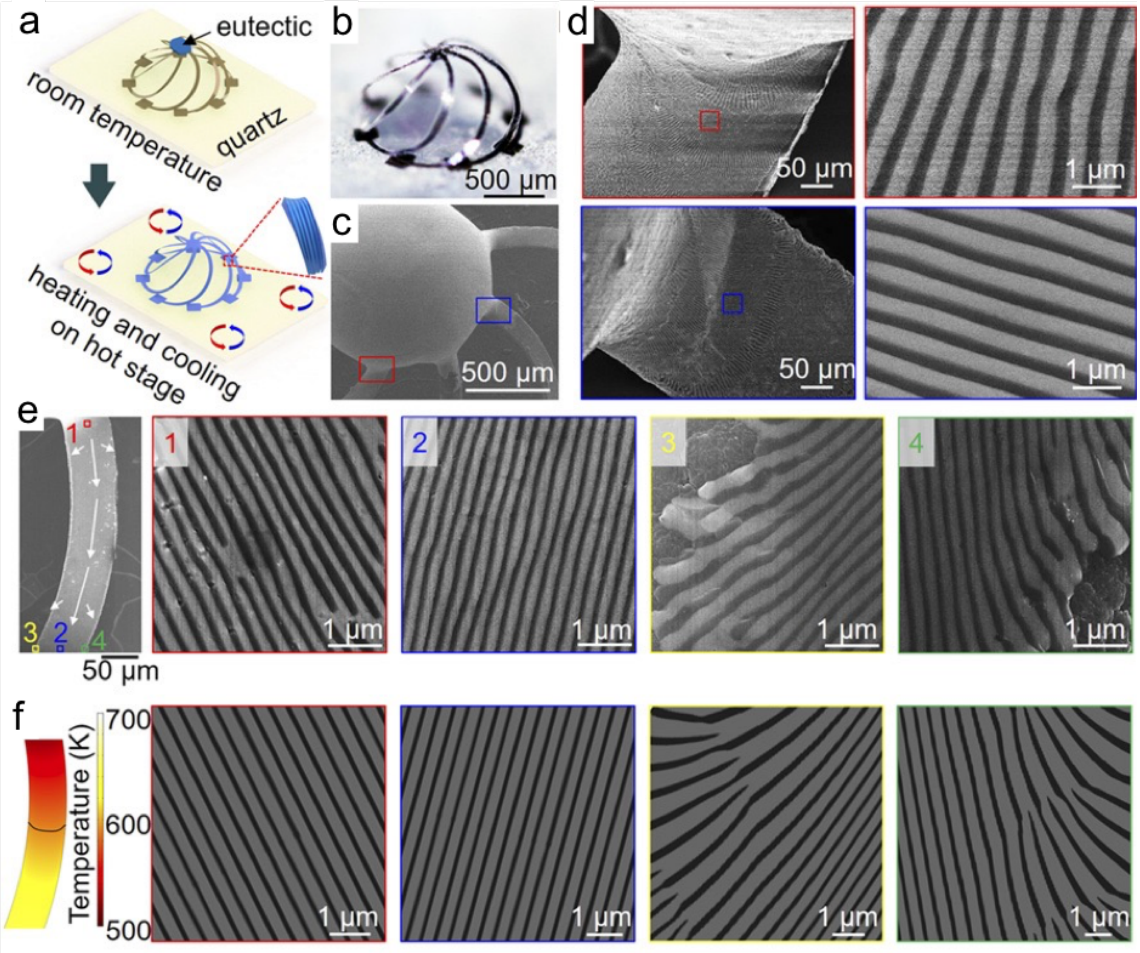

Figure 4.5 Three-dimensional mesostructures as templates for growth of functional materials at high temperatures: (a) Schematic illustration of the process of guided solidification of AgCl-KCl eutectic structures onto 3D cages of Si-SiO2 bilayers on quartz. **(b)** Optical image of a three-dimensional cage of Si-SiO2 bilayers on quartz annealed in air for 3 h at 600 °C. **(c)** and **(d)** SEM images of the cage with solidified AgCl-KCl eutectic and magnified views of periodical lamellar structures. **(e)** SEM images of a ribbon component of the cage covered with solidified eutectic material (left) and corresponding high magnification views from the top center (red), bottom center (blue), bottom left (yellow), bottom right (green) of the ribbon. **(f)** Heat-transfer and phase-field modeling of the solidification of AgCl-KCl eutectic features on one three-dimensional ribbon, including the thermal profile (left frame) and simulated AgCl–KCl structures (right four frames) that correspond to SEM images above. The dark black line in the left frame represents the solidification front. Reproduced under the terms of the CC-BY-NC-ND 4.0 license.[144]

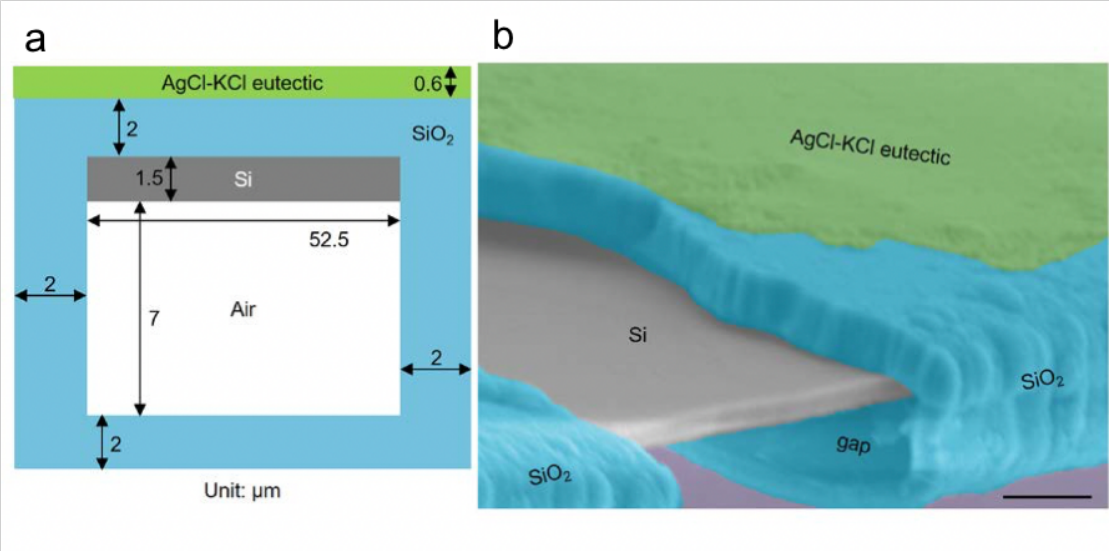

Figure 4.6 Cross-sectional views of AgCl-KCl eutectic structures on three-dimensional structures of Si-SiO2: (a) Schematic cross-sectional view of a ribbon in the three-dimensional cage after eutectic solidification. **(b)** SEM image (colorized) of the AgCl-KCl eutectics on the three-dimensional structure. The air gap forms as a result of the elimination of the epoxy material from the as-fabricated three-dimensional structures during high-temperature annealing. Scale bar, 5 μm. Reproduced under the terms of the CC-BY-NC-ND 4.0 license.[144]

Phase-field simulations utilizing the thermal profile information from the heat-transfer simulations match the experimentally observed eutectic microstructures well (Figure 4.5f), further confirming the ability of these three-dimensional structures to guide eutectic solidification. Particularly evident in the phase-field simulation results is the phenomenon of lamellae nucleating in proximity of the ribbon edge and subsequently terminating.

4.2.4 Conclusions

Utilizing a three-dimensional cage to guide the solidification of eutectic AgCl-KCl was a successful demonstration of an application for the mesostructured fabrication technique developed by the Rogers group. A difference in eutectic orientation, spacing, and morphology between the regions at the center and edges of the ribbon was observed. Heat transfer simulations revealed the origin of this phenomenon: the thermal conductivity of the ribbon was nonuniform due to its inhomogeneous structure. The higher thermal conductivity at the center of the ribbon

caused the solidification front to progress more quickly there, leading to a curved solidification front. Further, phase-field simulations utilizing temperature profiles based on the heat transfer simulation observations displayed good agreement with the experimentally obtained structures. The high level of control over eutectic microstructure, together with versatility in three-dimensional framework design, suggests unique opportunities in templated growth for optical devices and metamaterials that can operate in the visible and infrared wavelength regimes.

4.3 Rod-to-Lamellar Transition of AgCl-$CsAgCl_2$

This section is largely a reproduction of part of the article titled "Processing-Dependent Microstructure of AgCl-CsAgCl2 Eutectic Photonic Crystals" previously published in Advanced Optical Materials in 2018.[211] All eutectic solidification experiments and their related measurements presented in this section were conducted by experimental collaborators Ashish Kulkarni, Jaewon Choi, and Paul Braun at the University of Illinois at Urbana-Champaign.

4.3.1 Introduction

Self-organization techniques, such as eutectic solidification, has been shown as a possible path to forming large volumes of photonic crystals.[212-216] Among possible motifs provided by eutectic solidification, the regular microstructures of lamellar and rod eutectics have direct resemblance to one-dimensional and two-dimensional photonic crystals, respectively, where the phase-separated components provide the required contrast in the refractive index to exhibit a unique optical response.[2] The components of eutectic materials can be chosen from metals, semiconductors, polymers, organics, ceramics or salts; thus providing metal, dielectric, or even metallodielectric composites with which to synthesize (or to act as templates for) photonic crystals.[54,55,61,62,144,214,217-221] Recent examples from literature have demonstrated the formation of photonic crystals and other optically functional structures (for applications like diffraction gratings, phase-separated scintillators with light guiding and absorption induced transparency) in

directionally solidified chloride based molten salt eutectics such as AgCl-KCl,[61,62,144] NaCl-CsI,[65,221] CuI-KCl,[218] and KCl-LiF.[222]

The binary salt eutectic AgCl-$CsAgCl_2$ has the advantageous properties of a eutectic temperature (258 °C) and surface energy (135 mJ/m^2) at its eutectic temperature lower than most other eutectic salt systems, but it has received only minimal attention.[223,224] Experimental work by Jaewon Choi and Ashish Kulkarni in Paul Braun's research group at the University of Illinois at Urbana-Champaign show that when directionally solidified, AgCl-$CsAgCl_2$ has a tendency to form either a rod structure or lamellar structure depending on the directional solidification draw rates.[211] While not unprecedented, as some binary metal eutectics, e.g., Al-Al_4Ca,[225] Au-Co,[226] Cd-Sn,[227] Ni-W,[228] Ag-Cu,[229] and Al-Cu,[230] have been known to show transitions from rod to lamellar structure, to our knowledge no other salt eutectics have been shown to exhibit this property. In general, this rod-to-lamellar transition can be influenced by either volume fraction, entropy of solution of the constituent solid solution phases, interfacial boundary energy anisotropy, or the growth rate, depending on the material system.[57,124,229,231] The rod-to-lamellar microstructure transition is valuable in that it can be utilized to obtain a diversity of optical properties from a single material, using the processing conditions alone as the tuning knob. Specifically, the material can be interchangeably rendered into one-dimensional and two-dimensional photonic crystals.[2] Although the photonic properties of lamellar eutectic salts have previously been studied, i.e., as a one-dimensional photonic crystal, the optical properties of rod two-dimensional photonic crystal eutectic microstructures have not been investigated. Here, we utilize the microstructural transition of the AgCl-$CsAgCl_2$ salt eutectic system, and employ a combined experimental and simulation approach to understand the processing-dependent microstructural formation and resultant optical properties.

4.3.2 Heat Transfer Calculation Method

The temperature profiles of the eutectic during solidification were simulated in three dimensions using the commercial software COMSOL®. Neumann boundary conditions for Newton's law of cooling were applied to all air interfaces with a heat transfer coefficient of 100 W/m^2K.[232] Air temperatures for the furnace-cooled case were initially 350 °C and decreased at a rate of 4 °C /min. Air temperatures for the directional solidification case matched those measured in the tube furnace experiment with a moving frame of reference equivalent to the draw rate of 0.53 mm/s. Temperature profiles for the alumina crucible, glass slide substrate/capillary, and eutectic were calculated as a function of time by solving the heat equation and the solidification front positions were approximated by the isocontour at the eutectic temperature (531 K). The physical constants used to parameterize the heat transfer simulations were assumed to be the same as that of the AgCl-KCl eutectic system,[62] as K and Cs are Group I elements.

4.3.3 Phase-Field Simulation Method

Eutectic solidification simulations were performed using the phase-field model described in Chapter 3 Section 3.1. In particular, Equations 3.5 and 3.8 are used as the governing equations. The temperature of each point in the system is calculated based on its distance along the y-direction from the eutectic temperature isotherm plane by assuming a linear thermal gradient (G) in the x-direction (the solidification direction). The y- and z- directions are perpendicular to the solidification direction. The eutectic temperature isotherm has an initial position of x_{int} and moves in the x-direction at the solidification velocity, v. The materials properties used to parameterize the model are found in Table 4.1. The governing equations are discretized with a finite difference scheme with a grid spacing of $\Delta x=0.8$ in space and a forward Euler time-stepping scheme with a time step of Δt equal to the minimum of $0.1\Delta x^2/D$ and $0.1\Delta x^2\tau_i$ in time. This phase-field model does not account for each phase having a different

molar volume; therefore, the eutectic composition is set such that the volume fraction is preserved (C_E=68.05% AgCl). Periodic boundary conditions are imposed on all computational domain boundaries except for those perpendicular to the solidification direction, on which no-flux boundary conditions are imposed.

The initial condition for the structure of the solid layer, which serves as the seed, was either rods, lamellar, or mixed rods and lamellar (see Figure 4.7). For the rod initial condition, AgCl cylinders were placed in a $CsAgCl_2$ matrix in a hexagonal lattice arrangement. The centers of the cylinders were shifted randomly in the y- and z-directions by up to ±10% of the ideal rod spacing and the radii were adjusted by up to ±10% of the ideal rod radius given by the Jackson-Hunt theory.[57] For the lamellar initial condition, AgCl lamellae were placed in a $CsAgCl_2$ matrix with the lamellae aligned along the z-direction. The width (measured in the y-direction) of each lamellar pair is modified randomly by ±10% of the nominal lamellar spacing set by the Jackson-Hunt theory,[57] while conserving the volume. Subsequently, the local width of each AgCl layer is sinusoidally perturbed along the z-direction up to ±10% of the nominal width. The mixed initial condition is a superimposition of the rod and lamellar initial conditions with the AgCl features scaled to preserve the volume fraction.

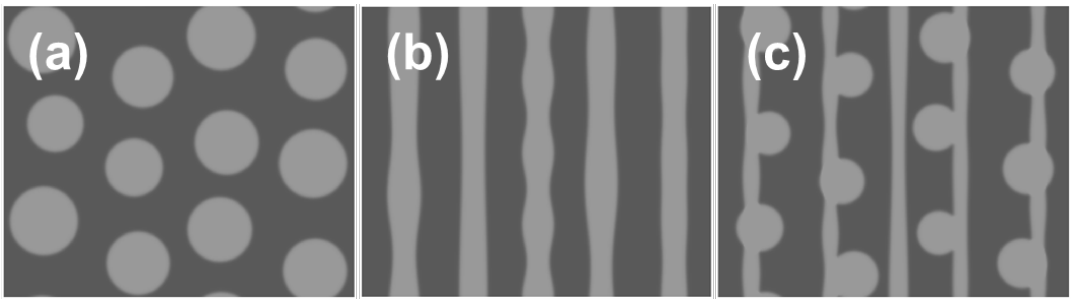

Figure 4.7 Phase-field simulation initial conditions: Cross-sections in the y-z plane (perpendicular to the solidification direction) of the initial conditions (i.e., solid seed) for the eutectic structure as assumed during the phase-field simulations. Light gray and dark gray represent AgCl and $CsAgCl_2$, respectively. **(a)** Rod initial condition. **(b)** Lamellar initial condition. **(c)** Mixed rod and lamellar initial condition. Reproduced with permission.[211] Copyright 2018, Wiley-VCH.

Table 4.1 Parameters used in the phase-field modeling, where α = $CsAgCl_2$ and β = AgCl phase.

Quantity	Symbol	Value	Reference
Liquidus slope of α	m_α	-3.33 K/mol	Calculated from [233]
Liquidus slope of β	m_β	14.25 K/mol	Calculated from [233]
Eutectic temperature	T_E	258°C	[233]
Eutectic composition	C_E	72 mol%	[233]
Composition of α at T_E	C_α	50 mol%	[233]
Volume fraction of β at T_E	V_E	36 vol.%	Calculated from [233]
Composition of β at T_E	C_β	100 mol%	[233]
α-Liquid interfacial energy	$\sigma_{\alpha-L}$	135 mJ/m^2	Assumed same as $\sigma_{\alpha-\beta}$
β-Liquid interfacial energy	$\sigma_{\beta-L}$	135 mJ/m^2	Assumed same as $\sigma_{\alpha-\beta}$
α-β interfacial energy	$\sigma_{\alpha-\beta}$	135 mJ/m^2	Extrapolated from [224]
Latent heat of fusion per unit volume for α	L_α	3.43×10^8 J/m^3	[211]
Latent heat of fusion per unit volume for β	L_β	5.13×10^8 J/m^3	173
Diffusion coefficient	D	2.53×10^{-10} m^2 /s	[234]

4.3.4 Rod-to-Lamellar Transition Observed in Experiments

This section describes the experimental works and observations performed by members of the Braun group. Specifically, they observed a rod-to-lamellar transition wherein slow solidification velocities of eutectic AgCl-$CsAgCl_2$ resulted in rod morphology and fast solidification velocities yielded a lamellar structure. The AgCl-$CsAgCl_2$ eutectic composition

consists of 72 mol% AgCl and 28 mol% CsCl and its eutectic temperature is 258 °C.[65] AgCl and CsCl powders were mixed at this composition, heated at 470 °C for 2 hours. Figure 4.8a depicts a scanning electron microscopy (SEM) image of the plan view of a bulk furnace-cooled (i.e., effective draw rate $v = 0$ mm/s) AgCl-$CsAgCl_2$ eutectic sample, showing a structure with rods in a hexagonal lattice arrangement. During furnace cooling, the samples were cooled to room temperature in the furnace (at a rate of about 4 °C/min) by turning the furnace off. The diameter of the rods, d_{AgCl}, and the rod spacing, λ, as defined in Figure 4.8a-i, were found to be approximately 750 nm and 1490 nm, respectively. Upon selectively etching the $CsAgCl_2$ matrix phase as seen in the cross-sectional view SEM image (Figure 4.8a-ii), it was discerned that the orientation of the rods was perpendicular to the substrate. Upon directional solidification of the bulk samples with a draw rate of $v = 0.2$ mm/s, the rod diameter and spacing decreased to approximately 250 nm and 440 nm, respectively. Bulk samples with rod geometry were obtained at draw rates up to $v = 0.2$ mm/s, and d_{AgCl} and λ were observed to decrease with increasing draw rates. For v of 0.27 mm/s and 0.33 mm/s circular rods were seen along with elongated rods or lamellar-like structures indicating the formation of a mixed microstructure in this range of draw rates. Increasing the draw rates to $v > 0.36$ mm/s, lamellar structures were observed in the bulk structure. We define d_{AgCl} as the width of the AgCl lamella and λ as the lamellar period (i.e., width of AgCl + width of $CsAgCl_2$); see Figure 4.8b-i. The lamellar structure was also observed for all draw rates higher than 0.36 mm/s. For $v = 0.53$ mm/s, d_{AgCl} and λ were about 115 nm and 518 nm, respectively (Figure 4.8b). The lamellae align parallel to the draw direction, as observed in the selectively etched cross-sectional view SEM image in Figure 4.8b-ii. When increasing the draw rate from $v = 0.4$ mm/s to $v = 0.63$ mm/s, the lamellar spacing is decreased from 1790 nm to 115 nm.

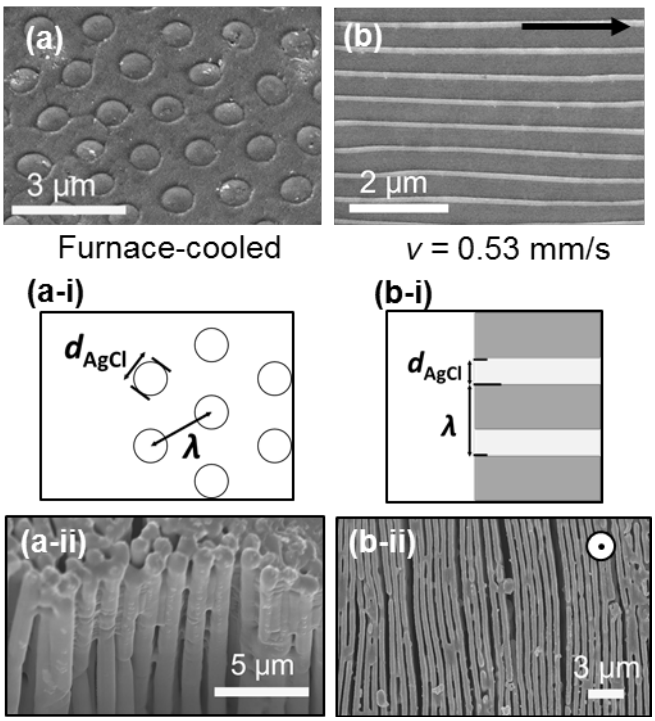

Figure 4.8 Plan view SEM images of bulk samples showing the microstructures: (a) furnace-cooled rod and **(b)** lamellae solidified with the draw rate of v = 0.53 mm/s. Arrow indicates the drawing direction. Corresponding insets show (i) the schematic defining λ and d_{AgCl} in the rod and lamellar structures and (ii) the cross-sectional view SEM images after etching-away $CsAgCl_2$. Reproduced with permission.[211] Copyright 2018, Wiley-VCH.

The low eutectic temperature and low surface energy of the AgCl-$CsAgCl_2$ eutectic system facilitate infilling of glass tubing. Using capillary action, borosilicate glass capillaries were infilled with the AgCl-$CsAgCl_2$ binary eutectic and were subsequently cooled either slowly in the furnace (that is allowed to naturally cool) or by drawing out of the furnace. The former (slow-cooled) capillaries were found to have a hexagonal arrangement of AgCl rods within a $CsAgCl_2$ matrix (Figure 4.10a). On the other hand, the capillaries solidified with a draw rate of 0.53 mm/s exhibited a lamellar microstructure consisting of alternating layers of AgCl and $CsAgCl_2$ (Figure 4.10b). Equal draw rates for both the eutectic-infilled capillaries and the bulk samples yielded similar d_{AgCl} and λ values, regardless of the resulting eutectic morphologies.

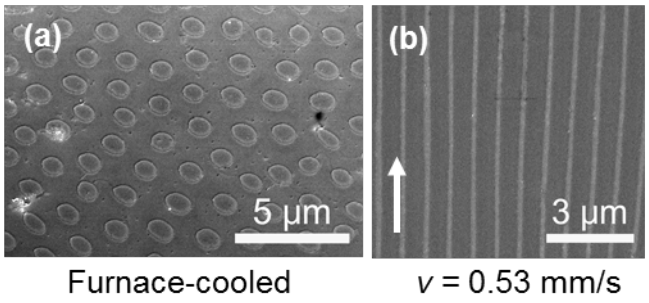

Figure 4.9 Plan view SEM images of eutectic-infilled capillary: (a) a rod structure for furnace-cooled case, and **(b)** a lamellar structure for directionally solidified case at a draw rate of 0.53 mm/s. Arrow indicates the drawing direction. Reproduced with permission.[211] Copyright 2018, Wiley-VCH.

4.3.5 Orientation and Solidification Direction

In the Braun group's experiments both the rod and lamellar structures were oriented orthogonal to the substrate, with the lamellae aligned along the draw direction. The alignment of the rods relative to the draw direction seems to be counterintuitive because the diffusion near the solidification front (i.e., the solid-liquid interface) parallel to the front is responsible for the simultaneous formation of the two solid phases. However, this alignment can be attributed to the orientation of the solidification direction not coinciding with the draw direction.[135,227] The orientation of the eutectic solidification front is determined by the details of the heat transfer in the eutectic material and the substrate for the given thermal condition, as previously demonstrated by simulations.[62,144] Heat transfer simulations were performed using COMSOL® to map the temperature profile in the eutectic material during directional solidification. For the furnace cooled case, the solidification front (approximated by the eutectic temperature isocontour) is a horizontal plane (shown in Figure 4.10a and b) and indicates a downward solidification direction. For directional solidification with a draw rate of 0.53 mm/s, the solidification front is inclined at a shallow angle to the top boundary, indicating a solidification

velocity with a smaller component in the draw direction and a larger downward component (perpendicular to the draw direction) as shown in Figure 4.10c and d.

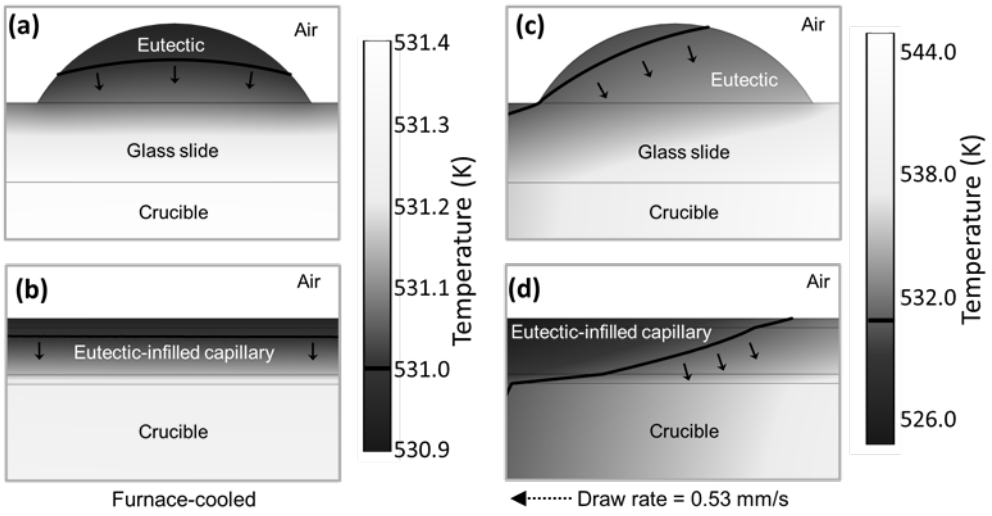

Figure 4.10 The temperature profiles of the eutectic during solidification for furnace cooling: (a) bulk case and **(b)** capillary, and for a draw rate of 0.53 mm/s **(c)** for bulk case and **(d)** capillary, respectively. Dotted arrow indicates the drawing direction. The temperature in the air is not plotted. Reproduced with permission.[211] Copyright 2018, Wiley-VCH.

4.3.6 Phase-Field Model Results and Implications

Phase-field simulations of eutectic solidification were performed with initial solid structures of rod, lamellar, and mixed configurations as a seed within eutectic liquid. For solidification velocities ranging from 0.001 mm/s to 5.3 mm/s, simulations with rods as an initial condition all yielded steady-state structures of rods in a hexagonal arrangement. For the same range of velocities, simulations with mixed or lamellar initial conditions all yielded steady-state structures of ordered lamellae. The steady-state structures are shown in Figure 4.11. The fact that the mixed state converts to the lamellar structures indicates that the lamellar structure is more stable; however, the energy barrier to switch between the rod and lamellar structures must be large enough that the rod phase does not convert to the lamellar phase. Thus, if the rod structure forms initially, then it will persist throughout the sample. Conversely, if a mixed or lamellar

structure forms initially, then the lamellar structure dominates. The apparent discrepancy with the experimental observations is attributable to the fact that in simulations, the solidification front is planar and normal to the drawing direction, whereas the solidification front orientation in the experiment is dependent on the draw rate. This will be discussed in more detail later.

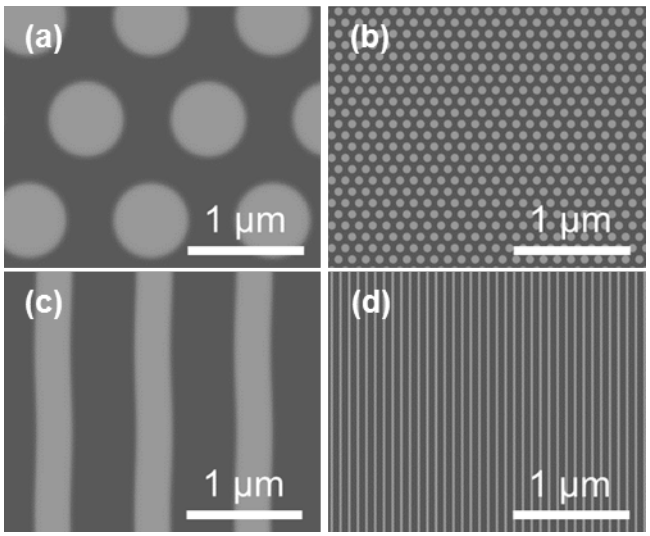

Figure 4.11 Steady-state phase-field microstructures: Phase-field simulation of directional solidification for **(a)** v = 0.01 mm/s with rod initial condition, **(b)** v = 0.53 mm/s with rod initial condition, **(c)** v = 0.01 mm/s with mixed initial condition, and **(d)** v = 5.3 mm/s with mixed initial condition. Light gray and dark gray represent AgCl and $CsAgCl_2$, respectively. Images shown consist of the computational domain repeated along periodic boundaries. Reproduced with permission.[211] Copyright 2018, Wiley-VCH.

As discussed earlier, the temperature profiles resulting from fast draw rates calculated by the heat transfer simulations show the solidification front propagating from the cooler top boundary toward the hotter bottom boundary with a small component along the draw direction. Therefore, the initial formation of the eutectic structure would likely occur at the top liquid eutectic-air interface for the bulk samples and the top liquid eutectic-glass capillary interface for the capillary samples. If a compact structure of the minority solid phase is preferred during the initial solidification at the cool boundary, a rod structure would emerge as a result and will persist through the thickness of the sample. These observations suggest that the difference in

structures seen in experiments at different draw rates is likely due to rod structures initially forming at the cool boundary at low draw rates and lamellar structures initially forming at the boundary at high draw rates. For example, in the furnace-cooled case, the initial solidification is perpendicular to the cool surface, allowing diffusion in the lateral directions that is uninhibited by the no-flux boundary of the surface. Thus, the rods and the matrix phase form simultaneously at the surface and then grow continuously downward through the sample. However, at larger draw rates, the solidification front is at an angle to the cool surface. The surface acts as a no-flux boundary where concentration gradients must be zero normal to the surface. Therefore, only one direction of diffusion is unencumbered where the solidification front and cool surface meet (i.e., the direction parallel to the planes of both the solidification front and the cool surface), leading to the formation of a lamellar structure. Further, with an angled solidification front, the rod structure could only form discontinuously, where one rod propagates along the cool surface, becomes capped by the matrix phase, and then another rod nucleates. This discontinuous growth is unlikely to occur and especially unlikely to form the hexagonally ordered patterns of rods observed in experiments.

4.3.7 Conclusion

In summary, a rod-to-lamellar microstructure transition in the AgCl-$CsAgCl_2$ eutectic system driven by the drawing rates during directional solidification was investigated through experiments and simulations. By varying the drawing rate, not only the characteristic dimensions of the microstructure, but also the lattice symmetry, can be controlled. At low solidification rates, the rod structure is present, while at higher solidification rates, the lamellar structure appears. From heat transfer and phase-field simulations, it was established that the solidified structure is strongly influenced by the structure that forms initially at the boundary of the liquid eutectic

during solidification, and thus the transition is attributed to the different structure that forms at the cool boundary.

4.4 Core-Shell Nanowire

4.4.1 Contact Angle Boundary Conditions

Here, we explore the case of directionally solidifying a single lamellar pair in a template channel.The template-directed eutectic solidification phase-field model utilized for the results presented in this section is described in Chapter 3 Section 3.1. In particular, Equations 3.19 and 3.26 are employed to govern the evolution. The template-directed eutectic solidification phase-field model is parameterized with the properties of a symmetric alloy as shown in Table 4.2. The solidification velocity which results in a lamellar spacing that matches the channel width of 50 nm is selected ($v = 9.6$ mm/s). The contact angle for the phase α-liquid-template junction, θ_α, and the contact angle for the phase β-liquid-template junction, θ_β, are varied between wetting and non-wetting conditions and the two-dimensional simulation results are displayed in Figure 4.12. As expected, low contact angles result in the solid phase preferring to be in contact with the template, and the solidification front extends farther in those cases. Conversely, high contact angles result in the solid phase preferring to avoid contact with the template and thus the solidification front lags behind in those cases.

Table 4.2 Symmetric alloy materials parameters used in the phase-field simulations.

Quantity	Symbol	Value
Liquidus slope of α	m_α	-300 K/mol
Liquidus slope of β	m_β	300 K/mol
Eutectic temperature	T_E	227°C
Eutectic composition	C_E	50 mol%

Composition of α at T_E	C_α	0 mol%
Volume fraction of β at T_E	V_E	50 vol.%
Composition of β at T_E	C_β	100 mol%
α-Liquid interfacial energy	$\sigma_{\alpha-L}$	100 mJ/m^2
β -Liquid interfacial energy	$\sigma_{\beta-L}$	100 mJ/m^2
α -KCl interfacial energy	$\sigma_{\alpha-\beta}$	100 mJ/m^2
Latent heat of fusion per unit volume for α	L_α	2.05×10^8 J/m^3
Latent heat of fusion per unit volume for β	L_β	2.05×10^8 J/m^3
Diffusion coefficient	D	1.0×10^{-9} m^2/s

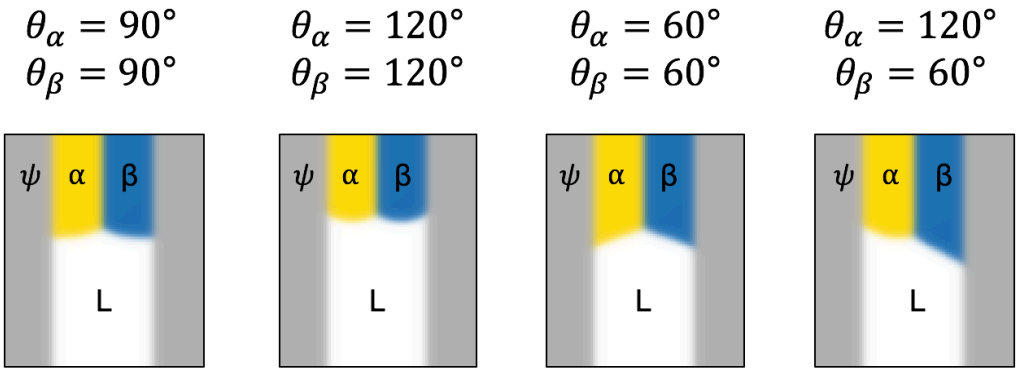

Figure 4.12 Solidification confined within a channel: Phase-field simulation results for a single lamellar pair within a narrow channel template. The contact angles for both solid phases with the liquid and template are varied. Low contact angles correspond with a preference to wet the template surface and high contact angles correspond with a preference to avoid contact with the template surface. The solidification direction is down.

4.4.2 Application to Synthesis of Core-Shell Nanowire

When extending the results from the previous two-dimensional system into a three-dimensional system, the narrow channel becomes a cylindrical channel. Two simulations are

performed: one using a cylindrical channel with a diameter of 75 nm and a second with a diameter of 125 nm. The α phase (yellow) has a contact angle of 120° and the β phase (blue) has a contact angle of 60°. All other parameters are the same as the simulations presented in Section 4.4.1. Figure 4.13 shows phase-field simulation results for the cylindrical channel structures. Because the β phase has a lower contact angle and prefers to wet the surface of the template, it migrates toward the edges of the cylinder while the α phase moves closer to the center (Figure 4.13b). Eventually, the β phase completely wets the surface of the cylindrical channel and a core-shell configuration is attained (Figure 4.13c). For the larger cylinder, a similar evolution is observed; in this case, however, the diameter of the cylinder is too large for separation into only two layers (one α and one β). The diffusion distance for two layers would be too high to maintain stability, thus a three layer structure is formed to reduce the diffusion distance and a β core is established within the α layer. The two-layer vs. three-layer distinction between the 75 and 125 nm diameter cylinders could also be achieved using a constant diameter and varying the solidification velocity instead.

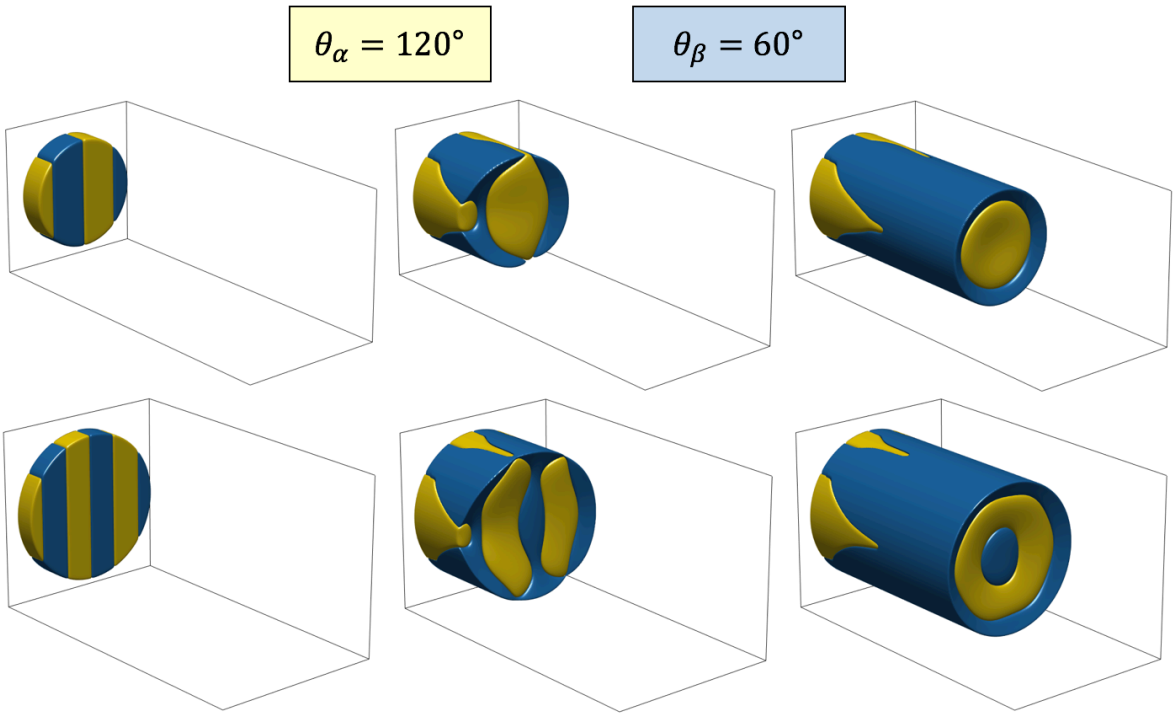

Figure 4.13 Solidification confined to a cylindrical channel: Phase-field simulation microstructures for a 75 nm diameter channel showing **(a)** the initial condition, **(b)** an intermediate structure, and **(c)** the steady-state structure and for a 125 nm diameter channel showing **(d)** the initial condition, **(e)** an intermediate structure, and **(f)** the steady-state structure with a solidification velocity of $v = 9.6$ mm/s. The yellow phase, α, has a contact angle with the template and liquid of 120° and the blue phase, β, has a contact angle with the template and liquid of 60°. The liquid and template phases are not shown for visibility.

Using this asymmetry of contact angles between the two solid phases could be useful in designing core-shell structures. If a material system and template combination were chosen such that the template phase could be selectively removed without damaging the eutectic phases, core-shell or multilayer nanowires could be synthesizes utilizing this approach.

Chapter 5: Control of Lamellar Eutectic Orientation Via Template-Directed Solidification

This chapter is largely a reproduction of the article titled "Control of Lamellar Eutectic Orientation via Template-Directed Solidification" previously published in Acta Materialia in 2019. All eutectic solidification experiments and their related measurements presented in this chapter were conducted by experimental collaborators Julia Kohanek, Ashish Kulkarni, and Paul Braun at the University of Illinois at Urbana-Champaign.

5.1 Introduction

Eutectic materials solidify upon cooling directly from a homogenous liquid into two (or more) distinct solid phases.[15,235] During this process, the solid phases organize into structures with morphologies that are controlled by a number of factors, including chemical diffusion rates, interfacial energies, bulk free energies, and thermal conductivities of the constituent materials.[15,235] The difference between the equilibrium eutectic temperature and the temperature at which the material solidifies is known as the undercooling. As discussed in Chapter 2, the

undercooling is a result of three factors: the curvature of the solidification front, the buildup of rejected solute in the liquid near the solidification front, and the energy barrier for chemical species to cross the solid-liquid interface.[57] The last of these contributions, called kinetic undercooling, is often negligibly small and disregarded. Observed eutectic microstructures are generally those that minimize undercooling, which would form before others that require a higher degree of undercooling.[57] Eutectic systems can organize into various morphologies including lamellar, rod-like, spiral, and globular structures.[229,235] The length scale of these structures can be effectively controlled in a range from tens of nanometers to hundreds of microns.[67] Eutectic systems have been found in all major classes of materials, including metals, ceramics, polymers, and small molecules. The wide variety and availability of eutectic systems as well as the diverse structures they form lend template-directed organization of eutectics applicable to syntheses of technological materials that rely on the arrangements of multiple phases with different properties.

The critical challenge of template-directed solidification is to elucidate how the template and processing condition should be designed to obtain a desired eutectic structure. The template material and geometry affect the temperature profile, which could also affect the direction of solidification and the resulting eutectic structure.[144] Surfaces (such as templates, substrates, and free surfaces) which are impenetrable by chemical species and thus impose no-flux boundary conditions, drive the orientation of the solidifying eutectic.[123,126,127,137] The chemical flux must be tangent to the no-flux boundaries, leading to the eutectic solid phases to form phase boundaries perpendicular to the surface (see Figure 5.1). In this chapter, how the boundary effects of templates, substrates, and free surfaces influence the orientation of eutectic microstructures is explored. The directional solidification of the molten salt eutectic AgCl-KCl (a model lamellar eutectic) within templates consisting of an array of pillars was undertaken by Ashish Kulkarni,

Julia Kohanek, and Paul Braun at the University of Illinois at Urbana-Champaign.[236] These experimental results are compared with phase-field model simulations. Together, the effects of pillar spacings and heights with respect to the lamellar spacing are explored and the capability to control lamellar orientation through manipulating the contribution of the boundary effects of the template is demonstrated. Understanding the pillar-template-dictated orientation of the eutectic phases is an important first step towards designing new mesostructures.

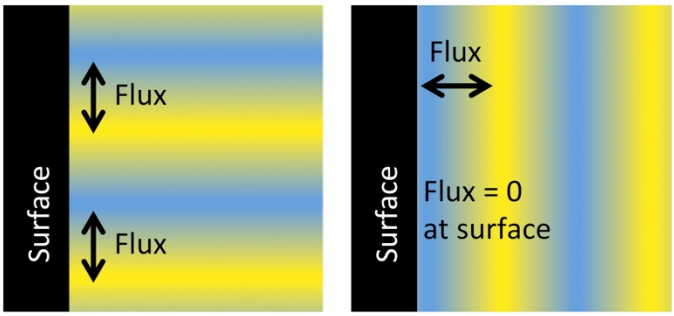

Figure 5.1 Schematic representation of the effects of a no-flux boundary on the direction of phase separation: Left: Phase boundaries forming perpendicular to the surface requires flux tangential to the surface. This is favorable since the flux is not disrupted by the surface. Right: Phase boundaries forming parallel to the surface requires non-zero flux into and out of the plane of the surface, which is not penetrable. This is unfavorable since the flux is disrupted by the surface. Reproduced with permission.[236] Copyright 2019, Elsevier.

5.2 Simulation Method

Here, the phase-field model described in Chapter 3 Section 3.2 is used for eutectic solidification simulations with Equations 3.5 and 3.19, in particular, governing the evolution. Materials parameters for AgCl-KCl are found in Table 3.1.

Unless otherwise indicated, the initial condition for the solid lamellar structure is aligned in the vertical (z) direction. The width of the computational domain in the y-direction is set to accommodate one unit cell of the template (except for the simulation shown in Figure 5.3, in which the width is two unit cells) and the z-direction is set to the same value. The x-direction size is set to be large enough to capture significant concentration gradients in the liquid, which

decrease further from the solidification front. Solidification velocities were chosen such that integer multiples of λ_{JH} fit in the domain.

The governing equations are discretized with a finite difference scheme with a grid spacing of $\Delta x = \lambda_{JH}/40$ and a forward Euler time-stepping scheme with a time step of $\Delta t = 0.1\Delta x^2/D$, which ensures numerical stability. Periodic boundary conditions are imposed on all computational domain boundaries except for those along the solidification direction, on which no-flux boundary conditions are imposed. The single exception is the simulation shown in Figure 5.3, in which no-flux boundaries are applied in the vertical direction, corresponding to the substrate and free surface.

5.3 Lamellar Reorientation Phenomenon

Directionally solidified AgCl-KCl eutectic forms a lamellar structure with a characteristic spacing of λ as defined in Figure 5.2a with the lamellae aligned parallel to the solidification direction. In the absence of a pillar template, the lamellae are oriented vertically (perpendicular to the substrate) as a result of the free surface and substrate surfaces being barriers to diffusion (no-flux boundaries) that prefer phase boundaries to form perpendicular to them. Lamellar AgCl-KCl is solidified within pillar templates. The pillar height is defined as h, diameter as d, and the smallest pillar-to-pillar edge gap as a_e as depicted in Figure 5.2b. A large range of pillar geometries was explored experimentally by the Braun group, with heights in the range of 400 nm to 6 μm and edge gaps in the range of 500 nm to 20 μm. The AgCl-KCl salt eutectic was directionally solidified within these pillar templates, such that the direction of solidification was perpendicular to the axis of the pillars (as shown in Figure 5.2c and 5.2d). The lamellar spacing λ was measured outside of the pillar template region, and the morphology of the lamellae between the pillars was discerned by cross-sectional analysis. Depending on template geometry, different lamellar orientations are observed between the pillars; either horizontal (denoted as $\lambda^{=}$)

as shown in Figure 5.2c, vertical (denoted as $\lambda^{\parallel}$) as shown in Figure 5.2d, or a mixed state (denoted as $\lambda^{\parallel=}$).

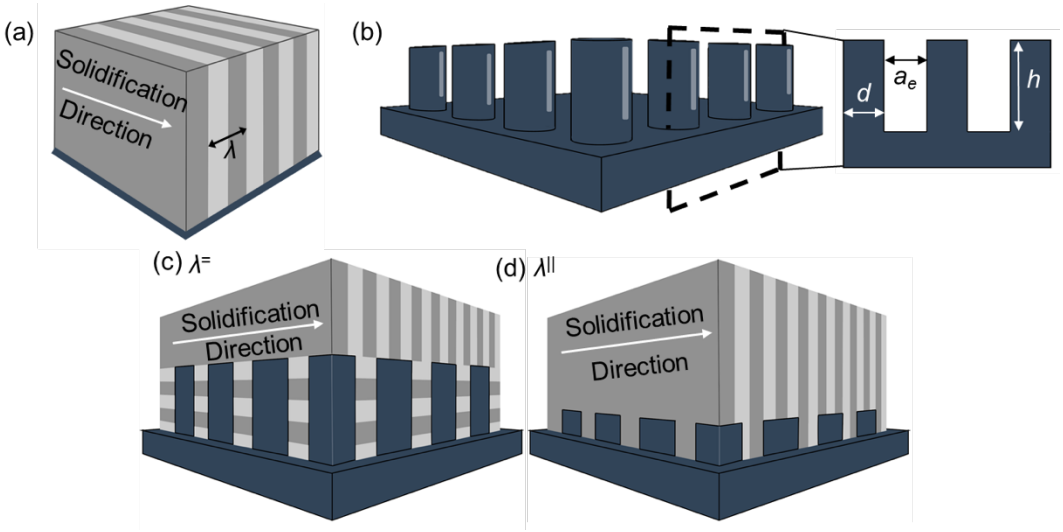

Figure 5.2 Lamellar reorientation schematic: (a) In the absence of a template, the lamellae orient vertically to the substrate and parallel to the solidification direction. The lamellar spacing is defined by λ. **(b)** Pillar template geometry: pillar height is defined as h, diameter as d, and the smallest pillar-to-pillar edge gap as a_e. **(c)** Horizontal alignment of eutectic phases (denoted as $\lambda^{=}$) within the pillar template, and **(d)** Vertical alignment of eutectic phases (denoted as $\lambda^{\parallel}$) within the pillars. Reproduced with permission.[236] Copyright 2019, Elsevier.

When the solidification front of the vertically oriented lamellae enters the pillar template, it is observed, both in experiments and simulations, that the lamellae between the pillars change orientation by 90° to align horizontally as shown in Figure 5.3. Above the pillar template, the lamellae remain vertically aligned. FIB-milled cross sections from the sample were imaged and compared to the phase-field model simulations at the corresponding locations with reliable agreement.

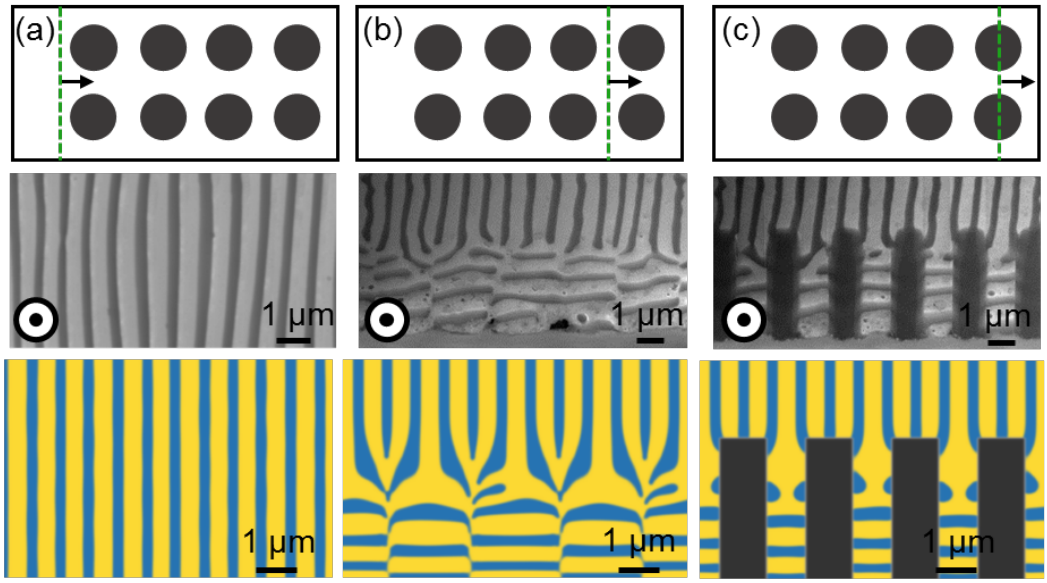

Figure 5.3 Change of lamellar orientation within pillars: Phase-field simulation results (bottom row) and cross-sectional images (middle row) at the corresponding locations indicated by the green dotted line in the top row, showing the change of lamellar orientation from **(a)** vertical outside the pillar region, to horizontal **(b)** between rows of pillars and **(c)** at the pillars. Simulation images consist of the computational domain repeated once along the y-direction periodic boundary. Black arrows and ⊙ indicate the direction of solidification. Reproduced with permission.[236] Copyright 2019, Elsevier.

5.4 Undercooling-Orientation Relationship

The undercooling was calculated from phase-field simulations at the location of the solidification front that had progressed the furthest. This value oscillates (see Figure 5.4) as the material solidifies through the template due to its periodic nature and the reported steady-state undercooling values were the maximums of these oscillations. To compare the steady-state undercooling for different orientations, multiple types of simulations were performed. First, steady-state structures and undercooling values were calculated using three-dimensional (3D) simulations with no template and compared to the analytically predicted undercooling from the Jackson-Hunt Theory.[57] Next, three-dimensional simulations were used to investigate the horizontal orientation as the evolution of the structure led to horizontal lamellae at steady-state. Because a vertical orientation was not stable as a steady-state structure in a three-dimensional

simulation, another approach was required to calculate the undercooling of the vertical case. In two-dimensional (2D) simulations, the z-direction is constrained such that all values are constant in that direction. Thus, all lamellar features are vertically aligned because that condition is enforced in two-dimensional simulations.

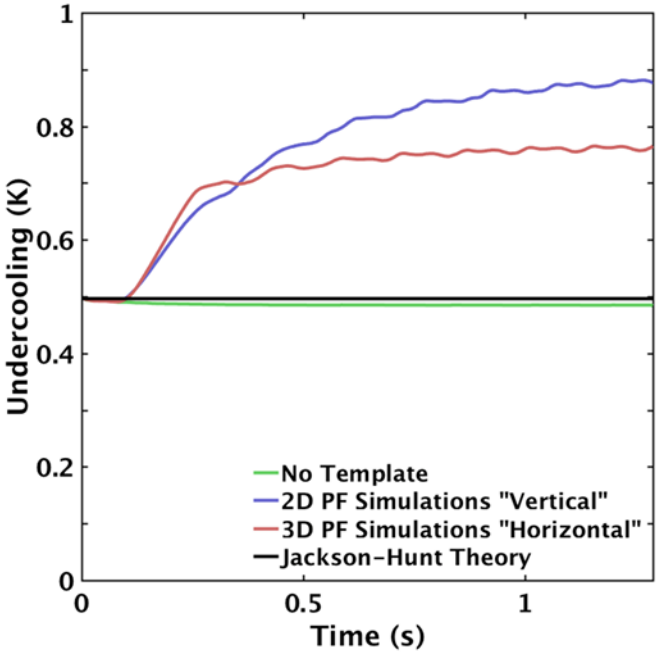

Figure 5.4 Undercooling evolution: Phase-field simulation calculated undercooling values for AgCl-KCl eutectic solidifying at v = 17.5 μm/s with different orientations. Reproduced with permission.[236] Copyright 2019, Elsevier.

For a specific solidification velocity, the eutectic prefers the optimal microstructure and spacing that achieve a minimum undercooling state.[57] Deviation from this optimal lamellar spacing increases the undercooling. We note that when the eutectic lamellae solidify without a template, the undercooling follows the theoretical minimum undercooling condition (Figure 5.5).

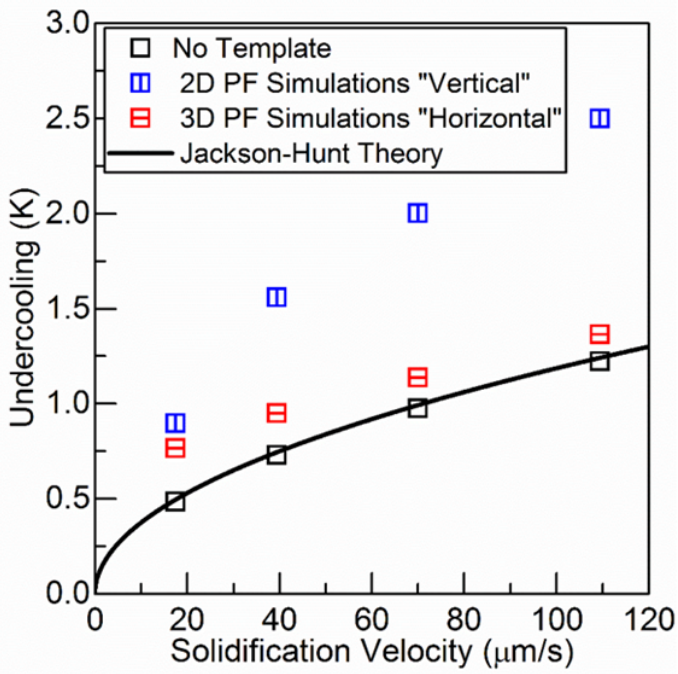

Figure 5.5 Undercooling observed in phase-field (PF) simulations: Undercooling values for the different conditions of solidification obtained by the phase-field simulations. The undercooling values for the no-template case matches with the Jackson-Hunt solidification theory.[57] In the case of solidification within the pillar template, the undercooling values of the vertical orientation are higher than the case of horizontal orientation. Reproduced with permission.[236] Copyright 2019, Elsevier.

Whereas, when the vertically aligned lamellae enter the pillar template, the solidification front is disrupted by the pillars forcing the lamellae to either terminate, increasing the lamellar spacing, or become narrower to fit between the pillars, decreasing the lamellar spacing. Alternatively, the lamellae could change their orientation to horizontal to preserve the optimal lamellar spacing. While this also necessitates an increased undercooling due to the disruption of the diffusion path imposed by the pillars, the undercooling is still less than that of the vertical alignment (as shown in Figure 5.5). Moreover, if horizontally oriented lamellae were to solidify into a pillar template, they would not change their orientation (see Figure 5.6).

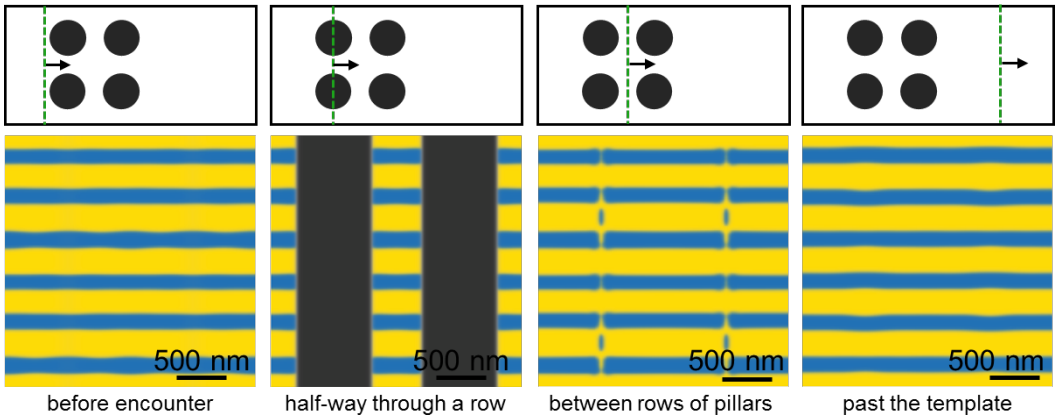

Figure 5.6 Phase-field simulation for horizontal orientation: Phase-field simulation results (bottom row) at the corresponding locations indicated by the green dotted line in the top row. The structures indicate that the lamellae remain horizontal as they solidify within the arrays of pillars if they enter the pillar template in the horizontal orientation. Simulation images consist of the computational domain repeated once along y- and z-direction periodic boundaries. All scale bars are 500 nm. Black arrows indicate the direction of solidification. Reproduced with permission.[236] Copyright 2019, Elsevier.

5.5 Conclusion

Experiments and simulations were used to quantitatively investigate the effects of templates on organization of a model lamellar AgCl-KCl eutectic. As the lamellae solidify within arrays of pillars, they are forced to modify their spacing, thus increasing the undercooling required for solidification. The undercooling calculated from phase-field simulations demonstrated that the horizontal alignment undercooling is lower than that of the vertical alignment. Therefore, lamellae will change their orientation to be horizontally aligned (perpendicular to the pillar axis), thus minimizing undercooling. Phase-field simulations reproduced this reorientation behavior, and the resultant structures agreed well with those observed in solidification experiments. Further, the phase-field model demonstrated that reorientation only occurs if the initial orientation has higher undercooling; thus, initially horizontal lamellae, which has low undercooling, will remain horizontal through the template. Additionally, by changing the relative contributions of the boundary effects of the substrate and

free surface with respect to the boundary effects of the template, other lamellar orientations can be obtained. The knowledge gained through this investigation can be used to guide the design of templates for the directional solidification of eutectics to expand the palette of microstructures emerging from template-directed organization of eutectic systems.

Chapter 6: Emergence of Highly Ordered Patterns in Template-Directed Eutectic Solidification

All eutectic solidification experiments and their related measurements presented in this chapter were conducted by experimental collaborators Ashish Kulkarni and Paul Braun at the University of Illinois at Urbana-Champaign.

6.1 Introduction

Decades of research on solidification of eutectics have indicated that both the direction and rate of heat removal play a critical role in the resultant eutectic structure.[15,57,211,237] While most investigations of eutectic solidification have been in the bulk, the study of the effect of a guiding template on eutectic solidification is only in its infancy.[1] Based on the first set of studies, the physical properties and confining effects of a template on a solidifying eutectic are showing promise for driving the emergence of new and complex eutectic mesostructures[61,138,144,236] that would be difficult or impossible to generate by other routes.

Here, we explored the case where the lamellar eutectic AgCl-KCl was solidified through a template consisting of a hexagonal lattice of pillars in a direction parallel to the pillar axis.

6.2 Simulation Method

6.2.1 Template-Directed Eutectic Solidification

Simulations for template-directed eutectic solidification were conducted using the method described in Chapter 3 Section 3.2; using Equations 3.5 and 3.19 to govern the evolution. AgCl-KCl materials parameters are found in Table 3.1. Simulations were performed over computational domains representing a unit cell of the hexagonal lattice of pillars with dimensions of 780 nm and 1352 nm and an edge gap, g, of 220 nm. Periodic boundary conditions were assumed at the unit-cell boundaries. The initial lamellar spacings were chosen such that their integer multiples (1 to 7) would fit in the 1352 nm domain width, and the solidification velocities were set such that they would result in these lamellar spacings in the absence of a template. These initial lamellae act as a solid seed in the simulations. A linear thermal gradient of 10^5 K/m was applied in the solidification direction. This thermal gradient is likely larger than that found in the physical system, but it allowed the simulation to reach a steady-state structure more quickly without affecting the final morphology. The solidification of the eutectic was simulated along the axis of the pillars until a stable, steady-state structure was attained.

6.2.2 Heat Transfer Calculation

The temperature profile in the eutectic during solidification was calculated using COMSOL (https://www.comsol.com/). In the case of pillar templates, the thermal conductivity, κ, of the infilled layer (6 μm thick, κ = 23.4 W/mK) was weighted by the volume fractions of the Ni pillar material and AgCl-KCl. The substrate was assumed as glass (0.7 mm thick, κ = 1.4 W/mK) and an overlayer of eutectic (a truncated hemispherical drop of diameter 5 mm and height 2 mm, κ = 3.3 W/mK) was placed on top of the pillar-eutectic composite. The material

parameters for AgCl-KCl eutectic were taken from Ref. 62. The cooling rate is enforced on the bottom surface of an aluminum plate (i.e., the cooling stage). Newton's law of cooling is applied to all other surfaces with an air temperature of 300 K. The shape of the solidification front (approximated by the eutectic temperature isocontour at 591.73 K) at a set cooling rate of 10 °C/min was calculated over time by solving the heat equation.

6.3 Emerging Patterns

With the well-studied AgCl-KCl eutectic,[61,62,144,236,238] an examination was undertaken to ascertain how a template impacts what would otherwise be a regular lamellar microstructure (see Figure 6.1a). Solidification experiments were performed by Ashish Kulkarni from Paul Braun's research group at the University of Illinois at Urbana-Champaign. The templates utilized in these experiments consisted of 4 to 6 μm tall pillars that are 500 to 620 nm in diameter, and arranged in a hexagonal lattice (see Figure 6.1b), with edge gaps, g (defined in the inset of Figure 6.1b), of 160 to 290 nm. Pillar diameters and g were selected to be comparable to the accessible range of the average lamellar spacing, λ (defined in the inset of Figure 6.1a), in the AgCl-KCl lamellar eutectic. Outside the template, as expected, λ was a function of the solidification rate. Inside the pillar template, there was a remarkable transition, and a broad array of solidification rate-dependent complex mesostructures appear. When λ was commensurate with the periodicity of the template, the pillars modify the phase-separation of the eutectic such that spoke-like patterns in AgCl and KCl were realized instead of the regular lamellar structure. The resultant structures were designated as trefoil (see Figure 6.1c), quatrefoil (see Figure 6.1e), cinquefoil (see Figure 6.1f), and hexafoil (see Figure 6.1g), based on the number of KCl spokes per unit cell of the template. Remarkably, the trefoil pattern resembles the Archimedean honeycomb lattice (see schematic in Figure 6.1d) of roughly hexagonally shaped AgCl and KCl domains. Whereas the

hexafoil pattern resembles the Archimedean square (KCl)-hexagonal (pillars)-dodecagonal (AgCl) lattice (defined as the SHD lattice, see schematic in Figure 6.1h).

Molten AgCl-KCl eutectic was infilled in the pillar templates and directionally solidified at various rates by the Braun group, leading to different g/λ (λ determined outside the template region). When $g/\lambda \leq 0.25$, a disordered pattern persisted. Upon increasing the solidification rate such that $0.4 < g/\lambda < 0.75$, trefoil patterns were formed. In the transition region when $g/\lambda \sim 0.3$, a mixed, predominantly trefoil, structure was present. For $g/\lambda \sim 0.95$, quatrefoil patterns dominated. When $g/\lambda \sim 1$, the cinquefoil pattern appeared, and for $g/\lambda \geq 1.05$, the hexafoil pattern was obtained. The cross-sectional view of these patterns shows a tilted alignment of the eutectic phase boundaries (see Figure 6.2a), which resulted from the slanted solidification front in the bulk of the template (see Figure 6.2b) due to the mismatch between the thermal conductivities of the Ni pillars and the AgCl-KCl eutectic.

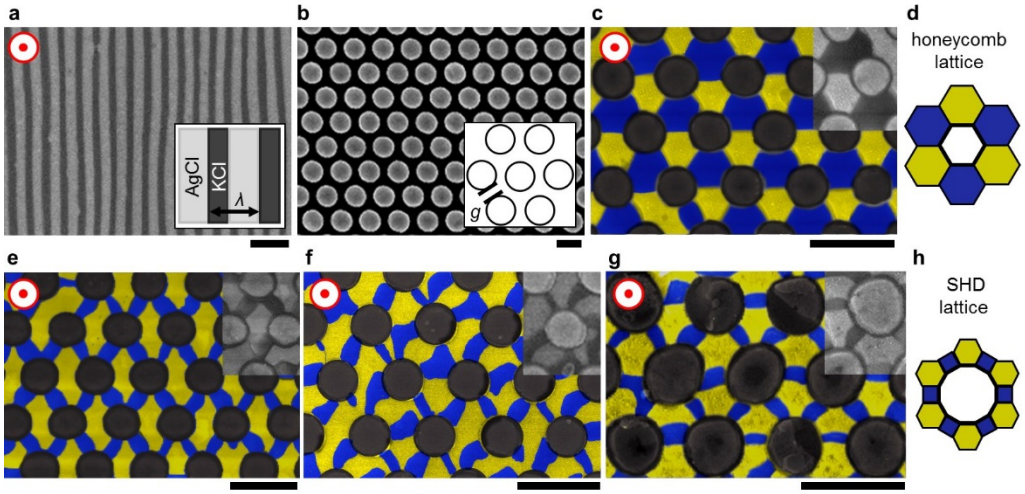

Figure 6.1 Selected microstructures formed by template-directed eutectic solidification: (a) SEM image of AgCl (bright) – KCl (dark) eutectic solidified at a cooling rate of 22 °C/min. λ as defined in the inset is 420 nm. The solidification direction is generally out of the image (z-axis), as indicated by the red ⊙. **(b)** Plan view SEM image of a pillar template sample showing the hexagonal arrangement of pillars. g = 220 nm as defined in the inset. SEM images of **(c)** trefoil, **(e)** quatrefoil, **(f)** cinquefoil, and **(g)** hexafoil patterns with 3, 4, 5, and 6 KCl spokes per unit cell of the template, respectively, obtained by varying the solidification conditions. **(d)** Schematic of the Archimedean honeycomb lattice. **(h)** Schematic of the Archimedean SHD lattice. Parts of the SEM images (in c and e-g) are false-colored with AgCl as yellow, KCl as blue, and Ni pillars as black. All scale bars are 1 μm.

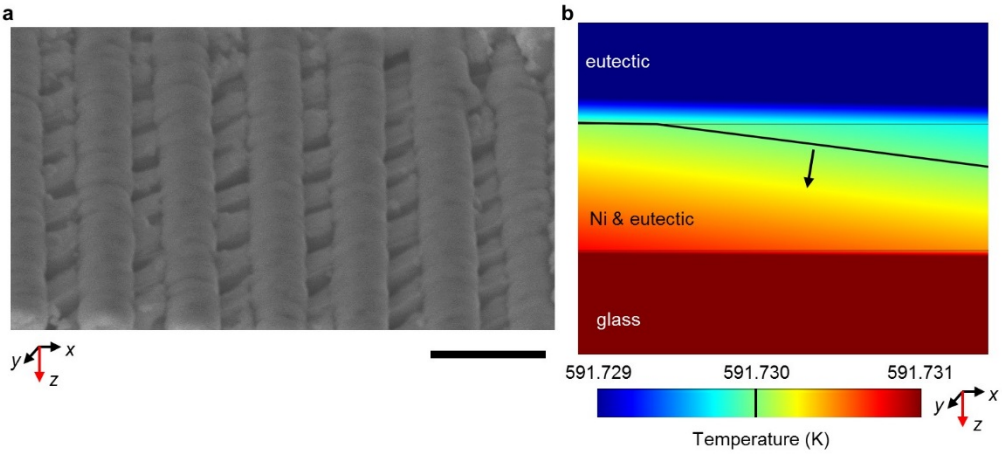

Figure 6.2 Eutectic phase boundary alignment and thermal profile in the bulk of the pillar template: (a) A cross-sectional view SEM image showing a tilted alignment of eutectic phase boundaries within the pillars. **(b)** Calculated thermal profile in the bulk of the template during directional solidification of eutectic-infiltrated Ni pillar template at a set cooling rate of 10 °C/min. The isothermal solidification front at the eutectic temperature (591.73 K) is denoted by a black line. Black arrow denotes the direction of solidification. Scale bar is 1 μm.

In phase-field simulations, when $g/\lambda = 0.163$, λ was significantly larger than the periodicity of the template and the template did not impose order on the eutectic pattern, resulting in a disordered structure (see Figure 6.3c and 6.3j). For increased solidification rates, the simulations predicted the trefoil pattern for $0.325 \leq g/\lambda \leq 0.651$ (see Figure 6.3d-6.3f and 6.3k-6.3m), cinquefoil pattern for $g/\lambda = 0.814$ (see Figure 6.3g and 6.3n), and hexafoil pattern for $g/\lambda \geq 0.976$ (see Figure 6.3h, 6.3i, 6.3o and 6.3p). Note, phase-field simulations results suggest that it is necessary to have the solidification direction parallel to the template pillar axis (i.e., along the z-axis; see Figure 6.3a and 6.3b) for these highly ordered patterns to emerge. These results reveal that at the solidification front within the template, the pillars disrupt the natural edgewise diffusion of the lamellar eutectic by compelling the diffusion fields to obey constraints set by the template geometry. To maintain the requirement of consistent diffusion path lengths[57] within this modified diffusion field, the eutectic solidifies in spoke-like patterns while preserving the overall hexagonal symmetry imposed by the template. The patterns observed for various g/λ

in experiments and phase-field simulations are mapped in Figure 6.4. This map suggests that certain ranges of lamellar spacings and template periodicities will result in a single type of spoke-like pattern, a useful finding for setting the parameters to achieve a specific mesostructure. While some experimentally observed patterns were not observed in the simulations, this is likely due to enforcement of periodic boundary conditions and use of a domain size of one template unit cell, which constrained the system and prevented the emergence of asymmetric patterns or patterns with larger periodicities.

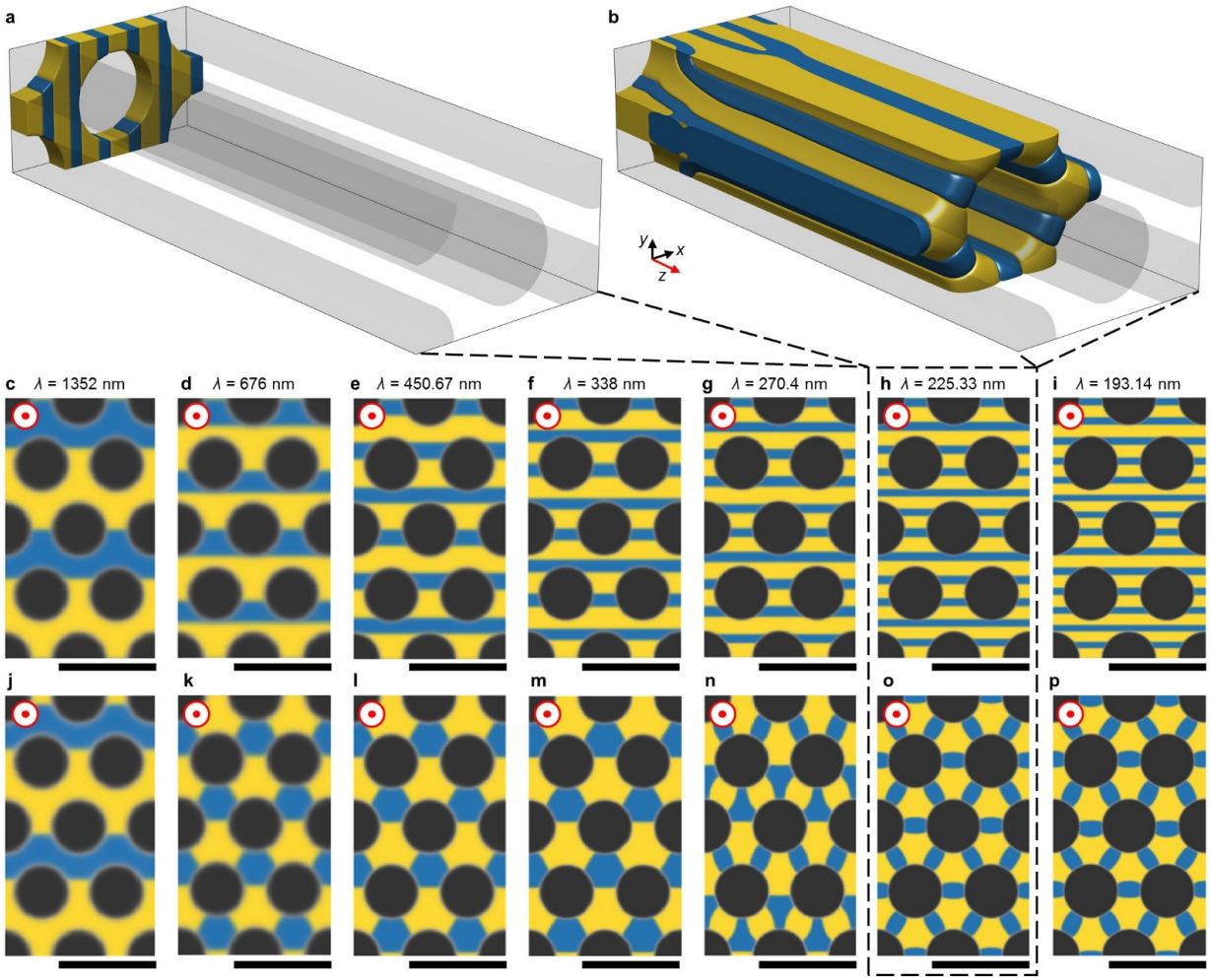

Figure 6.3 Patterns observed in phase-field simulations: A three-dimensional view of the phase-field simulation domain showing the evolution of **(a)** the initial lamellar seed (cross-section is shown in h) into **(b)** the hexafoil structure (cross-section is shown in o). The solidification direction in a & b is along the z-axis. Middle row **(c-i)**: images of the initial conditions of simulations performed using the given lamellar spacing. Bottom row images show the corresponding steady-state patterns: **(j)** disordered, **(k-m)** trefoil, **(n)** cinquefoil, **(o) & (p)** hexafoil. The solidification direction in c-p is out of the image (z-axis), as indicated by the red ⊙. The images in c-p show the x-y plane cross-section of the simulation domain repeated once in each direction. The template pillars are displayed as semitransparent gray in a & b or black in c-p, while AgCl as yellow, and KCl as blue. All scale bars are 1 μm.

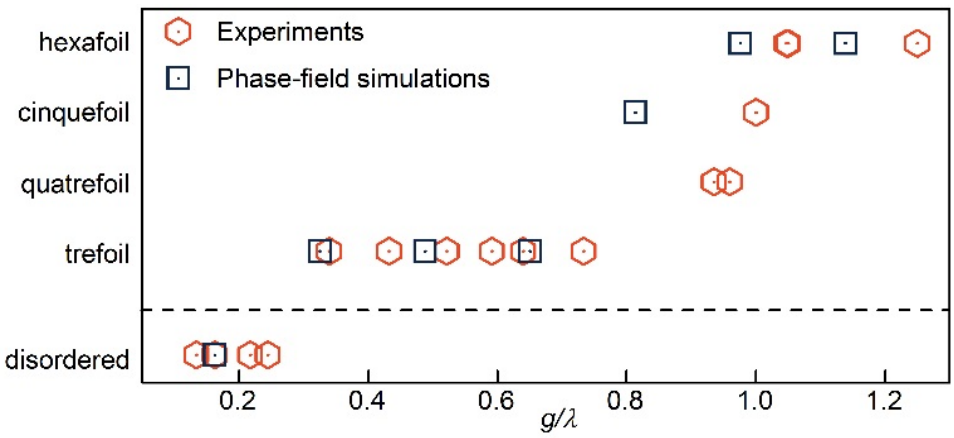

Figure 6.4 Mesostructure phase map. Map of experimentally observed and phase-field simulated patterns as a function of g/λ.

6.4 A Vast Parameter Space

The parameter space available in the template-directed eutectic solidification approach is considerable. There are many eutectic material systems available with which to vary materials constants (e.g. solid phase fraction, diffusivity, interfacial energies, etc.). There are countless template geometries accessible. Even when considering relatively simple subsets, such as lattices of pillar obstacles, there are still an extensive number of variables to select (e.g. pillar diameter, pillar spacing, lattice type, etc.) Finally, there are processing condition variables for eutectic solidification (e.g. solidification velocity, solidification direction, thermal gradient, etc.). All of these choices result in an immense parameter space for which experimental exploration alone is impractical. The phase-field model's predictions thus become particularly useful when trying to narrow that parameter space when considering the design of eutectic-template-process combinations.

To elucidate the model's utility, a parameter sweep through one variable from each of the three categories (eutectic materials constant, template geometry parameter, and processing variable) was undertaken. The parameters selected were eutectic minority phase volume fraction, V_β, pillar diameter, and solidification velocity, v. These three variables are impactful for

adjusting the mesostructure as well as demonstrating interdependence (e.g., the same effect on the microstructure can be realized by changing either solidification velocity or pillar diameter). The remaining parameters were held constant throughout the study. The materials constants were otherwise those of the AgCl-KCl system. The template consisted of pillars arranged in a hexagonal lattice with a center-to-center distance of 780 nm. Adjusting the pillar diameter while keeping the spacing and lattice constant is equivalent to changing the volume fraction of the template phase, V_ψ. The thermal gradient used was 10^5 K/m with the solidification direction along the pillar axis.

6.4.1 Hexagonal Lattice Pattern Mapping

Figure 6.5 displays the patterns that result from probing the parameter space by varying minority phase volume fraction, template phase volume fraction, and solidification velocity. Table 6.1 categories the resulting structures by the number of KCl "spokes" connected to each pillar. The 4/5-spoke label indicates that half of the pillars have four spokes and half of them have five spokes

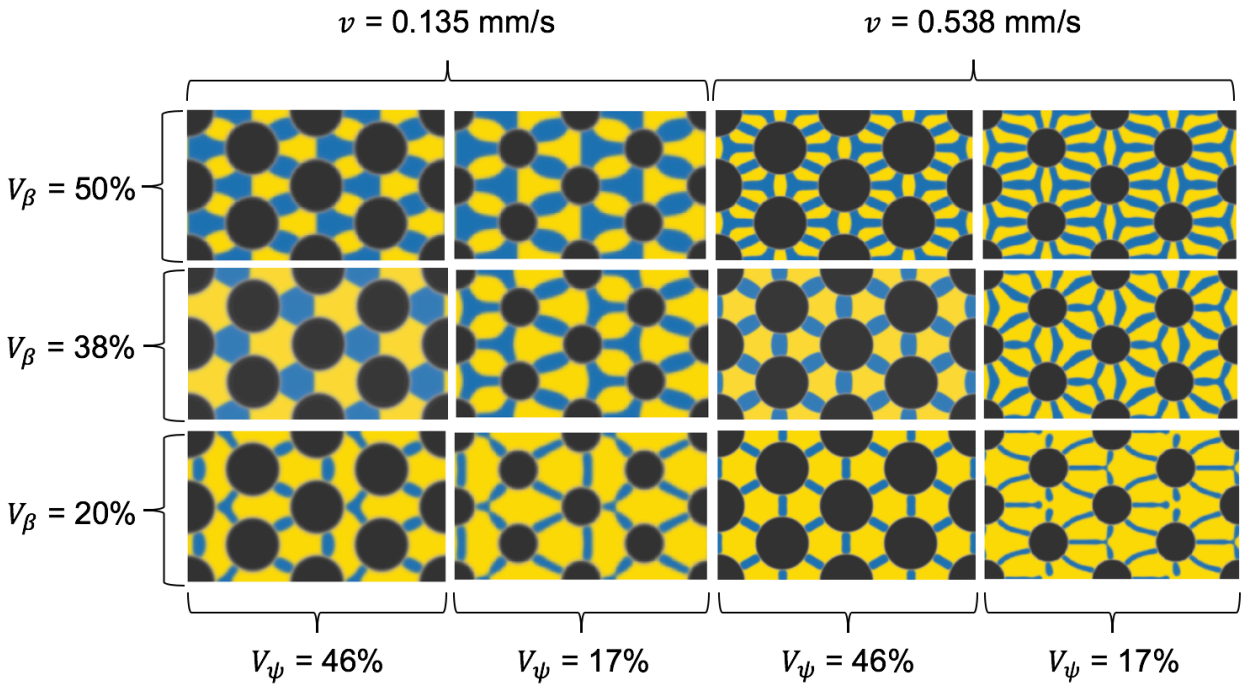

Figure 6.5 Self-organized patterns from parameter sweep: Patterns observed in phase-field simulations showing the steady-state structures that result from different combinations of three minority phase volume fractions, $V_\beta = 50\%$, 38%, and 20%; two template volume fractions, $V_\psi = 46\%$ and 17%; and two solidification velocities, $v = 0.135$ mm/s and 0.538 mm/s.

Table 6.1 Structure types from v-V_ψ-V_β parameter sweep.

v (mm/s)	V_ψ	V_β	Structure Type
0.135	46%	50%	5-spoke
0.135	46%	38%	3-spoke
0.135	46%	20%	4/5-spoke
0.135	17%	50%	5-spoke
0.135	17%	38%	5-spoke
0.135	17%	20%	4/5-spoke
0.538	46%	50%	10-spoke
0.538	46%	38%	6-spoke
0.538	46%	20%	6-spoke
0.538	17%	50%	10-spoke
0.538	17%	38%	9-spoke
0.538	17%	20%	7-spoke

Structures comprising higher numbers of spokes have smaller diffusion distances between disconnected regions of the same phase (e.g., KCl spokes). From Figure 6.5 and Table 6.1, it can be observed that a structure has features with a lower length scale when solidification velocity is increased. This is expected as it is consistent with eutectic solidification without template-direction.[57] Likewise, decreasing the minority phase volume fraction increases the number of spokes. With less KCl available, the connectivity of that phase has to decrease to preserve consistent diffusion distances. Similarly, as the pillar diameters decrease, there is more space for the structure to arrange itself, leading to smaller features sizes to maintain consistent spacing.

6.5 Conclusion

Template-directed self-assembly has been demonstrated to yield a broad diversity of highly ordered mesostructures[61,239-241], which in a few cases even exhibit symmetries not present in the native material.[140,242] Here we show using the directional solidification of a simple AgCl-KCl lamellar eutectic within a pillar template that interactions of the eutectic with the template lead to the emergence of an unprecedented set of microstructures, distinctly different from the eutectic's native lamellar structure and the template's hexagonal lattice structure. By modifying the solidification rate, in the same material-template system, disordered, trefoil, quatrefoil, cinquefoil, and hexafoil mesostructures with sub-micron size features are realized. Phase-field simulations suggest these mesostructures appear due to constraints imposed on diffusion by the hexagonally arrayed pillar template. Interestingly, the trefoil and hexafoil patterns bear a remarkable resemblance to Archimedean honeycomb and square-hexagonal-dodecagonal lattices,[243] respectively. Phase-field simulations were further utilized to elucidate a part of the vast parameter space associated with the template-directed eutectic solidification approach. It was discovered that the eutectic microstructure feature size could be adjusted not only by adjusting the solidification velocity, but also by changing the volume fractions of either the minority eutectic phase or the template. We anticipate these results will stimulate new studies on template-directed organization of inorganic materials into unique and useful mesostructures, including mesostructures which may have important optical,[244] magnetic[245], and mechanical[246] properties.

Chapter 7: Simulating Hindered Grain Boundary Diffusion Using the Smoothed Boundary Method

7.1 Introduction

We propose a diffuse interface approach based on the Smoothed Boundary Method (SBM) to solve the diffusion equation with hindrance at the interfaces between grains. Diffuse interface models, which circumvent the need for explicit interface tracking or remeshing for even complex geometries, have proven successful for calculating concentration evolution in inhomogeneous systems.[47,52] The proposed model is compared to a sharp interface model in one dimension. The effect of the numerical and physical parameters on the error of the model is explored. Finally, two case studies are presented. The first case study is oxygen diffusion in nanocrystalline YSZ, in which the effective diffusivities of the inhomogeneous structures are calculated and compared to mean field approximations. The second case study is the lithiation of a polycrystalline battery cathode particle.

7.2 Simulation Method

The hindered grain boundary diffusion model described in Chapter 3 Section 3.3 was utilized to simulate the systems described in this chapter. Specifically, Equations 3.35 and 3.36 were solved for the sharp-interface results and Equation 3.39 for all other results. The finite difference method was used for spatial discretization with a forward Euler time stepping scheme. The time step used was $\Delta t = 0.05\Delta x^2/D_{bulk}$. To avoid rounding error, all parameters were nondimensionalized for simulations using a length scale W equal to the grain size and a time scale $\tau = W^2/D_{bulk}$ such that nondimensional bulk diffusivity was equal to unity. For the three-dimensional structures, W was equal to the smallest grain size (40 nm for YSZ and 100 nm for NMC). Concentrations are scaled to fall within the range of zero to one. The domain sizes for the YSZ simulations in Section 7.4 were 120×120×120 and 20×120×120 grid points for the 240 nm and 40 nm structures respectively. The domain size for the NMC simulation in Section 7.5 was 240×240×240 grid points. Before smoothing, grains in the domain with the center of mass located outside the sphere of diameter equal to the nominal secondary (polycrystalline) particle diameter were removed, leaving a rough surface similar to those of experimentally synthesized particles.[41] The cathode particle diameter was 216 grid points. The NMC particle is described by an additional domain parameter $\psi = \sum \phi_q$ with which the Dirichlet concentration boundary condition is set on the outside surface of the particle.[163] The isotropic and anisotropic structures in Section 7.6 had domain sizes of 320×320×320 grid points. As described in Chapter 3 Section 3.3.3, the three-dimensional microstructures are originally generated using Dream.3D[175] and then the order parameters were smoothed and reduced following the description in Ref. 47.

7.3 Error Analysis

For a one-dimensional system, we choose a domain which consists of three grains and two grain boundaries (Figure 7.1a) to include error resulting from the interaction between grain boundaries. The first and last grain in the domain have lengths half that of the other grain(s). This choice allows the bulk-to-interface ratio to remain constant regardless of the number of grains in the system.

A finite difference method using forward Euler time stepping is utilized. A series of model parameters are investigated and their effects on error are reported below. All of the parameters reported in this section and the next will use nondimensional ratios to present the results as generically applicable. The numerical parameter ratios are $\zeta/\Delta x$ (a measure of the resolution of the numerical interface) and $N_{gb}\zeta/L_x$ (a measure of the diffuse interface volume fraction, which is proportional to the thickness of the diffuse interface), where Δx is the grid spacing, L_x is the domain size and N_{gb} is the number of grain boundaries. The physical parameter ratios are D_{gb}/D_{bulk} and $g = N_{gb}\delta/L_x$, the latter of which is the physical grain boundary volume fraction. In addition, the effect of the number of grain boundaries is explored.

The sharp-interface model (Equations 3.35 and 3.36) and our model (Equation 3.39) are solved, and the two sets of the solutions are compared to assess the error introduced by the diffuse interfaces in our model. An initial parameter set of $\zeta/\Delta x = 1$, $N_{gb}\zeta/L_x = 1/96$, $D_{gb}/D_{bulk} = 1/50$, and $g = 1/40$ is employed. Figure 7.1b and 1c show concentration profiles for both models at an early time and at steady state, respectively. As expected, the concentration drops sharply at the grain boundaries, where chemical transport is hindered. The extent of the concentration drop increases with increasing degree of hindrance (see Figure 7.2).

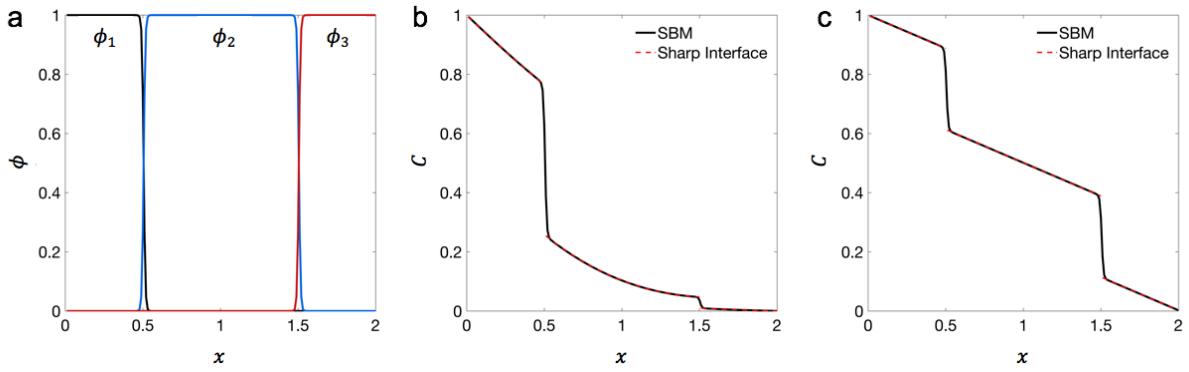

Figure 7.1 One-dimensional grain boundary system: (**a)** The domain parameter profiles for three grains with two grain boundaries. The concentration profiles for the diffuse-interface and sharp-interface models at **(b)** a time before steady state and **(c)** at steady state.

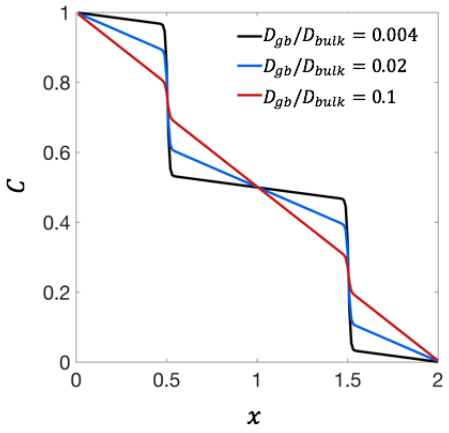

Figure 7.2 Concentration profiles for different degrees of hindrance in a three grain, two grain boundary one-dimensional system: As grain boundary diffusivity decreases (and degree of hindrance increases), concentration drops at the grain boundary become sharper.

The metric chosen with which to evaluate error is the average flux in the system at steady-state. This error is given by $\epsilon_{ss} = |J_{SBM} - J_{sharp}|/J_{sharp}$, where J_{SBM} and J_{sharp} are the average fluxes at steady state for our model and the sharp interface model, respectively. The dynamic error was also calculated as the system evolved and the maximum error over time was

recorded. For the majority of the parameter sets, the steady-state error was also the maximum error and therefore the analysis was limited to the steady-state error. The dynamic maximum error can be found in Figure 7.3.

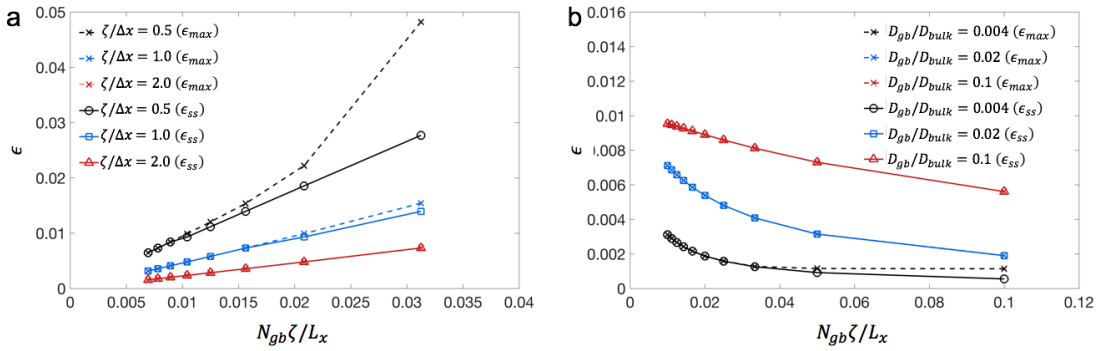

Figure 7.3 The maximum and steady-state error: (a) The error as a function of the numerical parameters $\zeta/\Delta x$ (interface resolution) and $N_{gb}\zeta/L_x$ (interface width). **(b)** The error as a function of the physical parameters D_{gb}/D_{bulk} and g. Dashed lines with X's show the dynamic maximum error in average flux. Solid lines show the error in average flux at steady state.

Figure 7.4a shows the effect of the numerical parameter ratios $\zeta/\Delta x$ and $N_{gb}\zeta/L_x$ on the error. While holding all other parameters constant, an increase in $\zeta/\Delta x$ (more grid points in the interface), decreases the error. Also, as $N_{gb}\zeta/L_x$ increases (thicker diffuse interface), the error increases. We then choose a parameter set which gives an error of less than 0.5% ($\zeta/\Delta x = 1$, $N_{gb}\zeta/L_x = 1/96$) to use for the next investigation, a sweep of the physical parameter ratios. Thus, there are common sets of parameters between the investigations and they are marked on the plots of Figure 7.4 with purple X's. Figure 7.4b shows the effect of the physical parameter ratios D_{gb}/D_{bulk} and g on the error. As D_{gb}/D_{bulk} increases, the error also increases. As g increases, the error decreases. This is due to the fact that $N_{gb}\zeta/L_x$ is held constant, and thus as grain size is reduced to increase g, L_x decreases and thus ζ decreases to compensate. Consequently, the resulting smaller interfacial thickness decreases error as g increases. The

parameter set of $\zeta/\Delta x = 1$, $N_{gb}\zeta/L_x = 1/96$, and $g = 1/40$ was then chosen to investigate the effect of N_{gb} on the error. Figure 7.4c shows that the error has practically no dependence on the number of grains aside from a very slight increase from two to more than two grains likely associated with grain boundaries interacting with one another.

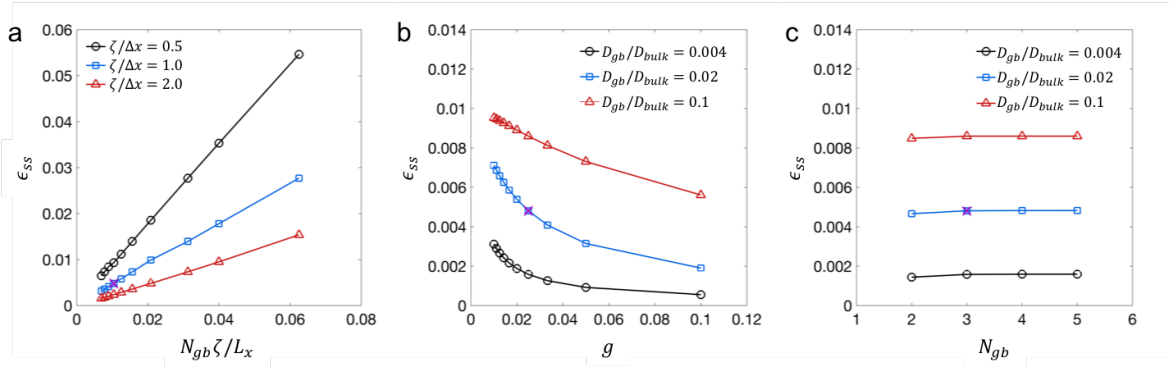

Figure 7.4 Error dependence on parameterization: (a) The error as a function of the numerical parameters $\zeta/\Delta x$ (interface resolution) and $N_{gb}\zeta/L_x$ (interface width). **(b)** The error as a function of the physical parameters D_{gb}/D_{bulk} and g. **(c)** The error as a function of D_{gb}/D_{bulk} and the number of grain boundaries. The purple X marks the common parameter set across the three plots.

7.4 Case Study 1 – Solid Oxide Fuel Cell

To use our model to accurately quantify the transport property of solid oxide fuel cell materials such as oxygen ion diffusion in yttria-stabilized zirconia (YSZ), the model must be extended into three dimensions:

$$\frac{\partial C_q}{\partial t} = D_{bulk}\frac{1}{\phi_q}\nabla\cdot\phi_q\nabla C_q + \frac{|\nabla\phi_q|}{\phi_q}\left[-\frac{1}{\kappa}\Delta C_{gb}\right] \tag{7.1}$$

An isotropic microstructure was generated with an average grain size of 50 nm[38] (with a range of 40-60 nm) and a thickness of 240 nm in each direction. The microstructure was generated and smoothed in the manner presented in Ref. 47 to obtain domain parameter interfaces with hyperbolic tangent function profiles with thicknesses and grid spacing corresponding to $N_{gb}\zeta/L_x = 1/25$ and $\zeta/\Delta x = 1$, respectively. The other physical parameters

used for YSZ are $D_{bulk} = 2.17 \times 10^{-13}$ m^2/s, $D_{gb} = 5.0 \times 10^{-15}$ m^2/s, and $\delta = 1$ nm.[38] This parameter set corresponds to an expected error of approximately 2% from Figure 7.4a.

Figure 7.5a shows the microstructure through plotting the sum of the square of the domain parameters. Figures 7.5b-d show the evolution of the concentration profile in the bulk of the YSZ. Sharp drops in concentration can be observed at the grain boundaries with a much more gradual concentration drop across the bulk of the grains.

An important application of this hindered grain boundary diffusion model is to use the steady-state concentration profile to calculate the effective diffusivity of the microstructure using the expression:

$$D_{eff} = \frac{J_{SBM} L_x}{(C_{out} - C_{in})} \tag{7.2}$$

where C_{in} and C_{out} are the concentration values for the Dirichlet boundary conditions at the beginning and end of the domain, respectively (one and zero, in this case). For the steady-state concentration profile in Figure 7.5d, we find $D_{eff} = 1.17 \times 10^{-13}$ m^2/s, whereas the experimentally reported value for effective diffusivity is 0.68×10^{-13} m^2/s. The discrepancy can be attributed to the uncertainty about the effective thickness of the grain boundary as the space charge layer thickness is greater than that of the grain boundary itself.[38] Additionally, there is uncertainty of the actual particle size distribution as only the average grain size of 50 nm was reported and the 40-60 nm range was arbitrarily chosen when generating the microstructure.

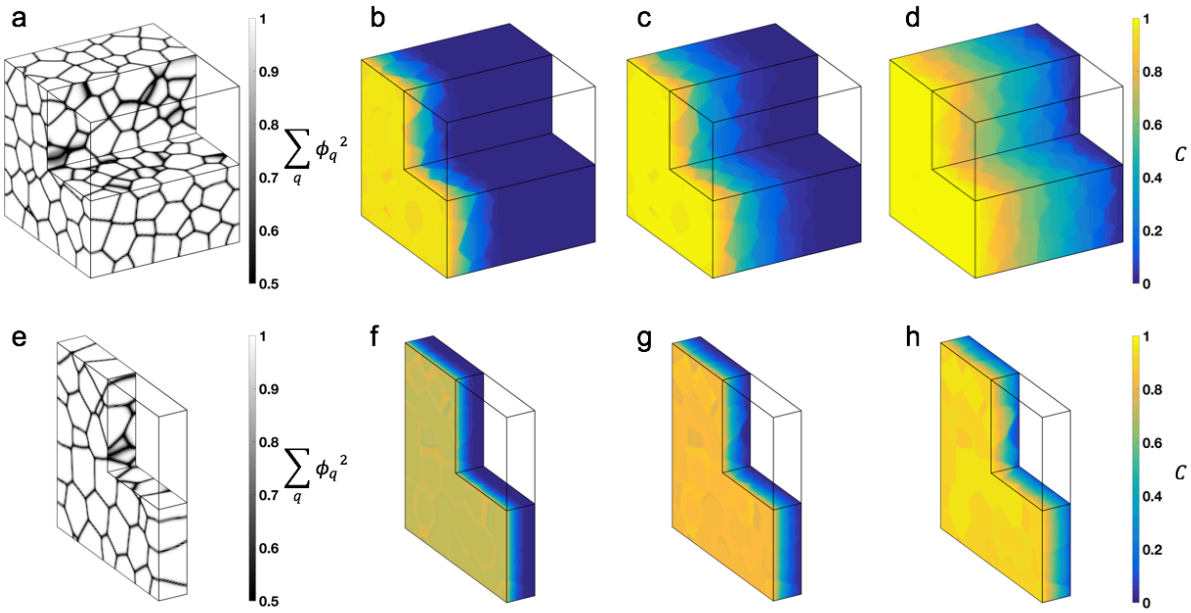

Figure 7.5 The microstructure and dynamic concentration profiles for YSZ: The sum of the square of the order parameters is plotted to show the grain boundaries of the **(a)** 240 nm thick YSZ structure and the **(e)** 40 nm thick YSZ structure. The concentration profiles are shown for **(b)** an early time, **(c)** a later time, and **(d)** at steady state for the 240 nm YSZ structure and **(f)** an early time, **(g)** a later time, and **(h)** at steady state for the 40 nm YSZ structure. Each plot has one quarter of the domain removed to see the interior.

There are multiple other models utilized to predict the effective diffusivity of polycrystalline solids in which grain boundary diffusivities differ from the bulk diffusivity. One such model is Hart's equation,[50] which assumes a simplified geometry where all grain boundaries are parallel to the diffusion direction:

$$D_{Hart} = gD_{gb} + (1-g)D_{bulk} \tag{7.3}$$

In a three-dimensional structure, the grain boundary volume fraction, g, is calculated by multiplying δ by the total area of the grain boundaries as calculated by summing the area of triangular patches generated from a MATLAB isosurface of the domain parameters. Another mean field approach is Maxwell Garnett's equation,[51] which assumes spherical grain boundaries:

$$D_{MG} = \frac{D_{gb}\left((3-2g)D_{bulk} + 2gD_{gb}\right)}{gD_{bulk} + (3-g)D_{gb}} \tag{7.4}$$

For the 240 nm thick YSZ microstructure, $D_{Hart} = 2.05 \times 10^{-13}$ m^2/s and $D_{MG} = 1.16 \times 10^{-13}$ m^2/s. The Maxwell Garnett prediction is very close to that of the numerical model because the spherical grain assumption is reasonable for an isotropic structure. The Hart model's assumption of parallel grain boundaries is not accurate and overestimates the effective diffusivity.

Not only is the presented numerical model more comprehensibly applicable than the existing mean field approaches (because it can dynamically predict the concentration profile), but it is also more robust when used only to predict the effective diffusivity, as it makes no assumptions about the geometry of grain boundaries. In the 240 nm thick microstructure, Maxwell Garnett's equation gives nearly the same result as the numerical model without the need – nor the cost – of a simulation. However, Maxwell Garnett's equation provides accurate predictions only when the structure is isotropic, as in this case. If we introduce an anisotropic microstructure in which grains are elongated in one direction, we expect the numerical model to become much more accurate than Maxwell Garnett's prediction. Another method to introduce anisotropy in the grain boundary structure is to consider a thin film with a thickness on the order of the grain size. In this case, there will be relatively fewer grain boundaries perpendicular to the diffusion direction. Figures 7.5e-h show the microstructure and concentration evolution of a 40 nm thick YSZ structure using the same average grain size of 50 nm. For this 40 nm thin film, we calculate $D_{eff} = 1.66 \times 10^{-13}$ m^2/s, $D_{Hart} = 2.08 \times 10^{-13}$ m^2/s, and $D_{MG} = 1.32 \times 10^{-13}$ m^2/s. The decrease in grain boundary volume fraction from the 240 nm to 40 nm structure (5.7% to 4.3%) results in an increase in D_{MG} by 14%. However, the numerical model, which accounts for both the change in volume fraction and the introduced anisotropy, predicts an increase in

D_{eff} of 42%. Hart's equation predicts very little change between the 240 nm and 40 nm structures as the assumption of parallel grain boundaries is already at the extreme limit of anisotropy and the change in volume fraction matters little in the parallel orientation.

7.5 Case Study 2 – Cathode Particle

Battery cathode particles often consist of an agglomeration of smaller, primary particles and thus are roughly spherical polycrystalline structures.[41] Our numerical model for hindered grain boundary diffusion can be applied to this case, where cracks that form at the grain boundaries during cycling are the sources of diffusion hindrance. The model is parameterized for the Nickel Manganese Cobalt oxide (NMC) cathode material with $D_{bulk} = 8.6 \times 10^{-18}$ m^2/s,[43] an average grain size of 150 nm (with a range of 100 nm to 200 nm), and a cathode particle size of 1 micron.[42] Because the crack width and effective diffusivity across the crack are not well studied, an arbitrary choice is made for the degree of hindrance ($\kappa = 1.0 \times 10^{11}$ s/m). This parameter could be tuned and the simulation results compared against experimental data to extract an accurate κ. The simulation numerical parameters are the same as those used in the YSZ case study.

A lithium fraction boundary condition of $C = 1$ is set at the surface of the particle that is initially devoid of lithium. Figures 7.6b-c show the evolution of the concentration as the cathode particle is filled with lithium. Again, sharp concentration drops can be seen at the grain boundaries where the cracks are inhibiting the lithium transport. Potential uses of this numerical model for cathode particles are to investigate the effects of cracks on cycling performance and/or coupling the concentration field to a mechanical solver to study the dynamic concentration's effects on stress and crack growth. Future work could be made more accurate by implementing a variable diffusivity which depends on the local concentration as lithium diffusivity in NMC is known to be concentration dependent.[43]

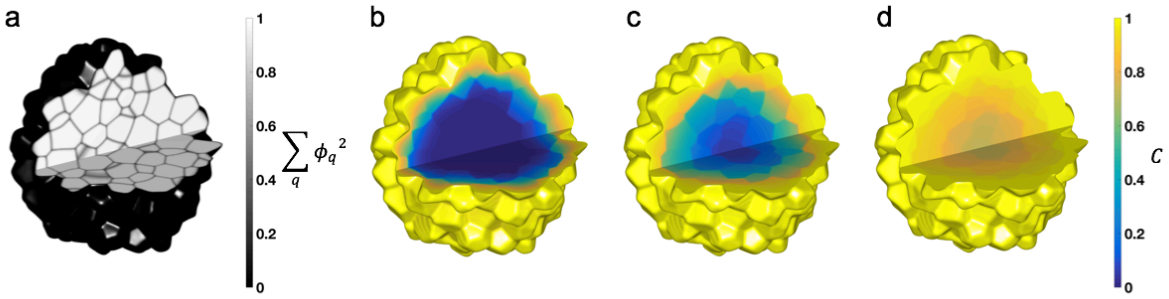

Figure 7.6 The microstructure and dynamic concentration profiles for a battery cathode NMC particle: (a) The sum of the square of the order parameters showing the grain boundaries of NMC particle. The concentration profiles are shown for **(b)** an early time, **(c)** a later time, and **(d)** at a time approaching complete lithiation. Each plot has one quarter of the domain removed to see the interior.

7.6 Isotropic vs. Anisotropic Grain Structures

7.6.1 Introduction

As noted in Section 7.4, one capability of this model is to extract effective diffusivities from microstructures without making any assumptions about the geometries of their grain boundaries. Therefore, the model is advantageous in that it can predict effective diffusivity values for structures with varying degrees of anisotropy, unlike the Hart[50] and Maxwell Garnett[51] equations, which assume straight and spherical grain boundaries, respectively. To reveal this benefit more clearly, we used the hindered grain boundary diffusion model to find the steady-state concentration profiles for an assortment of grain boundary geometries, extracted the effective diffusivity values, and compared them to the Hart and Maxwell Garnett mean-field approximation predictions.

7.6.2 Selected Structures and Concentration Profiles

To parameterize the system for this investigation, we chose nondimensional values of $D_{bulk} = 1$, $D_{gb} = 1/400$, and $\delta = 0.25$. Microstructures were generated with interface widths equivalent to $\zeta/\Delta x = 0.6$. The investigated microstructures are depicted in Figure 7.7 by

plotting the sum of the square of the order parameters. First, three isotropic structures were considered with subsequently larger grains and thus subsequently lower grain boundary volume fractions (see Figure 7.7a-c). Next, anisotropic structures comprising long, narrow, columnar-shaped grains with large aspect ratios were studied. The first columnar structure had the longest dimension of the grains parallel to the diffusion direction (Figure 7.7d) and the second had the grains oriented such that the longest dimension was perpendicular to the diffusion direction (Figure 7.7e). Finally, large, flat, plate-like grains were investigated with both long dimensions perpendicular (Figure 7.7f) and one long dimension parallel (Figure 7.7g) to the diffusion direction. The corresponding steady-state concentration profiles for each of these microstructures are shown in Figure 7.8.

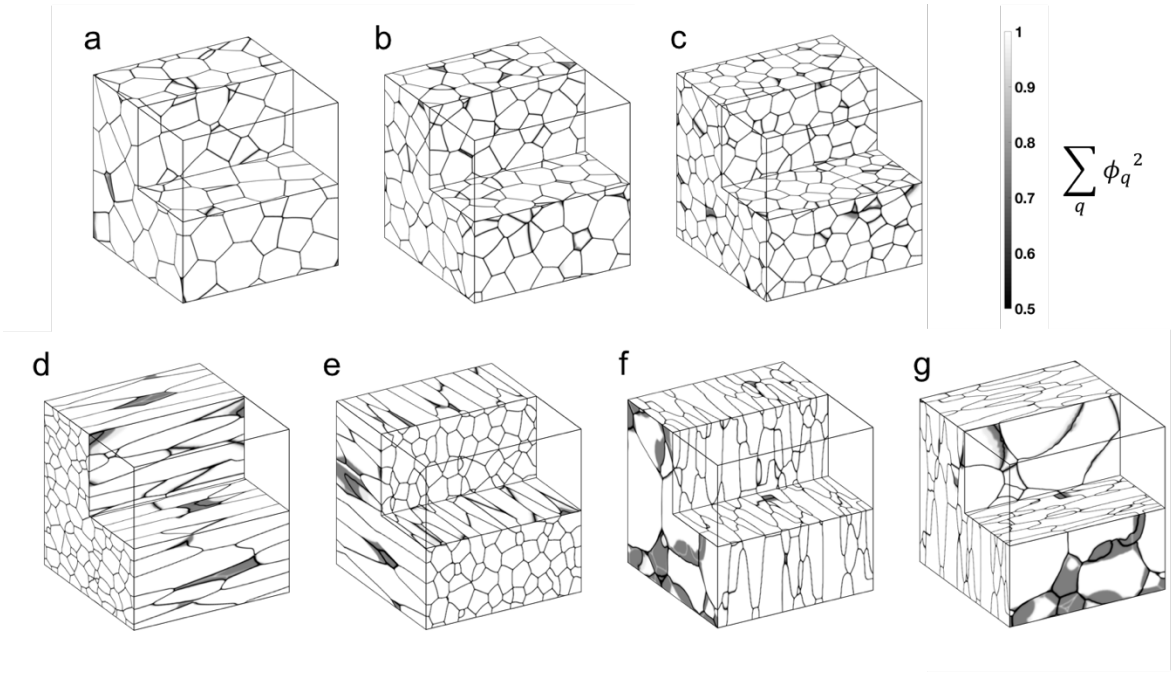

Figure 7.7 Isotropic and anisotropic grain boundary structures: The sum of the square of the order parameters are plotted for **(a)** large isotropic grains, **(b)** medium isotropic grains, **(c)** small isotropic grains, **(d)** columnar grains with the longest dimension parallel to the diffusion direction, **(e)** columnar grains with the longest dimension perpendicular to the diffusion direction, **(f)** plate-like grains with both long dimensions perpendicular to the diffusion direction, and **(g)** plate-like grains with the one long dimension parallel to the diffusion direction. One quarter of the domain is removed for visibility.

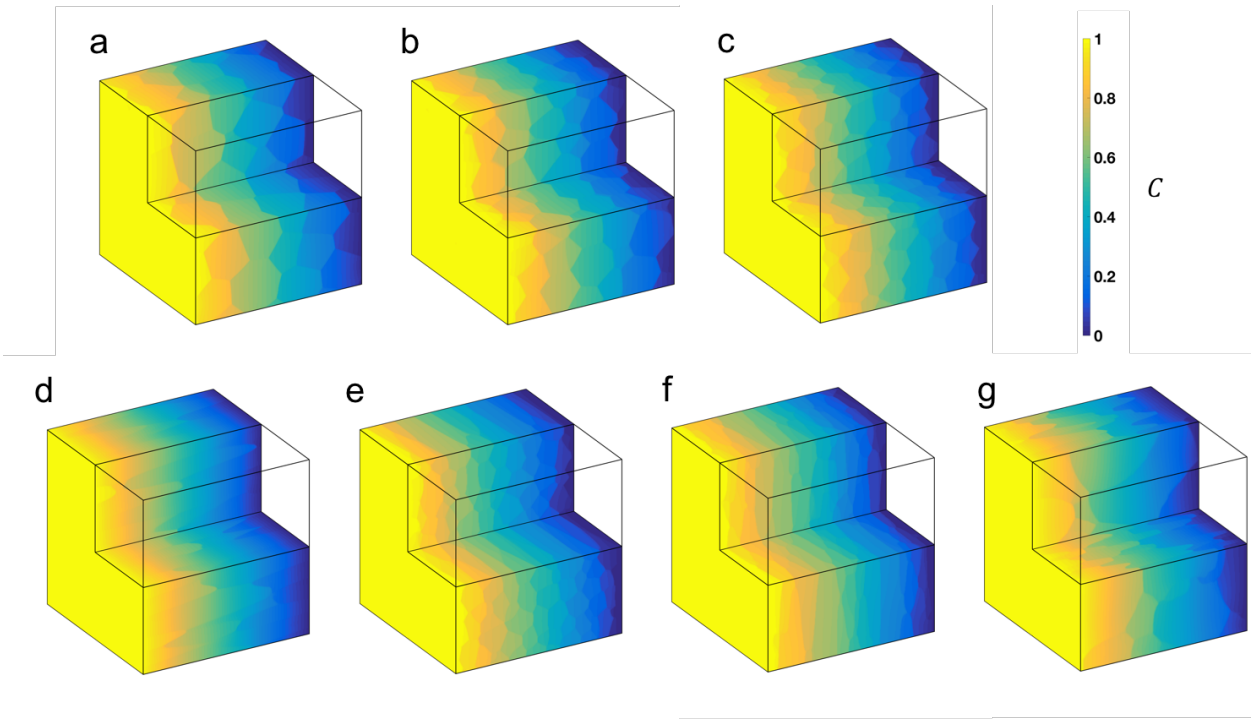

Figure 7.8 Steady-state concentration profiles: The steady-state concentration profiles are plotted for **(a)** large isotropic grains, **(b)** medium isotropic grains, **(c)** small isotropic grains, **(d)** columnar grains with the longest dimension parallel to the diffusion direction, **(e)** columnar grains with the longest dimension perpendicular to the diffusion direction, **(f)** plate-like grains with both long dimensions perpendicular to the diffusion direction, and **(g)** plate-like grains with the one long dimension parallel to the diffusion direction. One quarter of the domain is removed for visibility.

Once again, effective diffusivities were calculated from the steady-state concentration profiles using Equation 7.2. The results are shown in Figure 7.9 and listed in Table 7.1. In general, the Hart equation consistently overestimates the effective diffusivity because its assumption of parallel grain boundaries corresponds with the least impactful orientation for hindering grain boundaries. The prediction of the Hart equation which best matches the calculated effective diffusivity is for the structure consisting of columnar grains with the longest direction parallel to the diffusion direction. This is consistent with the expectation because that particular structure is predominantly composed of grain boundaries which are parallel to the diffusion direction.

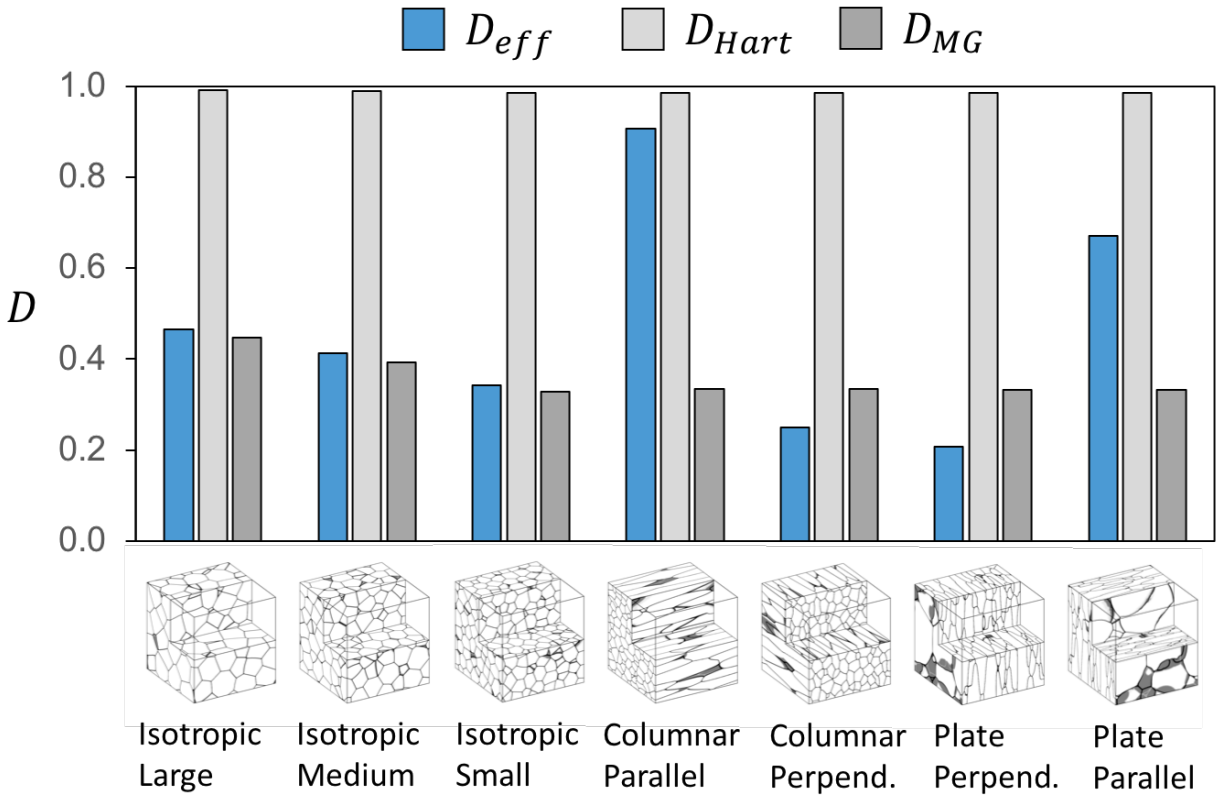

Figure 7.9 Effective diffusivity comparison: The numerically determined effective diffusivities for each of the isotropic and anisotropic microstructures compared to mean-field approximations (Hart and Maxwell Garnett).

Table 7.1 Our model's effective diffusivity compared to Hart and Maxwell Garnett predictions.

Structure	g	D_{eff}	D_{Hart}	D_{MG}
a. Isotropic – large	0.92%	0.465	0.991	0.446
b. Isotropic – medium	1.15%	0.414	0.989	0.392
c. Isotropic – small	1.51%	0.343	0.985	0.329
d. Columnar - parallel	1.48%	0.906	0.985	0.333
e. Columnar - perpendicular	1.48%	0.249	0.985	0.333
f. Plate - perpendicular	1.48%	0.207	0.985	0.333
g. Plate - parallel	1.48%	0.671	0.985	0.333

The Maxwell Garnett prediction and our model's prediction match well for the isotropic grain boundaries, an expected result as the Maxwell Garnett's geometric assumption of spherical grain boundaries is close to valid for isotropic grains. As the grain size decreases and g increases, the Maxwell Garnett equation predicts a decrease in diffusivity and our model follows the same trend. The two cases where the Maxwell Garnett equation predicts a lower diffusivity than our model (the columnar and plate-like structures oriented perpendicularly to the diffusion direction) are expected as those are the structures with a greater fraction of grain boundaries perpendicular to the diffusion direction than sphere-shaped or isotropic grains would have. Thus, structures with more grain boundaries perpendicular to the diffusion direction hinder diffusion to a greater degree, as is expected intuitively. Our model predicts effective diffusivities that are 75% and 62% of the Maxwell Garnett prediction for the perpendicular columnar and plate-like structures, respectively. Conversely, the columnar and plate-like structures in the parallel configuration exhibit less hindrance of diffusion as there are greater distances species can diffuse before encountering grain boundaries. As a consequence of that anisotropy, our model predicts significantly higher effective diffusivities in those cases than the Maxwell Garnett equation does (270% higher for the columnar structure and 200% for the plate-like structure). The effects of anisotropy on effective diffusivity are clear and the model's utility in accounting for those effects has been demonstrated.

7.7 Conclusion

We developed a numerical model that utilizes the SBM and accurately predicts the concentration evolution in polycrystalline structures with hindered grain boundary diffusion. The simulated concentration profiles can be used to study the effects of grain morphology on chemical transport in systems such as solid oxide fuel cell and battery cathode materials. Effective transport properties can be extracted from simulation results without resorting to grain

boundary geometry assumptions that are necessary for mean-field approaches. In one such case, for a nanocrystalline YSZ material, the developed model predicts a 42% increase in effective diffusivity when constrained to a thin film while the Maxwell Garnett approach (a mean-field approximation which does not account for the actual geometry) predicts only a 14% increase. A host of other anisotropic structures were examined as well, with effective diffusivities predicted by our model differing significantly from the Hart and Maxwell Garnett approaches. The model also enables future investigations of systems with hindered grain boundary diffusion in which other physics could be coupled to the concentration field, such as reaction kinetics or mechanical response.

Chapter 8: Effective Transport Properties of Polycrystalline Solids with Hindered Grain Boundary Diffusion

8.1 Introduction

Although mean-field approximations such as the Hart[50] and Maxwell Garnett[51] equations offer an estimation for the effective diffusivity of polycrystalline solids, based upon the observations in Chapter 7, we know that the effective diffusivity are determined not only by the grain boundary volume fraction on which these expressions depend, but also the degree of anisotropy and the configuration of the microstructure. While the effective diffusivity extracted from the steady-state concentration profiles produced by the hindered grain boundary diffusion model fully accounts for the geometry of the grain boundaries, this method requires numerical simulations that necessitate much greater computational cost than the simple evaluation of the mean-field approximations. Thus, a mean-field expression for effective diffusivity that depends on the actual geometry of a microstructure without a high computational cost would be highly

useful. We have developed such an expression and propose its applications for parameterizing coarse-grained models utilizing only the physical constants and the grain boundary geometry.

8.2 Circuitry Analogy and Grain Boundary Orientation

As observed in Chapter 7, grain boundaries that hinder diffusion lead to lower effective diffusivity when the grain boundaries are primarily perpendicular to the diffusion direction than when they are aligned with the diffusion direction. An effective analogy is that of circuitry. If we consider a hindering grain boundary to be an electrical resistor, a configuration in which it is in parallel with a bulk region of a grain (analogous to an electrical conductor), it will have little effect on lowering the conductivity of the circuit. Conversely, a resistor in series with a conductor has a much more considerable impact on the circuit's conductivity. In general, polycrystalline solids contain grain boundaries which are neither perpendicular nor parallel to the diffusion direction, but are rather at some intermediate orientation. The closer to perpendicular to the diffusion direction a grain boundary is, the greater its hindering effect on the diffusivity of the structure at large. Consequently, an accurate expression for effective diffusivity must take into account the effect of the grain boundary orientation. When considering the structure as a whole, the critical parameter thus becomes the fraction of the grain boundary area which is contributing in-parallel (the fraction that is parallel to the diffusion direction, $f_{\parallel}$) versus in-series (the fraction that is perpendicular to the diffusion direction, $f_{\perp}$), rather than the grain boundary volume fraction alone.

8.3 Projection Method and Universal Expression

Because grain boundaries can have arbitrary shapes, we must treat them numerically and thus we require discretization. This is accomplished by utilizing the isosurface tool in MATLAB to create a mesh consisting of triangular faces. The fraction of a triangular face's area which contributes perpendicularly can be found by projecting the unit vector normal to the plane of the

face, $\hat{n}$, onto the unit vector in the diffusion direction, $\hat{d}$. Performing a weighted average on the perpendicular contribution of each face, weighted by the faces' areas (A_i for face i), gives the fraction of the total area of the grain boundary network that is perpendicular to the diffusion direction.

$$f_{\perp} = \frac{\sum_i A_i \left(\hat{n}_i \cdot \hat{d}\right)^2}{\sum_i A_i} \tag{8.1}$$

Conversely, $f_{\parallel} = 1 - f_{\perp}$. We then consider the combination of the bulk, perpendicular grain boundary, and parallel grain boundary contributions to the diffusivity of a structure. First, the fast diffusion contributions (bulk and parallel grain boundary) are considered by adapting Hart's equation[50] (which assumes all grain boundaries and bulk regions to be parallel to one another). The equation is modified such that the arithmetic mean is weighted by the volume fraction of parallel grain boundaries, $f_{\parallel} g$, and the bulk, $1 - g$, for D_{gb} and D_{bulk}, respectively:

$$D_{\parallel} = \frac{f_{\parallel} g D_{gb} + (1-g) D_{bulk}}{f_{\parallel} g + (1-g)} \tag{8.2}$$

The parallel diffusivity contribution is then added in-series with the contribution of perpendicular grain boundaries using a weighted harmonic mean to obtain the final projection-method diffusivity prediction:

$$D_{proj} = \frac{1}{\frac{f_{\perp} g}{D_{gb}} + \frac{f_{\parallel} g + (1-g)}{D_{\parallel}}} \tag{8.3}$$

Equations 8.2 and 8.3 represent a universal description for effective diffusivity based only on physical and geometric constants. In point of fact, the projection method diffusivity prediction also applies to cases with enhanced grain boundary diffusivity. The next section aims to explore extreme cases to ensure that the model reduces to simpler models as expected.

8.4 Limiting Cases

In the limit of entirely parallel grain boundaries ($f_\perp = 0$, $f_\parallel = 1$), the first term in the denominator of Equation 8.3 is zero. Substituting Equation 8.2 in for $D_\parallel$ gives $D_{proj} = gD_{gb} + (1-g)D_{bulk}$. This is equivalent to Hart's equation,[50] as is expected in the limit of parallel grain boundaries.

In the limit of $D_{gb} = 0$, while $D_\parallel$ is nonzero, the first term in the denominator of Equation 8.3 is infinity. Thus, $D_{proj} = 0$, which is logical for a structure with grain boundaries that are completely impermeable to diffusion.

Finally, for the case where grain boundaries are neither hindering nor enhancing ($D_{gb} = D_{bulk}$), Equation 8.2 reduces to $D_\parallel = D_{gb} = D_{bulk}$ and Equation 8.3 reduces to a harmonic mean of two equivalent values, giving $D_{proj} = D_{gb} = D_{bulk}$. The effective diffusivity predicted by the projection method is entirely independent of the grain boundary volume fraction and orientation, as expected for a structure with homogeneous transport properties.

8.5 Single Grain Boundary Example

We consider two-dimensional systems with one grain boundary whose normal unit vector is oriented at different angles, θ, with respect to the diffusion direction. To parameterize the system for this investigation, we choose nondimensional values of $D_{bulk} = 1$, $D_{gb} = 1/400$, $\delta = 0.25$, and $\zeta/\Delta x = 0.5$. Figure 8.1 displays the concentration profiles, effective diffusivities, D_{eff}, obtained from the numerical model described in Chapter 7, and effective diffusivities obtained from the projection method (D_{proj}). As expected, as θ increases, the effective diffusivity becomes less hindered by a grain boundary which is increasingly parallel to the

diffusion direction. Good agreement between the two effective diffusivity calculations is demonstrated, with a lower than 0.5% difference in all cases.

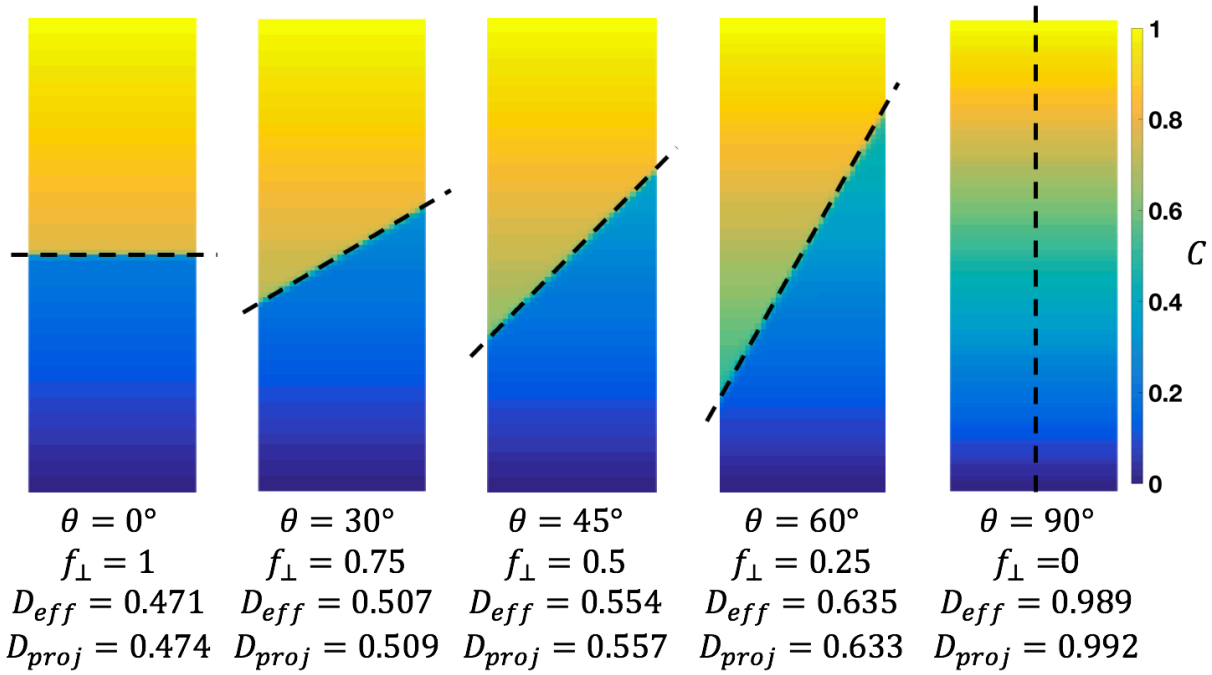

Figure 8.1 Single grain boundaries at different orientations: The steady-state concentration profiles for five grain boundary orientations are shown along with the calculated effective diffusivities from the hindered grain boundary diffusion and projection methods. Dashed lines represent the location of grain boundaries.

8.6 Isotropic vs. Anisotropic Structures

Finally, we compare the projection method calculations for effective diffusivity to the numerically determined effective diffusivity of the hindered grain boundary diffusion method of Chapter 7 as well as the mean-field approximations of Hart[50] and Maxwell Garnett.[51] The comparison was undertaken for the same isotropic and anisotropic polycrystalline structures that were used in the study in Chapter 7. Figure 8.2 and Table 8.1 display the results of the comparison for each structure.

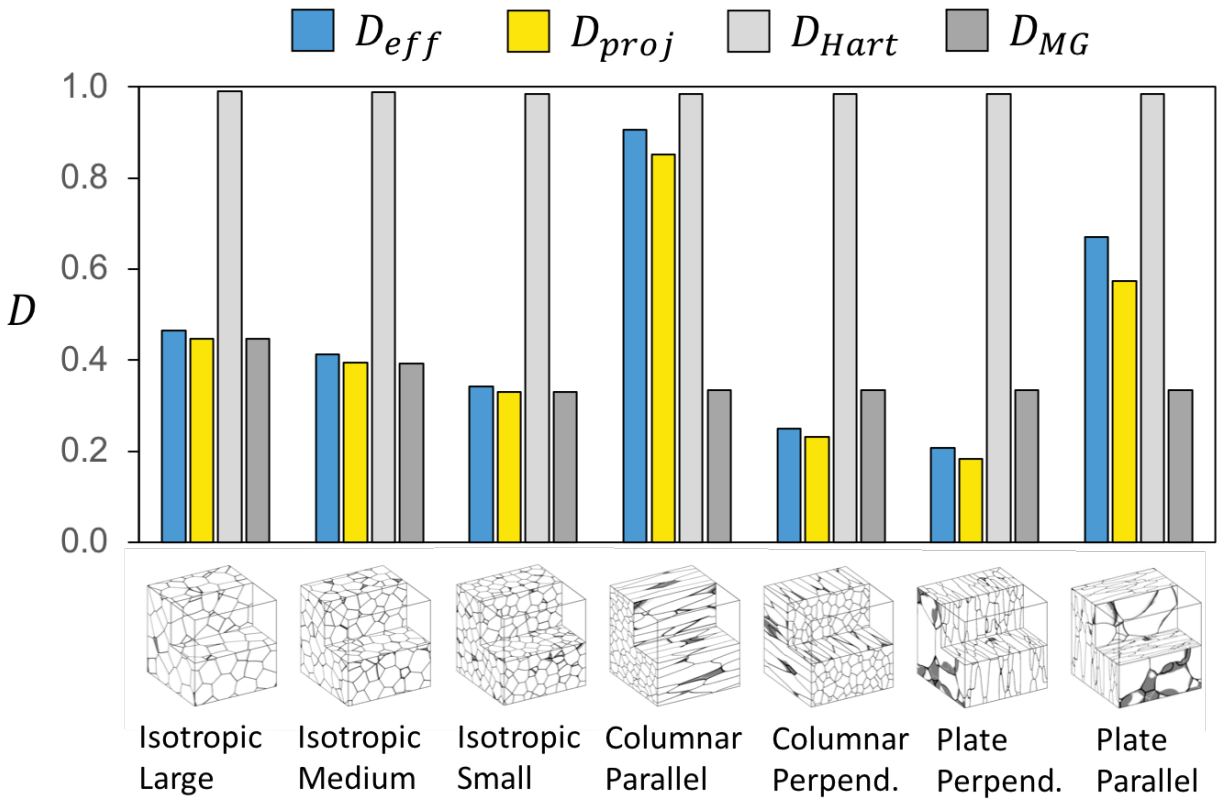

Figure 8.2 Comparison of the calculated effective diffusivities: The effective diffusivities from the hindered grain boundary diffusion simulations from Chapter 7 are compared to the effective diffusivity calculated by the projection method, as well as the other mean-field approximations of Hart and Maxwell Garnett.

Table 8.1 Our model's effective diffusivity compared to Hart and Maxwell Garnett predictions.

Structure	g	D_{eff}	D_{proj}	D_{Hart}	D_{MG}
a. Isotropic – large	0.92%	0.465	0.447	0.991	0.446
b. Isotropic – medium	1.15%	0.414	0.394	0.989	0.392
c. Isotropic – small	1.51%	0.343	0.330	0.985	0.329
d. Columnar - parallel	1.48%	0.906	0.851	0.985	0.333
e. Columnar - perpendicular	1.48%	0.249	0.231	0.985	0.333
f. Plate - perpendicular	1.48%	0.207	0.183	0.985	0.333
g. Plate - parallel	1.48%	0.671	0.573	0.985	0.333

For the isotropic microstructures, D_{eff}, D_{proj}, and D_{MG} all show good agreement, with the greatest difference between D_{eff} and D_{proj} being 5% and the greatest difference between D_{MG} and D_{proj} being only 0.5%. Once again, the agreement with Maxwell Garnett is expected where isotropic structures are similar to the spherical grain boundary assumption. For the columnar and plate-like grain structures, the projection method provides predictions that more closely match D_{eff} than either the Hart or Maxwell Garnett approximations. This is the case both in the parallel configuration where the effective diffusivity is lower than D_{Hart} but higher than D_{MG}, and in the perpendicular configuration where the effective diffusivity is lower than both other mean-field approximations. The noticeable differences between D_{eff} and D_{proj} in the parallel orientations for the columnar (7% difference) and plate-like (15% difference) grain structures are likely due to the microstructures not containing a representative volume of the microstructure. In the columnar case, there are grains which extend the length of the domain and provide a free path for unhindered diffusion. In the plate-like case, some grains extend farther than half of the length of the domain. Under these circumstances, the geometric parameters utilized in the projection method may not accurately capture the behavior of a microstructure with low-number statistics. However, even with a potentially unrepresentative volume, the projection method's prediction is much closer to D_{eff} than either the Hart or Maxwell Garnett mean-field approximations.

Let us briefly consider that the goal of the projection method is to achieve a better match to D_{eff} than either the Hart or Maxwell Garnett approaches for anisotropic microstructures. Because the Hart approach is only superior to Maxwell Garnett in one condition, we will focus on the comparisons to the Maxwell Garnett calculations. For the columnar structures, D_{proj} is 57% and 27% closer to D_{eff} than D_{MG} is for the parallel and perpendicular configurations,

respectively. For the plate-like structures, D_{proj} is 36% and 49% closer to D_{eff} than D_{MG} is for the parallel and perpendicular configurations, respectively. In each case, the projection method more closely matches the results of the hindered grain boundary diffusion simulation than the Maxwell Garnett equation does.

8.7 Conclusion

We developed a universal expression that can be used to predict effective diffusivities directly from physical materials constants and the geometry of a polycrystalline microstructures. This projection method accounts for in-parallel and in-series contributions of diffusion in the grain boundaries by accounting for parallel and perpendicular components of the grain boundaries, respectively. The effective diffusivities agree very well with the existing Maxwell Garnett mean-field approximation (0.5% difference or less) for isotropic microstructures, for which Maxwell Garnett's assumptions are valid. The projection method better predicts the effective diffusivity of anisotropic structures than other mean-field approximations such as the Hart and Maxwell Garnett equations without the use of potentially costly numerical simulation. When utilizing the results from the numerical hindered grain boundary diffusion model (explained in Chapter 7) as a baseline, the accuracy of the projection method's prediction exceeds that of Maxwell Garnett by up to 57%. The projection method expression can also be used to parameterize coarse-grained models with effective diffusivity values based on actual microstructure geometry.

Chapter 9: Summary and Future Work

9.1 Summary

In this thesis, a phase-field model for template-directed eutectic solidification was developed and its utility was demonstrated in a variety of cases. The model facilitated template design, guided the efforts of experimentalists, and provided insight into the template-directed eutectic solidification approach and its application for synthesizing functional optical materials.

In Chapter 4, several cases of eutectic solidification under geometric confinement were explored. The high operating temperature direct ink writing printing process was demonstrated in Section 4.1. Heat transfer calculations elucidated the solidification front shape and velocity and allowed a better understanding of the printing velocity's relationship with solidification velocity and microstructural evolution in the AgCl-KCl filament. Phase-field simulations of the eutectic filament's solidification agreed well with the experimental observations. In Section 4.2, solidification of AgCl-KCl was confined to the surface of a three-dimensional cage framework. The inhomogeneous cross section of the cage led to a curved solidification front where lamellae curved at the edges of the ribbon. A heat transfer calculation predicted this phenomenon, and the phase-field model demonstrated the resulting morphology, which had good agreement with the experimental observations. A rod-to-lamellar transition in AgCl-$CsAgCl_2$ was studied in Section

4.3. Under rapid solidification, a lamellar structure formed and at lower velocities, a rod morphology was realized. The phase-field simulation results indicated that the structure that forms at the surface would persist into the bulk. In Section 4.4, contact angle boundary conditions in the phase-field model utilized to impose asymmetric wetting behavior between two solid eutectic phases with the template was demonstrated as a system in which core-shell and multilayer nanowires could be synthesized.

In Chapter 5, a lamellar reorientation phenomenon is described. When solidifying AgCl-KCl through templates consisting of an array of pillars, lamellae that otherwise would be aligned vertically, instead reorient themselves to be aligned horizontally. Phase-field simulations were first used to predict the microstructures (which agreed well with the experimentally obtained microstructures) and subsequently were used to quantify the undercooling for different solidification velocities for vertical and horizontal orientations. The significantly lower undercooling for the horizontal orientation explained the source of this reorientation phenomenon.

In Chapter 6, highly ordered patterns were obtained by solidifying AgCl-KCl eutectic in a direction parallel to the axis of pillars in a hexagonally arranged template. The resulting morphologies were similar to Archimedean lattices. The morphology obtained could be selected by changing only the solidification velocity and keeping the template geometry and material system constant, a unique trait of the template-directed eutectic solidification approach.

In Chapter 7, the hindered grain boundary diffusion method utilizing the Smoothed Boundary Method was introduced and demonstrated. The error of the model was explored as a function of numerical and physical parameters. Two case studies of physical materials were discussed. The first was the solid oxide fuel cell material YSZ in which oxygen ion transport is hindered at grain boundaries. The second case study was for an NMC battery cathode particle in

which lithium transport is hindered by cracks that form at the grain boundaries during charging and discharging. Finally, a series of isotropic and anisotropic polycrystalline structures was investigated and the effective diffusivities were calculated and compared to mean-field approximations. The hindered grain boundary diffusion model's effective diffusivity calculation has an advantage in that it makes no assumptions about grain boundary geometry and thus can accurately describe the transport properties of even anisotropic morphologies. It is also extendable to include effects such as misorientation-dependent grain boundary diffusivities.

Chapter 8 displayed a newly developed expression which can predict the effective diffusivity of a polycrystalline structure with enhanced or hindered grain boundary diffusivity. The expression requires only the diffusion coefficients, the grain boundary width, and the grain boundary geometry and provides a more accurate prediction for effective diffusivity than other mean-field approximations for anisotropic microstructures without the computational cost of a simulation.

9.2 Future Work

9.2.1 Nucleation Behavior on Template Surface

Observations made in experiments by Ashish Kulkarni, Julia Kohanek, and Paul Braun at the University of Illinois at Urbana-Champaign suggest that for some systems, nucleation of eutectic phases may be facilitated by the template surface. At times, the constraint on the evolution of the eutectic microstructure within a template can be significant and systems can become particularly frustrated when the solidification front becomes locally dominated by one solid phase or the other (leading to a higher concentration buildup of the opposite species ahead of the front). Nucleation is a potential mechanism to reduce the local spacing and return on an unfrustrated state. Therefore, if nucleation is more likely to occur due to the presence of a template surface, it could be important to capture that behavior in a model as its absence could

cause unphysical results. Future work could implement nucleation behavior at the template surface and a parametric study could be undertaken to understand the effects of this nucleation and where its influence is important within the parameter space of template-directed eutectic solidification.

9.2.2 Surface Patterning as a Template

In Chapter 4 Section 4.3, it was explained that there is a tendency for eutectic morphologies that form first at surface to persist throughout the bulk of a sample. This may be less apparent in eutectic systems other than AgCl-$CsAgCl_2$ which have volume fractions (and other materials parameters) that put themselves farther from the rod-lamellar transition point predicted by the Jackson-Hunt theory.[57] Nevertheless, the concept could enable the use of a surface template to impose an initial morphology that is preserved in the bulk. Perhaps a topographical pattern could be applied to a surface to bias toward the formation of a certain structure. A potentially more promising approach may be to apply onto a surface patches of material which one of the solid eutectic phases prefers to wet (a concept similar to that of the core-shell nanowire shown in Chapter 4 Section 4.4). For example, if these patches were arranged in a pattern resembling a cross section of a rod-like eutectic, perhaps the AgCl-$CsAgCl_2$ could be influenced to obtain a rod morphology even at higher solidification velocities.

9.2.3 Core-Shell Nanowire

Future work may utilize the concept that was demonstrated in Chapter 4 Section 4.4 in which a core-shell nanowire synthesis technique was proposed. While cylindrical channel templates made from anodic aluminum oxide have been experimentally explored,[140,247] the morphology observed in that case has been alternating sections of the two solid eutectic phases rather than a core-shell or layered morphology. A eutectic-template system which has

asymmetric wetting behavior between the two solid phases with the template surface would be necessary to realize this core-shell nanowire synthesis technique.

9.2.4 Battery Cathode Mechanics

The hindered grain boundary diffusion method demonstrated the ability to predict the concentration profile in a NMC battery cathode particle where cracks that form at the grain boundaries hinder lithium transport (Chapter 7 Section 7.5). The next step would be to couple this concentration field with a mechanical equilibrium solver to investigate the evolution of stress during charge and discharge and the effect of that stress on the concentration evolution and subsequently, the performance of the battery. This coupled model could also be used to elucidate the formation of the cracks in the first place.

Bibliography

1 Kulkarni, A. A. *et al.* Template-Directed Solidification of Eutectic Optical Materials. *Advanced Optical Materials* **6**, 20, doi:10.1002/adom.201800071 (2018).

2 Joannopoulos, J. D., Johnson, S. G., Winn, J. N. & Meade, R. D. Photonic Crystals: Molding the Flow of Light, 2nd Edition. *Photonic Crystals: Molding the Flow of Light, 2nd Edition*, 1-286 (2008).

3 Joannopoulos, J. D., Villeneuve, P. R. & Fan, S. H. Photonic crystals: Putting a new twist on light. *Nature* **386**, 143-149, doi:10.1038/386143a0 (1997).

4 Saleh, B. E. A. & Teich, M. C. *Fundamentals of photonics*. (Wiley, 1991).

5 Tong, X. C. & SpringerLink (Online service). (Springer International Publishing : Imprint: Springer, Cham, 2018).

6 Pendry, J. B. Negative refraction makes a perfect lens. *Physical Review Letters* **85**, 3966-3969, doi:10.1103/PhysRevLett.85.3966 (2000).

7 Tang, Y. & Cohen, A. E. Optical Chirality and Its Interaction with Matter. *Physical Review Letters* **104**, doi:10.1103/PhysRevLett.104.163901 (2010).

8 Kim, J. Y. *et al.* Highly tunable refractive index visible-light metasurface from block copolymer self-assembly. *Nature Communications* **7**, doi:10.1038/ncomms12911 (2016).

9 Soukoulis, C. M. & Wegener, M. Past achievements and future challenges in the development of three-dimensional photonic metamaterials. *Nature Photonics* **5**, 523-530, doi:10.1038/nphoton.2011.154 (2011).

10 Urbas, A. M. *et al.* Roadmap on optical metamaterials. *Journal of Optics* **18**, doi:10.1088/2040-8978/18/9/093005 (2016).

11 Yatsui, T. & SpringerLink. Nanophotonic Fabrication Self-Assembly and Deposition Techniques.

12 Isaacofft, B. P. & Brown, K. A. Progress in Top-Down Control of Bottom-Up Assembly. *Nano Letters* **17**, 6508-6510, doi:10.1021/acs.nanolett.7b04479 (2017).

13 Galisteo-Lopez, J. F. *et al.* Self-Assembled Photonic Structures. *Advanced Materials* **23**, 30-69, doi:10.1002/adma.201000356 (2011).

14 von Freymann, G., Kitaev, V., Lotschz, B. V. & Ozin, G. A. Bottom-up assembly of photonic crystals. *Chemical Society Reviews* **42**, 2528-2554, doi:10.1039/c2cs35309a (2013).

15 Chadwick, G. A. Eutectic Alloy Solidification. *Progress in Materials Science* **12**, 99-182 (1963).

16 Noshay, A., McGrath, J. E. & ScienceDirect. Block copolymers overview and critical survey.

17 De Rosa, C., Park, C., Thomas, E. L. & Lotz, B. Microdomain patterns from directional eutectic solidification and epitaxy. *Nature* **405**, 433-437 (2000).

18 Muthukumar, M., Ober, C. K. & Thomas, E. L. Competing interactions and levels of ordering in self-organizing polymeric materials. *Science* **277**, 1225-1232, doi:10.1126/science.277.5330.1225 (1997).

19 Zeng, H., Li, J., Liu, J. P., Wang, Z. L. & Sun, S. H. Exchange-coupled nanocomposite magnets by nanoparticle self-assembly. *Nature* **420**, 395-398, doi:10.1038/nature01208 (2002).

20 Boal, A. K. *et al.* Self-assembly of nanoparticles into structured spherical and network aggregates. *Nature* **404**, 746-748 (2000).

21 Choi, K. S., Lichtenegger, H. C., Stucky, G. D. & McFarland, E. W. Electrochemical synthesis of nanostructured ZnO films utilizing self-assembly of surfactant molecules at solid-liquid interfaces. *Journal of the American Chemical Society* **124**, 12402-12403, doi:10.1021/ja0275562 (2002).

22 Corma, A., Rey, F., Rius, J., Sabater, M. J. & Valencia, S. Supramolecular self-assembled molecules as organic directing agent for synthesis of zeolites. *Nature* **431**, 287-290, doi:10.1038/nature02909 (2004).

23 Winfree, E., Liu, F. R., Wenzler, L. A. & Seeman, N. C. Design and self-assembly of two-dimensional DNA crystals. *Nature* **394**, 539-544, doi:10.1038/28998 (1998).

24 Douglas, S. M. *et al.* Self-assembly of DNA into nanoscale three-dimensional shapes. *Nature* **459**, 414-418, doi:10.1038/nature08016 (2009).

25 Scott, B. J., Wirnsberger, G. & Stucky, G. D. Mesoporous and mesostructured materials for optical applications. *Chemistry of Materials* **13**, 3140-3150, doi:10.1021/cm0110730 (2001).

26 Lee, T. S., Chung, J. N. & Chen, Y. C. Design and optimization of a combined fuel reforming and solid oxide fuel cell system with anode off-gas recycling. *Energy Conversion and Management* **52**, 3214-3226 (2011).

27 Minh, N. Q. Solid oxide fuel cell technology - Features and applications. *Solid State Ionics* **174**, 271-277 (2004).

28 Mahato, N., Banerjee, A., Gupta, A., Omar, S. & Balani, K. Progress in material selection for solid oxide fuel cell technology: A review. **72**, 141-337 (2015).

29 Stambouli, A. B. & Traversa, E. Solid oxide fuel cells (SOFCs): A review of an environmentally clean and efficient source of energy. *Renewable and Sustainable Energy Reviews* **6**, 433-455 (2002).

30 Ahamer, C., Opitz, A. K., Rupp, G. M. & Fleig, J. Revisiting the Temperature Dependent Ionic Conductivity of Yttria Stabilized Zirconia (YSZ). *Journal of the Electrochemical Society* **164**, F790-F803, doi:10.1149/2.0641707jes (2017).

31 Steele, B. C. H. & Heinzel, A. Materials for fuel-cell technologies. **414**, 345-352 (2001).

32 Nguyen, H. T., Mokkapati, S. & Macdonald, D. Detecting Dopant Diffusion Enhancement at Grain Boundaries in Multicrystalline Silicon Wafers With Microphotoluminescence Spectroscopy. *Ieee Journal of Photovoltaics* **7**, 598-603, doi:10.1109/jphotov.2017.2650561 (2017).

33 Yun, J. S. *et al.* Benefit of Grain Boundaries in Organic-Inorganic Halide Planar Perovskite Solar Cells. *Journal of Physical Chemistry Letters* **6**, 875-880, doi:10.1021/acs.jpclett.5b00182 (2015).

34 Jiang, C. S. *et al.* Does the local built-in potential on grain boundaries of Cu(In,Ga)Se-2 thin films benefit photovoltaic performance of the device? *Applied Physics Letters* **85**, 2625-2627, doi:10.1063/1.1793346 (2004).

35 Yan, Y. *et al.* Electrically benign behavior of grain boundaries in polycrystalline CuInSe2 films. *Physical Review Letters* **99**, 4, doi:10.1103/PhysRevLett.99.235504 (2007).

36 Rahman, M. M., Wang, J. Z., Hassan, M. F., Wexler, D. & Liu, H. K. Amorphous Carbon Coated High Grain Boundary Density Dual Phase Li4Ti5O12-TiO2: A Nanocomposite Anode Material for Li-Ion Batteries. *Advanced Energy Materials* **1**, 212-220, doi:10.1002/aenm.201000051 (2011).

37 Wang, C. *et al.* Combining Fast Li-Ion Battery Cycling with Large Volumetric Energy Density: Grain Boundary Induced High Electronic and Ionic Conductivity in Li4Ti5O12 Spheres of Densely Packed Nanocrystallites. *Chemistry of Materials* **27**, 5647-5656, doi:10.1021/acs.chemmater.5b02027 (2015).

38 De Souza, R. A. *et al.* Oxygen diffusion in nanocrystalline yttria-stabilized zirconia: the effect of grain boundaries. *Physical Chemistry Chemical Physics* **10**, 2067-2072, doi:10.1039/b719363g (2008).

39 Huang, H. C., Su, P. C., Kwak, S. K., Pornprasertsuk, R. & Yoon, Y. J. Molecular Dynamics Simulation of Oxygen Ion Diffusion in Yttria Stabilized Zirconia Single Crystals and Bicrystals. *Fuel Cells* **14**, 574-580, doi:10.1002/fuce.201300227 (2014).

40 Nakagawa, T. *et al.* Oxygen diffusion blocking of single grain boundary in yttria-doped zirconia bicrystals. *Journal of Materials Science* **40**, 3185-3190, doi:10.1007/s10853-005-2682-4 (2005).

41 Liu, H. *et al.* Intergranular Cracking as a Major Cause of Long-Term Capacity Fading of Layered Cathodes. *Nano Letters* **17**, 3452-3457, doi:10.1021/acs.nanolett.7b00379 (2017).

42 Fang, Y. C. *et al.* Synthesis of hollow peanut-like hierarchical mesoporous LiNi1/3Co1/3Mn1/3O2 cathode materials with exceptional cycle performance for lithium-ion batteries by a simple self-template solid-state method. *Journal of Alloys and Compounds* **743**, 707-715, doi:10.1016/j.jallcom.2018.01.257 (2018).

43 Amin, R., Ravnsbaek, D. B. & Chiang, Y. M. Characterization of Electronic and Ionic Transport in Li1-xNi0.8Co0.15Al0.05O2 (NCA). *Journal of the Electrochemical Society* **162**, A1163-A1169, doi:10.1149/2.0171507jes (2015).

44 Watanabe, S., Kinoshita, M., Hosokawa, T., Morigaki, K. & Nakura, K. Capacity fade of LiAlyNi1−x−yCoxO2 cathode for lithium-ion batteries during accelerated calendar and cycle life tests (surface analysis of LiAlyNi1−x−yCoxO2 cathode after cycle tests in restricted depth of discharge ranges). **258**, 210-217 (2014).

45 Li, W., Song, B. & Manthiram, A. High-voltage positive electrode materials for lithium-ion batteries. *Chemical Society Reviews* **46**, 3006-3059 (2017).

46 Yin, S. C., Rho, Y. H., Swainson, I. & Nazar, L. F. X-ray/neutron diffraction and electrochemical studies of lithium De/Re-intercalation in Li1-xCo1/3Ni1/3Mn1/3O2 (x=0 -> 1). *Chemistry of Materials* **18**, 1901-1910, doi:10.1021/cm0511769 (2006).

47 Yu, H. C., Choe, M. J., Amatucci, G. G., Chiang, Y. M. & Thornton, K. Smoothed Boundary Method for simulating bulk and grain boundary transport in complex polycrystalline microstructures. *Computational Materials Science* **121**, 14-22, doi:10.1016/j.commatsci.2016.04.028 (2016).

48 Fisher, J. C. Calculation of diffusion penetration curves for surface and grain boundary diffusion. *Journal of Applied Physics* **22**, 74-77, doi:10.1063/1.1699825 (1951).

49 Herzig, C. & Divinski, S. V. Grain boundary diffusion in metals: Recent developments. *Materials Transactions* **44**, 14-27, doi:10.2320/matertrans.44.14 (2003).

50 Hart, E. W. On the role of dislocations in bulk diffusion. *Acta Metallurgica* **5**, 597-597, doi:10.1016/0001-6160(57)90127-x (1957).

51 Garnett, J. C. M. Colours in metal glasses and in metallic films. *Philosophical Transactions of the Royal Society of London Series a-Containing Papers of a Mathematical or Physical Character* **203**, 385-420, doi:10.1098/rsta.1904.0024 (1904).

52 Kockelkoren, J., Levine, H. & Rappel, W. J. Computational approach for modeling intra- and extracellular dynamics. *Physical Review E* **68**, 4, doi:10.1103/PhysRevE.68.037702 (2003).

53 Calliser, W. D. & Rethwisch, D. G. Vol. 5 (John Wiley & Sons, Materials Science and Engineering, 2011).

54 Pawlak, D. A. *et al.* Self-organized, rodlike, micrometer-scale microstructure of Tb3Sc2Al3O12-TbSCO3 : Pr eutectic. *Chemistry of Materials* **18**, 2450-2457, doi:10.1021/cm060136h (2006).

55 Pawlak, D. A. *et al.* How Far Are We from Making Metamaterials by Self-Organization? The Microstructure of Highly Anisotropic Particles with an SRR-Like Geometry. *Advanced Functional Materials* **20**, 1116-1124, doi:10.1002/adfm.200901875 (2010).

56 Hunt, J. D. & Jackson, K. A. Binary eutectic solidification. *Transactions of the Metallurgical Society of Aime* **236**, 843-& (1966).

57 Jackson, K. A. & Hunt, J. D. Lamellar and rod eutectic growth. *Transactions of the Metallurgical Society of Aime* **236**, 1129-& (1966).

58 Scheil, E. Uber die eutektische kristallisation. *Zeitschrift Fur Metallkunde* **45**, 298-309 (1954).

59 Llorca, J. & Orera, V. M. Directionally solidified eutectic ceramic oxides. *Progress in Materials Science* **51**, 711-809, doi:10.1016/j.pmatsci.2005.10.002 (2006).

60 Sayir, A. *Directional solidification of eutectic ceramics*. (1999).

61 Kim, J. *et al.* Template-Directed Directionally Solidified 3D Mesostructured AgCl-KCl Eutectic Photonic Crystals. *Advanced Materials* **27**, 4551-4559, doi:10.1002/adma.201502265 (2015).

62 Boley, J. W. *et al.* High-Operating-Temperature Direct Ink Writing of Mesoscale Eutectic Architectures. *Advanced Materials* **29**, 8, doi:10.1002/adma.201604778 (2017).

63 Pena, J. I. *et al.* Microstructure of Y2O3 doped Al2O3-ZrO2 eutectics grown by the laser floating zone method. *Journal of the European Ceramic Society* **22**, 2595-2602, doi:10.1016/s0955-2219(02)00121-8 (2002).

64 Lee, J. H. *et al.* Microstructure of Y2O3 doped Al2O3/ZrO2 eutectic fibers grown by the micro-pulling-down method. *Journal of Crystal Growth* **231**, 179-185, doi:10.1016/s0022-0248(01)01451-8 (2001).

65 Yasui, N., Kobayashi, T., Ohashi, Y. & Den, T. Phase-separated CsI-NaCl scintillator grown by the Czochralski method. *Journal of Crystal Growth* **399**, 7-12, doi:10.1016/j.jcrysgro.2014.03.040 (2014).

66 Larrea, A., Contreras, L., Merino, R. I., Llorca, J. & Orera, V. M. Microstructure and Physical Properties of CaF2–MgO Eutectics Produced by the Bridgman Method. *Journal of Materials Research* **15**, 1314-1319 (2000).

67 Oliete, P. B. *et al.* Ultra-high-strength nanofibrillar Al2O3-YAG-YSZ eutectics. *Advanced Materials* **19**, 2313-+, doi:10.1002/adma.200602379 (2007).

68 Okamoto, H. *Phase Diagrams for Binary Alloys*. Vol. 314 (ASM International, 2000).

69 Villars, P., Prince, A. & Okamoto, H. *Handbook of Ternary Alloy Phase Diagrams*. (ASM International, 1995).

70 Kattner, U. R. & Massalski, T. B. *Binary Alloy Phase Diagrams*. Vol. 147 (ASM International, 1990).

71 Villars, P., Okamoto, H. & Cenzual, K. *ASM Alloy Phase Diagrams Database*. (ASM International, 2016).

72 Cubukcu, E., Aydin, K., Ozbay, E., Foteinopoulou, S. & Soukoulis, C. M. Negative refraction by photonic crystals. *Nature* **423**, 604-605, doi:10.1038/423604b (2003).

73 Yamada, I., Takano, K., Hangyo, M., Saito, M. & Watanabe, W. Terahertz wire-grid polarizers with micrometer-pitch Al gratings. *Optics Letters* **34**, 274-276, doi:10.1364/ol.34.000274 (2009).

74 Day, M. G. & Hellawell, A. Microstructure and crystallography of aluminium-silicon eutectic alloys. *Proceedings of the Royal Society of London Series a-Mathematical and Physical Sciences* **305**, 473-+, doi:10.1098/rspa.1968.0128 (1968).

75 Shahani, A. J., Xiao, X. & Voorhees, P. W. The mechanism of eutectic growth in highly anisotropic materials. *Nature Communications* **7**, doi:10.1038/ncomms12953 (2016).

76 Ebrahimi, Z. Modeling of eutectic formation in Al-Si alloy using a phase-field method. *Archives of Metallurgy and Materials* **62**, 1969-1981, doi:10.1515/amm-2017-0295 (2017).

77 Adams, C. D., Srolovitz, D. J. & Atzmon, M. Monte-Carlo Simulation of Phase-Separation During Thin-Film Codeposition. *Journal of Applied Physics* **74**, 1707-1715, doi:10.1063/1.354825 (1993).

78 Petrov, I., Barna, P. B., Hultman, L. & Greene, J. E. Microstructural evolution during film growth. *Journal of Vacuum Science & Technology A* **21**, S117-S128, doi:10.1116/1.1601610 (2003).

79 Fukutani, K., Tanji, K., Saito, T. & Den, T. Phase-separated Al-Si thin films. *Journal of Applied Physics* **98**, doi:10.1063/1.1994942 (2005).

80 Lu, W. & Kim, D. Engineering nanophase self-assembly with elastic field. *Acta Materialia* **53**, 3689-3694, doi:10.1016/j.actamat.2005.04.021 (2005).

81 Yu, H. C. & Lu, W. Dynamics of the self-assembly of nanovoids and nanobubbles in solids. *Acta Materialia* **53**, 1799-1807, doi:10.1016/j.actamat.2004.12.029 (2005).

82 Takaki, T., Hasebe, T. & Tomita, Y. Two-dimensional phase-field simulation of self-assembled quantum dot formation. *Journal of Crystal Growth* **287**, 495-499, doi:10.1016/j.jcrysgro.2005.11.072 (2006).

83 Tan, L. & Zabaras, N. A level set simulation of dendritic solidification of multi-component alloys. *Journal of Computational Physics* **221**, 9-40, doi:10.1016/j.jcp.2006.06.003 (2007).

84 Wu, X.-F. & Dzenis, Y. A. Phase-field modeling of the formation of lamellar nanostructures in diblock copolymer thin films under inplanar electric fields. *Physical Review E* **77**, doi:10.1103/PhysRevE.77.031807 (2008).

85 Granasy, L., Tegze, G., Toth, G. I. & Pusztai, T. Phase-field crystal modelling of crystal nucleation, heteroepitaxy and patterning. *Philosophical Magazine* **91**, 123-149, doi:10.1080/14786435.2010.487476 (2011).

86 Sadtler, B. *et al.* Phototropic growth control of nanoscale pattern formation in photoelectrodeposited Se-Te films. *Proceedings of the National Academy of Sciences of the United States of America* **110**, 19707-19712, doi:10.1073/pnas.1315539110 (2013).

87 Bhattacharya, A., Kiran, A., Karagadde, S. & Dutta, P. An enthalpy method for modeling eutectic solidification. *Journal of Computational Physics* **262**, 217-230, doi:10.1016/j.jcp.2014.01.007 (2014).

88 Fang, A. *et al.* Capillary effects in guided crystallization of organic thin films. *Apl Materials* **3**, doi:10.1063/1.4915537 (2015).

89 Almarza, N. G., Pekalski, J. & Ciach, A. Effects of confinement on pattern formation in two dimensional systems with competing interactions. *Soft Matter* **12**, 7551-7563, doi:10.1039/c6sm01400c (2016).

90 Lu, L.-X. *et al.* Nanostructure Formation by controlled dewetting on patterned substrates: A combined theoretical, modeling and experimental study. *Scientific Reports* **6**, doi:10.1038/srep32398 (2016).

91 Fang, A. & Haataja, M. Modeling and Analysis of Electrodeposition in Porous Templates. *Journal of the Electrochemical Society* **164**, D875-D887, doi:10.1149/2.1331713jes (2017).

92 Hill, J. D. & Millett, P. C. Numerical Simulations of Directed Self-Assembly in Diblock Copolymer Films using Zone Annealing and Pattern Templating. *Scientific Reports* **7**, doi:10.1038/s41598-017-05565-w (2017).

93 Hsu, H.-Y., Lin, B.-T. & Hsu, Y.-R. Three-dimensional numerical investigation of dendritic self-organizational structure growth on a nanopost surface. *Advances in Mechanical Engineering* **9**, doi:10.1177/1687814016683357 (2017).

94 Kurita, R. Control of pattern formation during phase separation initiated by a propagated trigger. *Scientific Reports* **7**, doi:10.1038/s41598-017-07352-z (2017).

95 Thornton, K., Agren, J. & Voorhees, P. W. Modelling the evolution of phase boundaries in solids at the meso- and nano-scales. *Acta Materialia* **51**, 5675-5710, doi:10.1016/j.actamat.2003.08.008 (2003).

96 Boussinot, G., Hueter, C. & Brener, E. A. Growth of a two-phase finger in eutectics systems. *Physical Review E* **83**, doi:10.1103/PhysRevE.83.020601 (2011).

97 Rowlinson, J. S. Translation of JD van der Waals, The Thermodynamic Theory of Capillarity Under the Hypothesis of a Continuous Variation of Density. *Journal of Statistical Physics* **20**, 197-244, doi:10.1007/bf01011513 (1979).

98 Kim, S. G., Kim, W. T. & Suzuki, T. Phase-field model for binary alloys. *Physical Review E* **60**, 7186-7197, doi:10.1103/PhysRevE.60.7186 (1999).

99 Karma, A. & Rappel, W. J. Phase-field method for computationally efficient modeling of solidification with arbitrary interface kinetics. *Physical Review E* **53**, R3017-R3020, doi:10.1103/PhysRevE.53.R3017 (1996).

100 Cahn, J. W. & Hilliard, J. E. Free energy of a nonuniform system. iii. Nucleation in a 2-component incompressible fluid. *Journal of Chemical Physics* **31**, 688-699, doi:10.1063/1.1730447 (1959).

101 Provatas, N., Elder, K. & Wiley Online, L. Phase-field methods in materials science and engineering.

102 Allen, S. M. & Cahn, J. W. Microscopic theory for antiphase boundary motion and its application to antiphase domain coarsening. *Acta Metallurgica* **27**, 1085-1095, doi:10.1016/0001-6160(79)90196-2 (1979).

103 Kobayashi, R. MODELING AND NUMERICAL SIMULATIONS OF DENDRITIC CRYSTAL-GROWTH. *Physica D* **63**, 410-423, doi:10.1016/0167-2789(93)90120-p (1993).

104 Caginalp, G. An analysis of a phase field model of a free-boundary. *Archive for Rational Mechanics and Analysis* **92**, 205-245 (1986).

105 Wheeler, A. A., Boettinger, W. J. & McFadden, G. B. Phase-field model for isothermal phase-transition in binary alloys. *Physical Review A* **45**, 7424-7439, doi:10.1103/PhysRevA.45.7424 (1992).

106 Guyer, J. E., Boettinger, W. J., Warren, J. A. & McFadden, G. B. Phase field modeling of electrochemistry. I. Equilibrium. *Physical Review E* **69**, doi:10.1103/PhysRevE.69.021603 (2004).

107 Guyer, J. E., Boettinger, W. J., Warren, J. A. & McFadden, G. B. Phase field modeling of electrochemistry. II. Kinetics. *Physical Review E* **69**, doi:10.1103/PhysRevE.69.021604 (2004).

108 Nestler, B. & Wheeler, A. A. A multi-phase-field model of eutectic and peritectic alloys: numerical simulation of growth structures. *Physica D* **138**, 114-133, doi:10.1016/s0167-2789(99)00184-0 (2000).

109 Apel, M., Boettger, B., Diepers, H. J. & Steinbach, I. 2D and 3D phase-field simulations of lamella and fibrous eutectic growth. *Journal of Crystal Growth* **237**, 154-158, doi:10.1016/s0022-0248(01)01895-4 (2002).

110 Folch, R. & Plapp, M. Towards a quantitative phase-field model of two-phase solidification. *Physical Review E* **68**, doi:10.1103/PhysRevE.68.010602 (2003).

111 Kim, S. G., Kim, W. T., Suzuki, T. & Ode, M. Phase-field modeling of eutectic solidification. *Journal of Crystal Growth* **261**, 135-158, doi:10.1016/j.jcrysgro.2003.08.078 (2004).

112 Folch, R. & Plapp, M. Quantitative phase-field modeling of two-phase growth. *Physical Review E* **72**, doi:10.1103/PhysRevE.72.011602 (2005).

113 Karma, A. Phase-field formulation for quantitative modeling of alloy solidification. *Physical Review Letters* **87**, doi:10.1103/PhysRevLett.87.115701 (2001).

114 Boussinot, G. & Brener, E. A. Achieving realistic interface kinetics in phase-field models with a diffusional contrast. *Physical Review E* **89**, doi:10.1103/PhysRevE.89.060402 (2014).

115 Ohno, M., Takaki, T. & Shibuta, Y. Variational formulation of a quantitative phase-field model for nonisothermal solidification in a multicomponent alloy. *Physical Review E* **96**, doi:10.1103/PhysRevE.96.033311 (2017).

116 Karma, A. Phase-field model of eutectic growth. *Physical Review E* **49**, 2245-2250, doi:10.1103/PhysRevE.49.2245 (1994).

117 Elder, K. R., Drolet, F., Kosterlitz, J. M. & Grant, M. Stochastic eutectic growth. *Physical Review Letters* **72**, 677-680, doi:10.1103/PhysRevLett.72.677 (1994).

118 Elder, K. R., Gunton, J. D. & Grant, M. Nonisothermal eutectic crystallization. *Physical Review E* **54**, 6476-6484, doi:10.1103/PhysRevE.54.6476 (1996).

119 Wheeler, A. A., McFadden, G. B. & Boettinger, W. J. Phase-field model for solidification of a eutectic alloy. *Proceedings of the Royal Society a-Mathematical Physical and Engineering Sciences* **452**, 495-525, doi:10.1098/rspa.1996.0026 (1996).

120 Plapp, M. & Karma, A. Eutectic colony formation: A phase-field study. *Physical Review E* **66**, doi:10.1103/PhysRevE.66.061608 (2002).

121 Akamatsu, S., Plapp, M., Faivre, G. & Karma, A. Overstability of lamellar eutectic growth below the minimum-undercooling spacing. *Metallurgical and Materials Transactions a-Physical Metallurgy and Materials Science* **35A**, 1815-1828, doi:10.1007/s11661-004-0090-z (2004).

122 Green, J. R., Jimack, P. K. & Mullis, A. M. Phase field analysis of eutectic breakdown. *Metallurgical and Materials Transactions a-Physical Metallurgy and Materials Science* **38A**, 1426-1432, doi:10.1007/s11661-007-9144-3 (2007).

123 Parisi, A. & Plapp, M. Stability of lamellar eutectic growth. *Acta Materialia* **56**, 1348-1357, doi:10.1016/j.actamat.2007.11.037 (2008).

124 Parisi, A. & Plapp, M. Defects and multistability in eutectic solidification patterns. *Epl* **90**, doi:10.1209/0295-5075/90/26010 (2010).

125 Plapp, M. & Karma, A. Eutectic colony formation: A stability analysis. *Physical Review E* **60**, 6865-6889, doi:10.1103/PhysRevE.60.6865 (1999).

126 Serefoglu, M., Napolitano, R. E. & Plapp, M. Phase-field investigation of rod eutectic morphologies under geometrical confinement. *Physical Review E* **84**, doi:10.1103/PhysRevE.84.011614 (2011).

127 Serefoglu, M., Bottin-Rousseau, S., Akamatsu, S., Faivre, G. & Iop. in *3rd International Conference on Advances in Solidification Processes* Vol. 27 *IOP Conference Series-Materials Science and Engineering* (2012).

128 Ghosh, S. & Plapp, M. Influence of interphase boundary anisotropy on bulk eutectic solidification microstructures. *Acta Materialia* **140**, 140-148, doi:10.1016/j.actamat.2017.08.023 (2017).

129 Lahiri, A., Tiwary, C., Chattopadhyay, K. & Choudhury, A. Eutectic colony formation in systems with interfacial energy anisotropy: A phase field study. *Computational Materials Science* **130**, 109-120, doi:10.1016/j.commatsci.2017.01.007 (2017).

130 Zhang, A., Guo, Z. & Xiong, S. M. Eutectic pattern transition under different temperature gradients: A phase field study coupled with the parallel adaptive-mesh-refinement algorithm. *Journal of Applied Physics* **121**, doi:10.1063/1.4978606 (2017).

131 Kazemi, O., Hasemann, G., Krueger, M., Halle, T. & Iop. in *18th Chemnitz Seminar on Materials Engineering* Vol. 118 *IOP Conference Series-Materials Science and Engineering* (2016).

132 Choudhury, A., Plapp, M. & Nestler, B. Theoretical and numerical study of lamellar eutectic three-phase growth in ternary alloys. *Physical Review E* **83**, doi:10.1103/PhysRevE.83.051608 (2011).

133 Hoetzer, J. *et al.* Large scale phase-field simulations of directional ternary eutectic solidification. *Acta Materialia* **93**, 194-204, doi:10.1016/j.actamat.2015.03.051 (2015).

134 Hoetzer, J. *et al.* Phase-field simulations of spiral growth during directional ternary eutectic solidification. *Acta Materialia* **106**, 249-259, doi:10.1016/j.actamat.2015.12.052 (2016).

135 Hunt, J. D. & Chilton, J. P. An investigation of lamella-rod transition in binary eutectics. *Journal of the Institute of Metals* **91**, 338-& (1963).

136 Plapp, M., Bottin-Rousseau, S., Faivre, G. & Akamatsu, S. Eutectic solidification patterns: Interest of microgravity environment. *Comptes Rendus Mecanique* **345**, 56-65, doi:10.1016/j.crme.2016.10.008 (2017).

137 Serefoglu, M. & Napolitano, R. E. On the selection of rod-type eutectic morphologies: Geometrical constraint and array orientation. *Acta Materialia* **56**, 3862-3873, doi:10.1016/j.actamat.2008.02.050 (2008).

138 Chen, S.-H., Chen, C.-C., Luo, Z. P. & Chao, C.-G. Fabrication and characterization of eutectic bismuth-tin (Bi-Sn) nanowires. *Materials Letters* **63**, 1165-1168, doi:10.1016/j.matlet.2009.02.019 (2009).

139 Chen, S. H., Chen, C. C. & Chao, C. G. Novel morphology and solidification behavior of eutectic bismuth-tin (Bi-Sn) nanowires. *Journal of Alloys and Compounds* **481**, 270-273, doi:10.1016/j.jallcom.2009.03.107 (2009).

140 Wu, Y. Y. *et al.* Composite mesostructures by nano-confinement. *Nature Materials* **3**, 816-822, doi:10.1038/nmat1230 (2004).

141 Hecht, U. *et al.* Multiphase solidification in multicomponent alloys. *Materials Science & Engineering R-Reports* **46**, 1-49, doi:10.1016/j.mser.2004.07.002 (2004).

142 Hunt, J. D. & Jackson, K. A. Dendrite-eutectic transition. *Transactions of the Metallurgical Society of Aime* **239**, 864-& (1967).

143 Khorasaninejad, M. & Capasso, F. Metalenses: Versatile multifunctional photonic components. *Science* **358**, doi:10.1126/science.aam8100 (2017).

144 Yan, Z. *et al.* Three-dimensional mesostructures as high-temperature growth templates, electronic cellular scaffolds, and self-propelled microrobots. *Proceedings of the National Academy of Sciences of the United States of America* **114**, E9455-E9464, doi:10.1073/pnas.1713805114 (2017).

145 Steinhart, M. *et al.* Polymer nanotubes by wetting of ordered porous templates. *Science* **296**, 1997-1997, doi:10.1126/science.1071210 (2002).

146 Shimada, M., Kokawa, H., Wang, Z. J., Sato, Y. S. & Karibe, I. Optimization of grain boundary character distribution for intergranular corrosion resistant 304 stainless steel by twin-induced grain boundary engineering. *Acta Materialia* **50**, 2331-2341, doi:10.1016/s1359-6454(02)00064-2 (2002).

147 Palumbo, G., Lehockey, E. M. & Lin, P. Applications for grain boundary engineered materials. *Jom-Journal of the Minerals Metals & Materials Society* **50**, 40-43, doi:10.1007/s11837-998-0248-z (1998).

148 Lee, D. S., Ryoo, H. S. & Hwang, S. K. A grain boundary engineering approach to promote special boundaries in Pb-base alloy. *Materials Science and Engineering a-Structural Materials Properties Microstructure and Processing* **354**, 106-111, doi:10.1016/s0921-5093(02)00919-x (2003).

149 Watanabe, T. & Tsurekawa, S. The control of brittleness and development of desirable mechanical properties in polycrystalline systems by grain boundary engineering. *Acta Materialia* **47**, 4171-4185, doi:10.1016/s1359-6454(99)00275-x (1999).

150 Holloway, K. & Fryer, P. M. Tantalum as a diffusion barrier between copper and silicon. *Applied Physics Letters* **57**, 1736-1738, doi:10.1063/1.104051 (1990).

151 Kim, H. *et al.* Robust TaNx diffusion barrier for Cu-interconnect technology with subnanometer thickness by metal-organic plasma-enhanced atomic layer deposition. *Journal of Applied Physics* **98**, doi:10.1063/1.1935761 (2005).

152 Kuczynski, G. C. The mechanism of densification during sintering of metallic particles. *Acta Metall.* **4**, 58-61 (1956).

153 Seigle, L. Role of grain boundaries in sintering. *Kinetics of High-Temperature Processes*, 172-178 (1959).

154 Tikkanen, M. The part of volume and grain boundary diffusion in the sintering of one-phase metallic systems. *Plansee. Pulvermet.* **11**, 70-81 (1963).

155 Guo, X. & Zhang, Z. L. Grain size dependent grain boundary defect structure: case of doped zirconia. *Acta Materialia* **51**, 2539-2547, doi:10.1016/s1359-6454(03)00052-1 (2003).

156 Pedersen, A. & Jonsson, H. Simulations of hydrogen diffusion at grain boundaries in aluminum. *Acta Materialia* **57**, 4036-4045, doi:10.1016/j.actamat.2009.04.057 (2009).

157 Hammond, K. D., Hu, L., Maroudas, D. & Wirth, B. D. Helium impurity transport on grain boundaries: Enhanced or inhibited? *EPL (Europhysics Letters)* **110**, 52002 (2015).

158 Vladimirov, I., Kühn, M., Geßner, T., May, F. & Weitz, R. T. Energy barriers at grain boundaries dominate charge carrier transport in an electron-conductive organic semiconductor. **8**, 14868 (2018).

159 Jain, R. K. & Stylianopoulos, T. Delivering nanomedicine to solid tumors. *Nature Reviews Clinical Oncology* **7**, 653-664, doi:10.1038/nrclinonc.2010.139 (2010).

160 Khalkhali, M., Rajabpour, A. & Khoeini, F. Thermal transport across grain boundaries in polycrystalline silicene: A multiscale modeling. **9**, 5684 (2019).

161 Wang, Y.-J., Gao, G.-J. J. & Ogata, S. Atomistic understanding of diffusion kinetics in nanocrystals from molecular dynamics simulations. *Physical Review B* **88**, 115413 (2013).

162 Uberuaga, B. P., Vernon, L. J., Martinez, E. & Voter, A. F. The relationship between grain boundary structure, defect mobility, and grain boundary sink efficiency. **5**, 9095 (2015).

163 Yu, H. C., Chen, H. Y. & Thornton, K. Extended smoothed boundary method for solving partial differential equations with general boundary conditions on complex boundaries.

Modelling and Simulation in Materials Science and Engineering **20**, 41, doi:10.1088/0965-0393/20/7/075008 (2012).

164 Echebarria, B., Folch, R., Karma, A. & Plapp, M. Quantitative phase-field model of alloy solidification. *Physical Review E* **70**, doi:10.1103/PhysRevE.70.061604 (2004).

165 Fischer, E. Thermodynamic optimization of the AgCl-KCl and BaCl2-LiCl systems. *Journal of Phase Equilibria* **24**, 228-235, doi:10.1361/105497103770330523 (2003).

166 Rodrigues, P. C. R. & Fernandes, F. Melting, freezing and nucleation in nanoclusters of potassium chloride. II Modelling the solid-liquid coexistence. *European Physical Journal D* **41**, 113-119, doi:10.1140/epjd/e2006-00178-y (2007).

167 Pelton, A. D. & Thompson, W. T. A structural model for magnesium-containing melts. *Canadian Journal of Chemistry* **48**, 1585-&, doi:10.1139/v70-258 (1970).

168 Osher, S. & Fedkiw, R. P. *Level set methods and dynamic implicit surfaces*. (Springer, 2003).

169 CRYSTRAN. *Potassium Chloride*, <http://www.crystran.co.uk/optical-materials/potassium-chloride-kcl> (accessed June 5 2016).

170 CRYSTRAN. *Silver Chloride*, <http://www.crystran.co.uk/optical-materials/silver-chloride-agcl> (accessed June 5 2016).

171 Nagasaka, Y., Nakazawa, N. & Nagashima, A. Experimental-determination of the thermal-diffusivity of molten alkali-halides by the forced Rayleigh-scattering method. i. Molten LiCl, NaCl, KCl, RbCl, and CsCl. *International Journal of Thermophysics* **13**, 555-574, doi:10.1007/bf00501941 (1992).

172 Whitelaw, J. H. *Convective Heat Transfer*, <http://thermopedia.com/content/660/> (accessed June 5 2016).

173 Thompson, W. T. & Flengas, S. N. Drop calorimetric measurements on some chlorides, sulfides, and binary melts. *Canadian Journal of Chemistry* **49**, 1550-&, doi:10.1139/v71-252 (1971).

174 Moelans, N., Blanpain, B. & Wollants, P. Quantitative analysis of grain boundary properties in a generalized phase field model for grain growth in anisotropic systems. *Physical Review B* **78**, doi:10.1103/PhysRevB.78.024113 (2008).

175 Groeber, M. A. & Jackson, M. A. DREAM.3D: A Digital Representation Environment for the Analysis of Microstructure in 3D. *Integrating Materials and Manufacturing Innovation* **3**, 5, doi:10.1186/2193-9772-3-5 (2014).

176 Tian, B. *et al.* Macroporous nanowire nanoelectronic scaffolds for synthetic tissues. *Nature Materials* **11**, 986-994, doi:10.1038/nmat3404 (2012).

177 Xie, C., Lin, Z., Hanson, L., Cui, Y. & Cui, B. Intracellular recording of action potentials by nanopillar electroporation. *Nature Nanotechnology* **7**, 185-190, doi:10.1038/nnano.2012.8 (2012).

178 Lind, J. U. *et al.* Instrumented cardiac microphysiological devices via multimaterial three-dimensional printing. *Nature Materials* **16**, 303-+, doi:10.1038/nmat4782 (2017).

179 Mannoor, M. S. *et al.* 3D Printed Bionic Ears. *Nano Letters* **13**, 2634-2639, doi:10.1021/nl4007744 (2013).

180 Wehner, M. *et al.* An integrated design and fabrication strategy for entirely soft, autonomous robots. *Nature* **536**, 451-+, doi:10.1038/nature19100 (2016).

181 Wang, J. & Gao, W. Nano/Microscale Motors: Biomedical Opportunities and Challenges. *Acs Nano* **6**, 5745-5751, doi:10.1021/nn3028997 (2012).

182 Solovev, A. A., Mei, Y., Urena, E. B., Huang, G. & Schmidt, O. G. Catalytic Microtubular Jet Engines Self-Propelled by Accumulated Gas Bubbles. *Small* **5**, 1688-1692, doi:10.1002/smll.200900021 (2009).

183 Valentine, J. *et al.* Three-dimensional optical metamaterial with a negative refractive index. *Nature* **455**, 376-U332, doi:10.1038/nature07247 (2008).

184 Overvelde, J. T. B. *et al.* A three-dimensional actuated origami-inspired transformable metamaterial with multiple degrees of freedom. *Nature Communications* **7**, doi:10.1038/ncomms10929 (2016).

185 Song, Z. *et al.* Origami lithium-ion batteries. *Nature Communications* **5**, doi:10.1038/ncomms4140 (2014).

186 Liu, W. *et al.* 3D Porous Sponge-Inspired Electrode for Stretchable Lithium-Ion Batteries. *Advanced Materials* **28**, 3578-+, doi:10.1002/adma.201505299 (2016).

187 Wu, W., Wen, X. & Wang, Z. L. Taxel-Addressable Matrix of Vertical-Nanowire Piezotronic Transistors for Active and Adaptive Tactile Imaging. *Science* **340**, 952-957, doi:10.1126/science.1234855 (2013).

188 Chen, Z. *et al.* Three-dimensional flexible and conductive interconnected graphene networks grown by chemical vapour deposition. *Nature Materials* **10**, 424-428, doi:10.1038/nmat3001 (2011).

189 Syms, R. R. A., Yeatman, E. M., Bright, V. M. & Whitesides, G. M. Surface tension-powered self-assembly of micro structures - The state-of-the-art. *Journal of Microelectromechanical Systems* **12**, 387-417, doi:10.1109/jmems.2003.811724 (2003).

190 Song, Y. M. *et al.* Digital cameras with designs inspired by the arthropod eye. *Nature* **497**, 95-99, doi:10.1038/nature12083 (2013).

191 Murphy, S. V. & Atala, A. 3D bioprinting of tissues and organs. *Nature Biotechnology* **32**, 773-785, doi:10.1038/nbt.2958 (2014).

192 Truby, R. L. & Lewis, J. A. Printing soft matter in three dimensions. *Nature* **540**, 371-378, doi:10.1038/nature21003 (2016).

193 Cumpston, B. H. *et al.* Two-photon polymerization initiators for three-dimensional optical data storage and microfabrication. *Nature* **398**, 51-54 (1999).

194 Meza, L. R., Das, S. & Greer, J. R. Strong, lightweight, and recoverable three-dimensional ceramic nanolattices. *Science* **345**, 1322-1326, doi:10.1126/science.1255908 (2014).

195 Sun, Y., Choi, W. M., Jiang, H., Huang, Y. Y. & Rogers, J. A. Controlled buckling of semiconductor nanoribbons for stretchable electronics. *Nature Nanotechnology* **1**, 201-207, doi:10.1038/nnano.2006.131 (2006).

196 Xu, F., Lu, W. & Zhu, Y. Controlled 3D Buckling of Silicon Nanowires for Stretchable Electronics. *Acs Nano* **5**, 672-678, doi:10.1021/nn103189z (2011).

197 Cavallo, F. & Lagally, M. G. Nano-origami: Art and function. *Nano Today* **10**, 538-541, doi:10.1016/j.nantod.2015.07.001 (2015).

198 Im, S. H., Lim, Y. T., Suh, D. J. & Park, O. O. Three-dimensional self-assembly of colloids at a water-air interface: A novel technique for the fabrication of photonic bandgap crystals. *Advanced Materials* **14**, 1367-1369, doi:10.1002/1521-4095(20021002)14:19<1367::aid-adma1367>3.0.co;2-u (2002).

199 Nych, A. *et al.* Assembly and control of 3D nematic dipolar colloidal crystals. *Nature Communications* **4**, doi:10.1038/ncomms2486 (2013).

200 Gao, P. X. *et al.* Conversion of zinc oxide nanobelts into superlattice-structured nanohelices. *Science* **309**, 1700-1704, doi:10.1126/science.1116495 (2005).

201 Noorduin, W. L., Grinthal, A., Mahadevan, L. & Aizenberg, J. Rationally Designed Complex, Hierarchical Microarchitectures. *Science* **340**, 832-837, doi:10.1126/science.1234621 (2013).

202 Luo, Z. *et al.* Atomic gold-enabled three-dimensional lithography for silicon mesostructures. *Science* **348**, 1451-1455, doi:10.1126/science.1257278 (2015).

203 Xu, S. *et al.* Assembly of micro/nanomaterials into complex, three-dimensional architectures by compressive buckling. *Science* **347**, 154-159, doi:10.1126/science.1260960 (2015).

204 Zhang, Y. *et al.* A mechanically driven form of Kirigami as a route to 3D mesostructures in micro/nanomembranes. *Proceedings of the National Academy of Sciences of the United States of America* **112**, 11757-11764, doi:10.1073/pnas.1515602112 (2015).

205 Yan, Z. *et al.* Mechanical assembly of complex, 3D mesostructures from releasable multilayers of advanced materials. *Science Advances* **2**, doi:10.1126/sciadv.1601014 (2016).

206 Zhang, Y. *et al.* Printing, folding and assembly methods for forming 3D mesostructures in advanced materials. *Nature Reviews Materials* **2**, doi:10.1038/natrevmats.2017.19 (2017).

207 Jang, K.-I. *et al.* Self-assembled three dimensional network designs for soft electronics. *Nature Communications* **8**, doi:10.1038/ncomms15894 (2017).

208 Rogers, J., Huang, Y., Schmidt, O. G. & Gracias, D. H. Origami MEMS and NEMS. *Mrs Bulletin* **41**, 123-129, doi:10.1557/mrs.2016.2 (2016).

209 Yan, Z. *et al.* Controlled Mechanical Buckling for Origami-Inspired Construction of 3D Microstructures in Advanced Materials. *Advanced Functional Materials* **26**, 2629-2639, doi:10.1002/adfm.201504901 (2016).

210 Ning, X. *et al.* 3D Tunable, Multiscale, and Multistable Vibrational Micro-Platforms Assembled by Compressive Buckling. *Advanced Functional Materials* **27**, doi:10.1002/adfm.201605914 (2017).

211 Choi, J. *et al.* Processing-Dependent Microstructure of AgCl-CsAgCl2 Eutectic Photonic Crystals. *Advanced Optical Materials* **6**, 8, doi:10.1002/adom.201701316 (2018).

212 Blanco, A. *et al.* Large-scale synthesis of a silicon photonic crystal with a complete three-dimensional bandgap near 1.5 micrometres. *Nature* **405**, 437-440 (2000).

213 Gratson, G. M. *et al.* Direct-write assembly of three-dimensional photonic crystals: Conversion of polymer scaffolds to silicon hollow-woodpile structures. *Advanced Materials* **18**, 461-+, doi:10.1002/adma.200501447 (2006).

214 Merino, R. I., Pena, J. I., Larrea, A., de la Fuente, G. F. & Orera, V. M. *Melt grown composite ceramics obtained by directional solidification: Structural and functional applications*. Vol. 4 (2003).

215 Parviz, B. A., Ryan, D. & Whitesides, G. M. Using self-assembly for the fabrication of nano-scale electronic and photonic devices. *Ieee Transactions on Advanced Packaging* **26**, 233-241, doi:10.1109/tadvp.2003.817971 (2003).

216 Vlasov, Y. A., Bo, X. Z., Sturm, J. C. & Norris, D. J. On-chip natural assembly of silicon photonic bandgap crystals. *Nature* **414**, 289-293, doi:10.1038/35104529 (2001).

217 Pawlak, D. A. *et al.* Second order self-organized pattern of terbium-scandium-aluminum garnet and terbium-scandium perovskite eutectic. *Journal of Applied Physics* **91**, 9731-9736, doi:10.1063/1.1479752 (2002).

218 Acosta, M. F., Rodrigo, S. G., Martin-Moreno, L., Pecharroman, C. & Merino, R. I. Micropillar Templates for Dielectric Filled Metal Arrays and Flexible Metamaterials. *Advanced Optical Materials* **5**, doi:10.1002/adom.201600670 (2017).

219 Fukutani, K., Tanji, K., Motoi, T. & Den, T. Ultrahigh pore density nanoporous films produced by the phase separation of eutectic Al-Si for template-assisted growth of nanowire arrays. *Advanced Materials* **16**, 1456-+, doi:10.1002/adma.200400268 (2004).

220 Sadecka, K. *et al.* When Eutectics Meet Plasmonics: Nanoplasmonic, Volumetric, Self-Organized, Silver-Based Eutectic. *Advanced Optical Materials* **3**, 381-389, doi:10.1002/adom.201400425 (2015).

221 Yasui, N., Ohashi, Y., Kobayashi, T. & Den, T. Development of Phase-Separated Scintillators with Light-Guiding Properties. *Advanced Materials* **24**, 5464-5469, doi:10.1002/adma.201201962 (2012).

222 Massaouti, M. *et al.* Eutectic epsilon-near-zero metamaterial terahertz waveguides. *Optics Letters* **38**, 1140-1142, doi:10.1364/ol.38.001140 (2013).

223 Kisza, A., Dzielendziak, J. & Kazmierczak, J. *Kinetics and mechanism of the silver electrode reaction in molten Agcl-CsCl binary mixtures*. Vol. 98 (1998).

224 Sternberg, S. & Terzi, M. Surface tension of molten binary mixtures - AgCl+RbCl and AgCl+CsCl. *Journal of Chemical Thermodynamics* **3**, 259-+, doi:10.1016/s0021-9614(71)80111-8 (1971).

225 Street, K. N., Stjohn, C. F. & Piatti, G. Structures of unidirectionally solidified binary eutectics Al-Al4Ca Al-Al4Ce and Al-Al3Y. *Journal of the Institute of Metals* **95**, 326-& (1967).

226 Livingston, J. D. Structure and magnetic properties of Au-Co aligned eutectic. *Journal of Applied Physics* **41**, 197-+, doi:10.1063/1.1658321 (1970).

227 Racek, R., Lesoult, G. & Turpin, M. Cd-Sn eutectic structures at low growth-rates. *Journal of Crystal Growth* **22**, 210-218, doi:10.1016/0022-0248(74)90096-7 (1974).

228 Kurz, W. & Lux, B. Growth of Ni-W eutectic. *Metallurgical Transactions* **2**, 329-&, doi:10.1007/bf02662684 (1971).

229 Ratkai, L., Toth, G. I., Kornyei, L., Pusztai, T. & Granasy, L. Phase-field modeling of eutectic structures on the nanoscale: the effect of anisotropy. *Journal of Materials Science* **52**, 5544-5558, doi:10.1007/s10853-017-0853-8 (2017).

230 Liu, S., Lee, J. H. & Trivedi, R. Dynamic effects in the lamellar-rod eutectic transition. *Acta Materialia* **59**, 3102-3115, doi:10.1016/j.actamat.2011.01.050 (2011).

231 Croker, M. N., Fidler, R. S. & Smith, R. W. Characterization of eutectic structures. *Proceedings of the Royal Society of London Series a-Mathematical Physical and Engineering Sciences* **335**, 15-&, doi:10.1098/rspa.1973.0111 (1973).

232 Hu, X. J., Jain, A. & Goodson, K. E. Investigation of the natural convection boundary condition in microfabricated structures. **47**, 820-824 (2008).

233 Sandonnini, C. & Scarpa, G. Analisi termiche di miscele binarie di cloruri di elementi monovalenti. Nota IV. *Reale Accademia Dei Lincei* **21**, 77 (1912).

234 Sternberg, S. & Herdlicka, C. Interdiffusion Coefficient of the Ag Ion in Molten Alkali Chlorides by the Chronopotentiometric Method. *Revue Roumaine de Chimie* **17**, 343 (1972).

235 Elliott, R. Eutectic solidification. *International Metals Reviews* **22**, 161-186 (1977).

236 Kulkarni, A. A., Kohanek, J., Hanson, E., Thornton, K. & Braun, P. V. Control of lamellar eutectic orientation via template-directed solidification. *Acta Materialia* **166**, 715-722, doi:10.1016/j.actamat.2019.01.016 (2019).

237 Akamatsu, S. & Plapp, M. Eutectic and peritectic solidification patterns. *Current Opinion in Solid State and Materials Science* **20**, 46-54 (2016).

238 Fischer, E. Thermodynamic Optimization Of The AgCl-KCl and BaCl 2-LiCl Systems. *Journal of Phase Equilibria* **24**, 228-235 (2003).

239 Braun, P. V., Osenar, P. & Stupp, S. I. Semiconducting superlattices templated by molecular assemblies. *Nature* **380**, 325-328, doi:10.1038/380325a0 (1996).

240 vanBlaaderen, A., Ruel, R. & Wiltzius, P. Template-directed colloidal crystallization. *Nature* **385**, 321-324, doi:10.1038/385321a0 (1997).

241 Tavakkoli, K. G. A. *et al.* Templating Three-Dimensional Self-Assembled Structures in Bilayer Block Copolymer Films. *Science* **336**, 1294-1298, doi:10.1126/science.1218437 (2012).

242 Tavakkoli, K. G. A. *et al.* Rectangular Symmetry Morphologies in a Topographically Templated Block Copolymer. *Advanced Materials* **24**, 4249-+, doi:10.1002/adma.201104895 (2012).

243 Grunbaum, B. & Shephard, G. C. C. F. p. d. N. Tilings by Regular Polygons. *Mathematics Magazine* **50**, 227-247 (1977).

244 David, S., Chelnokov, A. & Lourtioz, J. M. Isotropic photonic structures: Archimedean-like tilings and quasi-crystals. *Ieee Journal of Quantum Electronics* **37**, 1427-1434, doi:10.1109/3.958365 (2001).

245 Richter, J., Schulenburg, J. & Honecker, A. in *Quantum Magnetism* 85-153 (Springer, 2004).

246 Schaedler, T. A. *et al.* Ultralight metallic microlattices. *Science* **334**, 962-965 (2011).

247 Masuda, H. & Satoh, M. Fabrication of gold nanodot array using anodic porous alumina as an evaporation mask. *Japanese Journal of Applied Physics Part 2-Letters* **35**, L126-L129, doi:10.1143/jjap.35.l126 (1996).

Appendix A: Nucleation Threshold in Eutectic Solidification Simulations

As discussed in Chapter 4 Section 4.2.2, a nucleation control mechanism was implemented into the eutectic solidification phase-field model to study eutectic solidification confined to three-dimensional cage structures. When a chemical threshold, μ_t, was exceeded at the eutectic solidification front, a nucleus of the phase corresponding with that concentration buildup was added to facilitate nucleation of that phase. This appendix will explain how that chemical threshold was chosen for the simulations presented in Chapter 4 Section 4.2.

First, a range of chemical threshold values were utilized in simulations to study the effects of threshold selection. These simulations used the phase-field model described in Chapter 3 Section 3.1 with Equations 3.5 and 3.8 governing the evolution. Figure A.1 shows the resultant microstructures from the simulations using a high, moderate, and low chemical potential threshold, μ_t. The simulation corresponding to the high μ_t, in fact, did not have nucleation control implemented at all; thus, μ_t can be considered infinite in that case. When lamellae terminate at the edge of the ribbon, the lamellar spacing necessarily increases. Since the solidification velocity remains unchanged, this larger spacing is not stable. Therefore, new

lamellae must nucleate in proximity to the ribbon edge to maintain the desired local spacing. With a high nucleation barrier ($\mu_t = \infty$), new lamellae are not able to form and instead, the remaining lamellae oscillate to mitigate the instability of a larger lamellar spacing (Figure A.1a). Conversely, if the nucleation threshold is quite low ($\mu_t = 1.1\times10^{-3}$), lamellae nucleate too freely, even far from the ribbon edge where the lamellar spacing is stable (Figure A.1c). However, with a moderate nucleation threshold ($\mu_t = 4.0\times10^{-3}$), lamellae nucleate only in proximity to the ribbon edge without erroneous oscilation (Figure A.1b). As the moderate nucleation threshold structure most closely matched experimental observations (see Figure 4.5), $\mu_t = 4.0\times10^{-3}$ was selected to conduct the study.

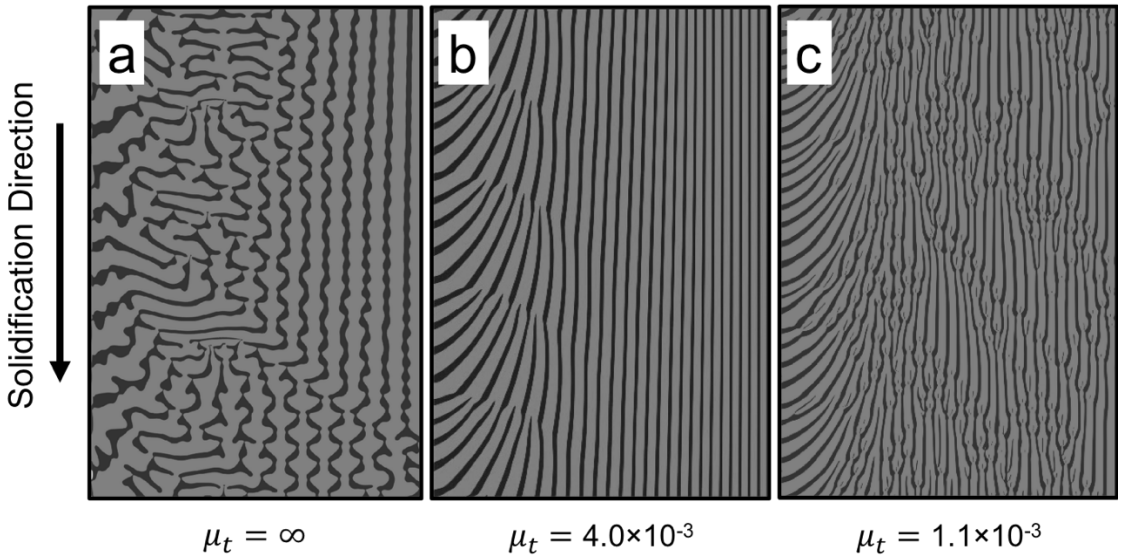

Figure A.1 Phase-field simulation results for a range of chemical potential nucleation thresholds: Eutectic solidification confined to the edge of a ribbon leg from a three-dimensional cage structure was simulated with **(a)** no nucleation control (i.e., $\mu_t = \infty$), **(b)** a moderate chemical potential threshold ($\mu_t = 4.0\times10^{-3}$), and **(c)** a low chemical potential threshold ($\mu_t = 1.1\times10^{-3}$). The solidification direction is down and the left edge of each image corresponds to the edge of the ribbon.